



DISSERTATION APPROVAL SHEET

Title of Dissertation: Analysis and Protocols to Establish Downlink for Communication
Across the Air-Water Interface

Name of Candidate: Md Shafiqul Islam
mdislam1@umbc.edu
Doctor of Philosophy, 2022

Graduate Program: Computer Engineering

Dissertation and Abstract Approved:

A handwritten signature in black ink, appearing to read "Mohamed Younis".

Mohamed Younis
younis@umbc.edu

Professor
Computer Science and Electrical Engineering
11/29/2022 | 12:26:39 PM EST

NOTE: *The Approval Sheet with the original signature must accompany the thesis or dissertation. No terminal punctuation is to be used.

Curriculum Vitae

Name: Md Shafiqul Islam

EDUCATION

Ph.D. in Computer Engineering Dec 2022
University of Maryland Baltimore County, USA

M.Sc. in Computer Engineering May 2019
University of Maryland Baltimore County, USA

M.Sc. in Applied Physics, Electronics & Communication Engineering July 2014
University of Dhaka, Bangladesh

B.Sc. in Applied Physics, Electronics & Communication Engineering Feb 2013
University of Dhaka, Bangladesh

Major: Computer Engineering.

PUBLICATIONS

M. S. Islam, M. Younis and A. Ahmed, "Communication Through Air Water Interface using Multiple Light Sources," *2018 IEEE International Conference of Communications (ICC)*, Kansas City, MO, USA, 2018.

M. S. Islam, and M. Younis, "Analyzing Visible Light Communication Through Air-Water Interface," *IEEE Access*, vol. 7, pp. 123830-123845, 2019.

M. S. Islam, and M. Younis, "An Adaptive DPPM for Efficient and Robust Visible Light Communication across the Air-Water Interface" *Proc. of for 29th Wireless and Optical Communications Conference (WOCC)*, Newark, NJ, May 2020.

M. S. Islam, M. Younis, M. Mahmud, and J. B. Saif, "A Novel Encoding Scheme for Improving the Bandwidth Efficiency of DPPM," *IEEE International Conference on Communications*, pp. 1-6, Montreal, QC, Canada, 2021.

M. S. Islam, M. Younis, and F. S. Choa, "Optimizing Acoustic Signal Quality for Linear Photoacoustic Communication," *IEEE International Conference on Communications*, pp. 1-6, Montreal, QC, Canada, 2021.

M. Mahmud, **M. S. Islam**, M. Younis, and G. Carter, "Optical Focusing-based Adaptive Modulation for Photoacoustic Communication," *2021 30th Wireless and Optical Communications Conference (WOCC)*, 2021, pp. 272-276.

M. Mahmud, **M. S. Islam**, A. Ahmed, M. Younis, and F. S. Choa, “Cross-Medium Photoacoustic Communications: Challenges, and State of the Art,” *Sensors*, vol. 22, pp. 4224, 2022.

M. S. Islam, M. Younis, M. Mahmud, G. carter, and F. S. Choa, “A Peak Detection Based OOK Photoacoustic Modulation Scheme for Air to Underwater Communication,” *Optics Communications*, under review

PROSPECTIVE POSITION

Associate Hardware Engineer,
Schweitzer Engineering Laboratories
2350 NE Hopkins Court
Pullman, WA 99163 - USA

ABSTRACT

Title of Document: ANALYSIS AND PROTOCOLS TO ESTABLISH DOWNLINK FOR COMMUNICATION ACROSS THE AIR-WATER INTERFACE

Md Shafiqul Islam, Ph.D., 2022

Directed By: Prof. Mohamed Younis

Abstract:

In underwater wireless networks (UWNs), conventionally there is no direct communication between an underwater node and a remote command center, because there is no known physical signal that propagates well in both the water and air mediums. Radio signals are the popular choice in the air while acoustics are the prime means for communication underwater. Hence, the typical architecture of an UWN includes surface nodes or gateways which have dual modems, an acoustic modem to communicate with underwater nodes and a radio modem to interact with terrestrial command centers. However, such an architecture is logistically complicated and could expose the network to security threat. Therefore, it is desirable to establish a direct communication from air to underwater without having any intermediate surface node. This dissertation opts to fulfill such a need by pursuing two viable solutions, namely, using visual light communications (VLC) and exploiting the optoacoustic (photoacoustic) effect. Through extensive analysis and experiments we show that VLC is an effective means for scenarios where the distance between the airborne and underwater nodes is relatively short. We first analyze the coverage area and intensity inside the water for a light transmitter placed in the air. We then provide guidelines for

using single and multiple light sources to establish robust VLC links under rough environmental conditions like high water current and turbidity. Furthermore, we investigate effective modulation techniques that suit VLC. For long distance communication, VLC is not a viable option since light gets absorbed at an exponentially growing rate with the increase of water depth. Photoacoustic (PA) energy transfer mechanism is the promising method for long distance communication. Although the use of the photoacoustic mechanism is quite common in medical imaging, little progress has been made on building the communication protocol stack for air-to-underwater communication. In our research work, at first, we have studied the channel characteristics of the PA based air-to-underwater communication. We show that by carefully choosing the relative position of the airborne unit and underwater node, we can generate a narrowband acoustic signal which is very crucial for long distance communication. Moreover, we develop suitable modulation and demodulation schemes for PA communication.

ANALYSIS AND PROTOCOLS TO ESTABLISH DOWNLINK FOR
COMMUNICATION ACROSS THE AIR-WATER INTERFACE

By

Md Shafiqul Islam

Dissertation submitted to the Faculty of the Graduate School of the
University of Maryland, Baltimore County, in partial fulfillment
of the requirements for the degree of

DOCTOR OF PHILOSOPHY

2022

© Copyright by
Md Shafiqul Islam
2022

Preface

As a young child, like every other, I was very studious but had no idea about what the outcome of all of this study is. My vision of education had completely changed when I got the opportunity to study at Notre Dame College which is the best college in my home country, Bangladesh. As an urban teenager, it was a great opportunity; however, such an opportunity came along with lots of responsibilities because I had to compete with the nation's top ranked students. Finally, I succeeded and learned that the true meaning of knowledge is not only learning from the book but also how to apply that knowledge to contribute to science and engineering. Hence, I decided to pursue research career. Finding a research topic in this modern era that will contribute to mankind is another difficult task. Luckily with the help of my mentor and advisor Dr. Mohamed Younis, I have come up with an interesting topic to do research. I observed that 70% of the earth's surface is covered by water but yet we know very little about the underwater world because of a lack of communication from the earth to the underwater. In this dissertation, I have tried to build a model using visible light and photoacoustic energy conversion method to establish communication from the air to the underwater. I hope my research work will make a little contribution in this field.

Acknowledgements

To begin with, I would like to thank almighty God who has guided me to the right path to fulfil this thesis requirement. At the starting of my Ph. D., it was challenging for me to remain calm and persistent to focus on the study because it's a long journey in spite of the fact that I know it's fulfilling at the end. But I was fortunate enough to get tremendous support from a few superb individuals around me and I would like to express my gratitude to them.

First, I would like to express my appreciation to my advisor Dr. Mohamed Younis who's predominant exhorting and fantastic mentoring lead to the fruitful completion of this dissertation. His broad knowledge of the research field and open mind attitude on a discussion help me a lot to shape my ideas and implementing those ideas. He is a guardian and mentor at the same time to me.

I would moreover like to thank my committee member Dr. Fow-Sen Choa, Dr. Gary Carter, Dr. Lloyd Emokpae, and Dr. Akram Fadhl N. Ahmed for their support and guidance throughout my Ph. D. period.

I would like to thank my whole family for the support they have shown as I might not have accomplished such victory without their support. I want to give special thanks to my mother for her tremendous support since my childhood. She used to be my mentor and tutor in my childhood. Moreover, I want to give special thanks to my wife who is also pursuing her graduate degree along with me. Her mental support boosts my courage to finish my dissertation. I am blessed to have my daughter, Riddhi Hrishita Islam during my Ph. D. Having a child inspire me a lot to finish my Ph. D. I am

fortunate to have some wonderful friends in every stage of life. They help a lot to peruse my desire target.

Finally, I would like to acknowledge the National Science Foundation Grant #0000010465 for providing the funds necessary to perform the research.

Table of Contents

PREFACE.....	II
ACKNOWLEDGEMENTS.....	III
TABLE OF CONTENTS.....	V
LIST OF FIGURES	VII
CHAPTER 1: INTRODUCTION	1
1.1 Motivation.....	1
1.2 Visible Light Communication (VLC).....	1
1.3 Photoacoustic Communication	4
1.4 Organization.....	7
CHAPTER 2: RELATED WORK.....	8
2.1 Underwater Communication.....	8
2.2 Modulation Techniques for VLC.....	9
2.3 Photoacoustic Communication	10
CHAPTER 3: SYSTEM MODEL.....	12
3.1 VLC Background.....	12
3.1.1 Best Suited Optical Signal	12
3.1.2 Modeling the Water Surface	13
3.1.3 Modulation techniques for VLC communication he Water Surface	15
3.2 Photoacoustic Background.....	17
3.2.1 Photoacoustic Mechanism	17
3.2.2 Design Challenges	19
CHAPTER 4: VLC COMMUNICATION USING A SINGLE LIGHT SOURCE.....	21
4.1 Single Source Analysis	22
4.2 Coverage Area	23
4.3 Light Intensity.....	27
CHAPTER 5: MULTIPLE BEAMFORMED LIGHT SOURCES.....	31
5.1 Positioning of Multiple Light Sources.....	32
5.2 Analysis of Three Beamformed Light Sources.....	34
CHAPTER 6: VALIDATION RESULTS OF VLC COMMUNICATION	36
6.1 Simulation for a Flat Water Surface	36
6.2 Wavy Surfaces	39
6.3 Lab Experiment.....	40
CHAPTER 7: MODULATION: ADAPTIVE DPPM	43
7.1 Frame design.....	43
7.2 Protocol Efficiency	45
7.3 Algorithms and Illustrative Examples	48
7.4 Validation Results.....	51

CHAPTER 8: MODULATION: IMPROVING BANDWIDTH EFFICIENCY OF DPPM	54
8.1 Theoretical Analysis	54
8.2 Improving Bandwidth Efficiency	56
8.3 Frame Design	59
8.4 Validation Results	63
CHAPTER 9: PHOTOACOUSTIC: OPTIMIZING ACOUSTIC SIGNAL QUALITY	65
9.1 Acoustic Spectral Response	66
9.2 Parameter Effect Analysis	69
9.3 Positioning of Airborne and Underwater Nodes	71
9.3.1 Flat Water Surface	72
9.3.2 Wavy Water Surface	72
9.4 Validation Results	74
CHAPTER 10: PHOTOACOUSTIC: MODULATION SCHEME	76
10.1 Transmitter and Receiver Design	76
10.1.1 Transmitter Design	77
10.1.2 Receiver Design	78
10.2 Validation Results	80
10.2.1 Lab Experiments	80
10.2.2 Simulation Results	84
CHAPTER 11: CONCLUSION AND FUTURE WORK	88
11.1 Conclusion	88
11.2 Future Work	89
CHAPTER 12: REFERENCES	94
APPENDICES	91

List of Figures

Figure 1: 3D view of a coverage area inside the water.....	2
Figure 2: Block diagram of photoacoustic communication from air to water.....	5
Figure 3: Illustrating the shape of a cnoidal wave	13
Figure 4: Different modulation techniques for VLC communication	15
Figure 5: Air to underwater communication using photoacoustic mechanism	18
Figure 6: (a) Generated acoustic signal from a single laser pulse and (b) FFT of that acoustic signal.....	19
Figure 7: Generated acoustic signal from a Q-switch Nd:Yag laser with repetition rate = 10 Hz.....	20
Figure 8: Illustration of light ray direction in a wavy surface	21
Figure 9: Illustrating the difference between the actual and effective coverage area for (a) shallow water ($H=1$ m, $T=5.6$ sec, $\lambda=30$ m and $h=3$ m), (b) deep water ($H=0.2$ m; $T=1.2$ sec; $h=10$ m), and (c) flat water surface.....	24
Figure 10: Effect of step size of rotation angle on accuracy of r_{eff} and runtime of the algorithm. Note that relative runtime means in comparison to the case where $\Delta r = 1$	27
Figure 11: Relationship between transmittance and reflectance and the incident angle	28
Figure 12: Effect of scattering factor, n on the light propagation.....	29
Figure 13: Relation between coverage area and intensity for (a) single light source and (b) three light sources.....	30
Figure 14: Changes of I_{min} for different beam angles of a single light source. The plot is based on setting $d_a = 10$ m, $d_w = 10$ m and $p = 100$ w/m ²	31
Figure 15: Communication through the air-water interface using multiple light sources.....	32
Figure 16: Sample arrangement for: (a) two, (b) three in straight line, (c) three in triangular, (d) four, (e) five, and (f) six light sources. Same power ‘P’ is equally split among all sources.....	33
Figure 17: The coverage and light intensity at various underwater depth for a single light source placed in air at a height, $d_a = 5$ m, from the water surface with beam angle, $\theta=10^\circ, 20^\circ$, and 50°	36
Figure 18: The effect of underwater distance on the coverage and light intensity for three collinear beamformed light sources places at height $d_a = 5$ m above the water surface.....	37
Figure 19: Comparison of intensity and coverage area for a single light source with different beam angles in (a), and (b), and for three beamformed sources in (c), where $d_a = 5$ m and $d_w = 5$ m.	38
Figure 20: Effect of water surface wave’s amplitude on intensity for single light source	39
Figure 21: Effect of instantaneous time on intensity for single light source	39
Figure 22: Coverage area in presence of water waves for both (a) single and (b) multiple light sources.....	40

Figure 23: Changes in coverage area for different wave amplitude for (a) Single light source, (b) three beamformed sources.	40
Figure 24: Comparing intensity and coverage area for both single (a), (b) and multiple light sources (c) at $d_a = 5\text{m}$ and $d_w = 5\text{m}$ for wavy water surface.....	41
Figure 25: Experimental and theoretical results for light intensity at $d_a = 0.25\text{m}$ and $d_w = 0.46\text{m}$, with $\theta = 52^\circ$	41
Figure 26: ADPPM frame structure.....	43
Figure 27: Effect of data size, D and M on protocol efficiency, η	47
Figure 28: An example ADPPM frame	49
Figure 29: An example of decoding received ADPPM frame.....	49
Figure 30: Bit rate vs SNR for different value of M	51
Figure 31: Packet error rate vs SNR for different M in DPPM	52
Figure 32: PER vs underwater depth for various modulation techniques	52
Figure 33: DPPM frame sizes for different methods ($D = 32$ bits)	57
Figure 34: EDPPM (a) and CDPPM (b) frame structures	59
Figure 35: Illustration of creating EDPPM frame	61
Figure 36: Illustration of creating CDPPM frame	62
Figure 37: Protocol efficiency of EDPPM frame for different data size.....	63
Figure 38: Power efficiency of EDPPM frame relative to OOK frame for different data size.....	63
Figure 39: Protocol efficiency of CDPPM frame for different data size.....	64
Figure 40: Power efficiency of CDPPM frame relative to OOK frame for different data size.....	64
Figure 41: General geometry for linear optoacoustic communication from air to underwater.....	68
Figure 42: Determination of directionality factor, D for a) $\theta_r = 0^\circ$, b) $\theta_r = 45^\circ$ and amplitude, A_0 c) $\theta_r = 45^\circ$ and $\theta = 45^\circ$ for various frequency component of pressure wave	69
Figure 43: Directionality, D vs vertical observation angle, θ for (a) $\theta_r = 00$ and (b) $\theta_r = 600$	71
Figure 44: Relative position of laser beam incident point and hydrophone position for better quality pressure wave.....	72
Figure 45: Relative position of laser beam incident point and hydrophone for (a) flat and (b) wavy water surface.....	73
Figure 46: Sum of θ and θ_r for all phases of a water surface wave. Here water surface is assumed to be a sine wave	73
Figure 47: Spectral response of acoustic wave, for (a) $\theta_r = 00, \theta = 00$, (b) $\theta_r = 850, \theta = 850$, (c) $\theta_r = 850, \theta = 00$, and (d) $\theta_r = 00, \theta = 850$	74
Figure 48: Spectral response of acoustic signal for various phase of the wavy water surface while wave amplitude = 30 cm	75
Figure 49: Timing diagram of PDOOK signals.....	77
Figure 50: Block diagram of the photoacoustic air-to-underwater communication..	78
Figure 51: Schematic diagram of the acoustic receiver circuit.....	79
Figure 52: Tx and Rx data for laser pulse energy 30 mj and repetition rate 10 Hz..	81
Figure 53: Depicting the experimental setup for air-to-underwater PA communication.....	81

Figure 54: Effect of laser pulse energy on the received acoustic signal strength for laser repetition rate (a) 10 Hz and (b) 20 Hz	82
Figure 55: Effect of laser repetition rate on received acoustic signal strength for laser pulse energy (a) 20 mj and (b) 50 mj	83
Figure 56:BER vs laser pulse energy for laser repetition rate 20 Hz for different noise levels	85
Figure 57: BER vs laser pulse repetition rate laser pulse energy for pulse energy 50 mj for different noise levels	85
Figure 58: SNR vs underwater depth for different laser pulse energy	87
Figure 59: SNR vs underwater depth for different laser pulse repetition rate	87

Chapter 1: Introduction

1.1 *Motivation*

Underwater Wireless Networks (UWNs) are deemed promising technology with numerous applications such as marine biology, oil field monitoring, water pollution studies, security surveillance, naval combat, etc. In fact, about 70% of the earth is covered by water. Due to the high absorption and attenuation coefficient of radio waves in underwater environments, acoustics has been the prime choice for communication in the water medium [1]. However, an acoustic signal mostly attenuates when crossing the water surface and a UWN cannot be directly accessed from a ground station using acoustic links. Therefore, a typical UWN uses floating nodes, e.g., boats or buoys, which act as gateways. A gateway carries dual modems, an acoustic modem to communicate with underwater nodes and a radio modem to interact with command centers. Nonetheless, such an approach requires preplanning and is costly; in fact, it may be impractical in risky application scenarios, e.g., during combat, and too slow when dealing with emerging events. For example, when monitoring an evolving event such as oil leakage or conducting search-and-rescue missions, sending a boat, or anchoring a buoy is logistically complicated and lacks responsiveness. Moreover, in military applications, a surface node can be easily detected and the presence of UWN may get uncovered. Therefore, an alternative means for reaching the UWN is needed. This dissertation opts to fulfill such a need by pursuing two viable solutions, namely, using Visual Light Communications (VLC) and exploiting the Optoacoustic or Photoacoustic (PA) effects.

1.2 *Visible Light Communication*

Visible light can travel up to 100 meters in water depending on the quality of the water [2]. High bandwidth and low time latency make visible light more suitable for communication through the air-water interface.

However, the shape of the water surface and water properties introduce some challenges. Depending on the wind, the water surface might be flat or wavy, which will dynamically vary the intensity and the area covered by a light beam inside the water. The high-water current could also cause an underwater node to drift away from the coverage area. Another important factor is the attenuation coefficient of water, which increases in proportion to the water impurity level. Therefore, the communication system should be adaptive to handle various water properties.

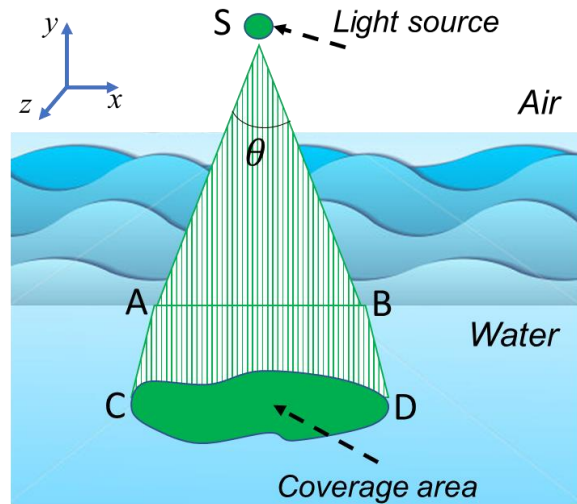


Figure 1: 3D view of a coverage area inside the water

Figure 1 illustrates a VLC system through the air-water interface. In this figure, a visible light source has been placed in the air at d_a meter above the water surface and an underwater node is placed at d_w depth underwater. The water surface could be flat or wavy. Based on some existing water surface models in the literature, in this research work, we first analytically study the effect of water surface and the various VLC parameters on the underwater coverage and optical beam intensity and provide guidelines for establishing robust VLC air-to-water links when using single and multiple light sources [3][4]. We also develop algorithms to calculate the intensity and coverage area for different water parameters like water wave's height, phases, water attenuation coefficient, and purity level etc.

Furthermore, we investigate effective modulation techniques that suit this kind of cross-medium communication. Generally, the scarcity of the optical power is the main challenge for underwater VLC, especially for wavy water surface and in case of impure water. Therefore, a power efficient modulation technique is crucial in order to support reliable communication and maximize the underwater reach from the airborne unit. There are various modulation techniques for optical communication. Among them On-Off

Keying (OOK) is the most simple and popular one. Though OOK is bandwidth efficient, it is not power efficient. The Pulse Position Modulation (PPM) is one of the most popular power efficient techniques for optical communication [5][6].

In PPM, each M bits are sent over a symbol $L= 2^M$ time chips and only one pulse is sent in L for the chip position, corresponding to the value of the M bits. However, PPM requires very accurate clock synchronization between the transmitter and receiver, which is quite challenging in underwater environments. Also, PPM is not bandwidth efficient. For bandwidth efficiency, a modified version of PPM is used which is Differential Pulse Position Modulation (DPPM). DPPM starts the next symbol after sending the pulse, i.e., before the elapse of the remaining time chips of the symbol L . Thus, in DPPM the transmitter and receiver do not need to have tightly synchronized clocks. Nonetheless, the bit error detection in DPPM is very complex as the number of chips in a frame are variable after modulation, i.e., the frame size is not constant.

In our research work, we introduce a new variant of DPPM to suit communication across the air-water interface. We show that the symbol size L affects both reliability and bandwidth efficiency. We argue that by varying the value of M in DPPM, we can control the Packet Error Rate (PER) and implicitly bit rate of DPPM, and trade it off with the bandwidth of a VLC link [7]. To enable the use of different values of M , we design and analyze a novel frame structure for DPPM which contains the information of M so that a receiver can detect the errors in the frame. As information about M is embedded within the transmitted frame, a transmitter can change the value of M any time without hindering correct reception. Using our proposed frame, we further develop an algorithm to transmit data from an airborne node to an underwater node while changing the value of M depending on the packet error rate. We name this as Adaptive Differential Pulse Position Modulation (ADPPM).

We further develop a novel encoding algorithm and frame structure in order to shorten the time between consecutive symbols and consequently improve the bit rate of L-DPPM [8]. The idea is based on avoiding bit

patterns that contribute the most to bandwidth inefficiency. The proposed algorithm explores several bit patterns remapping through simple complement and shifting operations. A detailed frame structure with all necessary control bits is provided. Overall, boosting the bandwidth efficiency comes at the expense of adding control bits and slightly increasing transmission power. The contributions of our research work on VLC cross-medium communication are summarized as follows:

- 1) Developing an algorithm for determining the effective coverage area and intensity inside the water medium. The algorithm can handle the various water conditions like wavy water surface, water attenuation coefficient etc.
- 2) Devising a scheme for beamforming using multiple light sources to control the underwater coverage area in the desired direction, which is suitable for hostile water conditions like drift current.
- 3) Proposing a novel ADPPM frame structure and design algorithms to create and decode such a frame structure. We also develop an algorithm to dynamically change the value of M of DPPM based on certain PER criteria.
- 4) Design a novel encoding algorithm and frame structure to increase the bandwidth efficiency of DPPM.

1.3 Photoacoustic Communication

Depending on the purity of the water, light can travel maximum 200 meters inside the water. So, VLC is good for communication up to few meters. For long distance, it is not practical since light attenuates exponentially with the increase of underwater depth. Therefore, we exploit the photoacoustic effect as an alternate way for long distance cross-medium communication. Alexander Graham Bell first discovered the photoacoustic effect in 1881 [9]. He noticed that when high intensity light impinges on a liquid medium like water, acoustic signal is generated which is called photoacoustic effect.

Photoacoustic energy conversion process could be divided into two mechanisms, linear and nonlinear. In linear PA, the variation in the light energy density creates a temperature fluctuation in the water medium. This temperature fluctuation then creates a volume fluctuation of the liquid medium. Eventually this volume fluctuation (contraction and expansion) creates an acoustic signal which propagates through the water medium.

In such linear PA mechanism, the generated sound energy is proportional to the applied light energy, i.e., laser beam energy. In this process the properties of the water medium do not change. In contrast, in nonlinear photoacoustic mechanism, the generated acoustic signal strength is not proportional to

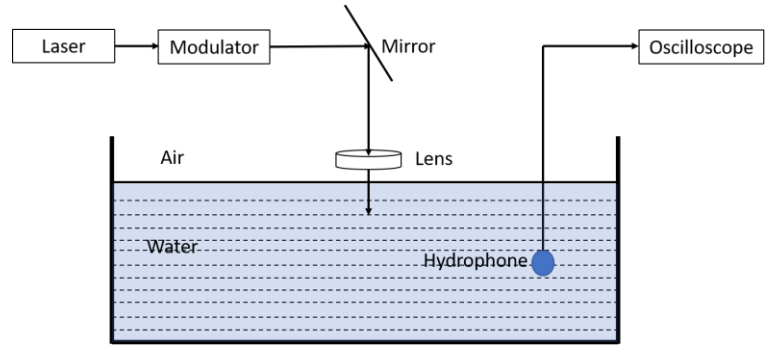


Figure 2: Block diagram of photoacoustic communication from air to water

the applied light energy. In this process, the physical properties of the water medium changes, i.e., water medium becomes vapor which creates cavitation bubbles. A detailed description of linear and non-linear PA have been given in section 3.2.1.

Figure 2 shows the general block diagram of a photoacoustic communication system from air to the water medium. A modulated high-power pulsed laser light is focused into the water using a lens and a mirror. A highly sensitive hydrophone is used to receive the generated sound wave from the laser light. This kind of communication setup is relatively unexplored and little development has been made on the protocol level. Our research work focuses on characterizing the channel propagation model and find a suitable modulation technique for this kind of communication.

Controlling the generated acoustic signal through the photoacoustic process is very complex. Specifically, if the repetition rate of laser pulses is low, the corresponding acoustic signal is very broadband. Since the higher frequency components of this broadband signal attenuate more in underwater environment, all the energy used to generate these signals is lost especially if the underwater node is very far from the location where PA effect is taking place. Hence, generating a relatively narrowband signal using the PA effect with lower frequency components is more desirable for long distance communication. Moreover, the frequency component of the broadband acoustic signal depends on the incident angle of the laser light and observation angle of the receiver,

i.e., the position of the underwater hydrophone. Both angles also change continuously for a wavy water surface, which makes it more complex to determine the frequency components of this kind of signal. In our research work, we show that by carefully choosing the relative position of the airborne unit and underwater node, we can generate a narrowband acoustic signal with lower frequency components for both flat and wavy water surfaces. We provide theoretical analysis and simulation results to capture the effect of these angles on the generated acoustic signals. We further provide guidelines for optimum angle setting for improving the quality of the photoacoustic communication link.

Another key issue with photoacoustic cross-medium communication is the lack of communication protocol stack, particularly devising modulation/demodulation schemes. The design of a suitable modulation/demodulation scheme for PA is quite challenging for several reasons. First, the generated acoustic signal in the nonlinear PA process is very broadband in nature which makes it difficult to pursue Frequency-shift keying (FSK) and Phase-shift keying (PSK). Second, the acoustic signal strength at the receiver is variable due to the intensity variation of any practical laser source, which makes the use of certain kinds of modulation techniques such as Quadrature amplitude modulation (QAM) very difficult. Third, the PA process is hybrid in nature, meaning that the transmitter is sending one kind of energy which is light, while the receiver is receiving another kind of energy, specifically acoustic. Because of such hybrid nature, the modulation and demodulation scheme are not reciprocal.

In our research, we address the aforementioned issues and devise a novel modulation and demodulation technique using the OOK methodology that is based on peak detection of the received acoustic signal. The key advantages of Peak Detection based OOK modulation (PDOOK) are that it is not sensitive to the broadband nature of the received signal and facilitates synchronizing the transmitter and receiver. These advantages simplify the transmitter and receiver design and yield low bit error rate. The contributions of our research work on photoacoustic cross-medium communication are summarized as follows:

- 1) Providing guidelines for the placement of the airborne unit and the underwater node for narrowband acoustic signal generation.
- 2) Analyzing the generated acoustic signal quality based on the laser light parameters and relative position of the transmitter and receiver.
- 3) Proposing and implementing a novel modulation and demodulation scheme that provides the best results for hybrid communication systems such as PA based on the above analysis.
- 4) Validating the performance of such a modulation and demodulation scheme in terms of the achievable bit rate and the bit error rate (BER), for different light parameters and varying receiver positions relative to the normal of the water surface at the laser light incident point, both by experiments and simulations.

1.4 Organization

This dissertation proposal is organized as follows. In chapter 2, related work is discussed. Chapter 3 provides a system model. VLC communication is elaborately described in chapter 4, 5 and 6. Chapter 7 and 8 describes modulation techniques for VLC communication. Meanwhile, Chapter 9 and 10 focus on photoacoustic based cross-medium communication. Chapter 11 presents conclusion and future work.

Chapter 2: Related Work

In this chapter, we review published work related to the dissertation contribution. We start with the literature review of underwater communication in general, and then focus on the modulation techniques that are used for VLC communication. Finally, we cover prior work on photoacoustic communication.

2.1 *Underwater Communication*

Acoustic waves are the prime choice for wireless communication in an underwater environment [10][11]. However, acoustic waves suffer high attenuation in the air medium. On the other hand, the electromagnetic wave (EM) is broadly used to communicate in the air, yet it is not suitable for a water medium due to its high attenuation coefficient [12][13]. Thus, neither EM nor acoustic waves can be used alone as a means for communication through the air-water interface. Another option could be Magnetic Induction (MI) as the magnetic permeability of air and water is almost the same, which helps MI to smoothly transition across the air-water interface [14]. Nonetheless, the conductive nature of the seawater affects the path loss of MI and consequently makes the communication range very small. As shown in [15], the communication range of MI is limited to 4.5 meters. Visible light, on the other hand, performs moderately in both air and water medium in terms of communication range. To our best knowledge, no prior research work has studied the visible light as a means for communication medium through the air-water interface. It is only used in either underwater [16][17][18] or air (indoor environment) [19][20].

In the literature, very few studies have targeted communication across the air-water interface. In [21], Translational Acoustic-RF communication (TARF) has been proposed. TARF supports only uplinks where data from underwater nodes are sent. The idea is that acoustic transmissions act as pressure waves that cause slight displacement upon striking the water surface. An airborne radar would measure these surface displacements and reform the acoustic wave. Not only TARF involves a very complex process, but also little

details are provided for how the displacement in the water surface can be differentiated from the natural surface vibration and on how data could be modulated and encoded.

In order to communicate through the air-water interface, the wavy water surface will increase scattering. Only a few publications have considered the effect of a wavy water surface. Peng et al. [22] have designed an adaptive filter to suppress the interference caused by the water waves to detect opto-acoustic conversion more precisely. In [23] the authors characterize the behavior of the optical link under various conditions like in air-water interface, still water, and turbid water. To mitigate turbulence-induced fading, spatial diversity has been pursued in [24]. However, no published research work has comprehensively studied the effect of water surface properties like wave amplitude and wave frequency. Our research work fills such a gap and studies the intensity and coverage area in underwater for VLC systems.

2.2 Modulation Techniques for VLC

Numerous modulation techniques have been developed for optical communication over the years. For simplicity, underwater optical communication usually uses Intensity-based Modulation with Direct Detection technique (IM / DD). The most common modulation technique is OOK with NRZ or RZ encoding [25][26][27]. Although the bandwidth efficiency and bit rate are very high using OOK-NRZ or OOK-RZ, power efficiency is not good. Since the optical signal needs to penetrate the air-water interface and continue propagating in underwater environments, power efficiency is very crucial for optical communication due to the absorption and scattering loss of the optical signal. The Pulse position modulation (PPM) is one of the most popular power efficient techniques for optical communication [5][6]. In PPM, each M bits are sent over a symbol $L = 2^M$ time chips and only one pulse is sent in L for the chip position, corresponding to the value of the M bits.

PPM requires very accurate clock synchronization between the transmitter and receiver, which is quite challenging in underwater environments. Moreover, PPM is not bandwidth efficient. In order to achieve better bandwidth efficiency, a number of modified versions of PPM have been proposed, such as Overlapping PPM (OPPM) [28][29], Multiple PPM (MPPM), Differential PPM (DPPM) [30][31], Pulse-interval modulation

(DPIM) [32][33], and Dual-header pulse-interval modulation (DH-PIM α) [34]. Among these PPM variants, DPPM is the most popular [30]. DPPM starts the next symbol after sending the pulse, i.e., before the elapse of the remaining time chips of the symbol L . Thus, in DPPM the transmitter and receiver do not need to have tightly synchronized clocks.

Only few studies could be found in the literature for improving the performance of DPPM. In [35], it has been shown that energy efficiency of DPPM can be increased as high as 42.5 % in comparison to OOK by choosing optimal data word length. Soft decision decoding is not possible for DPPM because of its variable symbol size. A modified version of DPPM, called IDPPM, is derived from DPPM by adding an extra zero before DPPM symbol [36]. This modification helps receiver for soft decision decoding. Although DPPM has a higher bandwidth efficiency than PPM, its bandwidth efficiency is still significantly lower than OOK. We found very few published studies on boosting the bandwidth efficiency of DPPM. In [37], DPPM is combined with Pulse-width modulation (PWM) to improve bandwidth efficiency. However, the realization of such a scheme requires reducing the pulse duration which increases the packet error rate significantly. In this research work we have shown that we can improve power efficiency by varying modulation index, M of DPPM. In addition to that we have also shown a way to increase the bandwidth efficiency and assess the corresponding inverse effect on power efficiency.

2.3 Photoacoustic Communication

Exploiting PA for air to underwater communication is a very promising method, especially over long distances. PA technology is quite popular in medical imaging [38][39][40] and industrial applications [41]. However, its uses for air to underwater communication is relatively new. There are some notable research studies. In [42], low-cost passive relays are deployed on the water surface to minimize the energy required for PA communication. However, the placement of these passive relays is logistically very complicated and requires preplanning, in fact, it could be risky in some application scenarios, e.g., during combat. A fully wireless link

between air and water is highly desirable for such a scenario. Moreover, the use of relays is applicable for linear optoacoustic links which are generally limited in range.

F. Blackmon and L. Antonelli have done extensive research on laser generated sound in the water medium by photoacoustic energy conversion method. In [43], F. Blackmon conducts theoretical and experimental study of time and frequency domain analysis of the generated acoustic signal in the water medium. He also shows the angular dependency of the sound pressure level for the oblique laser beam incidence at the air–water interface. In [44], they have investigated the M-array FSK and Multi-frequency Shift Keying (MFSK) for both linear and non-linear photoacoustic energy conversion.

There is some other notable research on photoacoustic downlink communication from air-to water. Y. H. Berthelot [45] has shown that the generated acoustic signal from the pulsed laser is basically a broadband signal. In order to create a narrowband signal, we need to choose the laser repetition rate carefully based on the laser parameters. Since the generated acoustic signal is broadband, there is a frequency that carries most of the energy, which is referred to as the peak frequency. The relationship between peak frequency and laser power has been discussed in [46]. From this paper we have come to know that with the increase of laser pulse energy, peak frequency decreases. Lower frequency acoustic signals can travel more in the underwater environment. Hence, for long distance underwater communication, we need to provide higher energy laser pulses.

Chapter 3: System Model

We will provide some theoretical background associated with the VLC and photoacoustic communication. We will start our discussion with VLC and then photoacoustic.

3.1 *VLC Background*

In order to communicate through the air-water interface using optics we first discuss what type of optical signal is most suited for this task and provide a detailed analysis of water surface. In this section, we highlight the different types of optical signals and how we can model the water surface based on shallow and deep water. At the end of this section, we will provide a details analysis of different modulation technique that can be used for this kind of communication set up.

3.1.1 *Best Suited Optical Signal*

In Chapter 1, we have discussed why the optical signal is the best one to communicate through the air-water medium. There are two types of optical signals which are mainly used in wireless optical communication, namely laser and visible light. Due to the high directivity of the laser light, it can penetrate the water surface much more than visible light [47][48]. However, such high directionality also complicates the establishment of communication links since it is hard to precisely target an inherently moving underwater receiver, e.g., due to water current. On the other hand, visible light with limited beam angle could provide reasonable penetration and coverage at the same time. Directional high-power Light-emitting diode (LED) has been improved a lot in recent years and made visible light communication a viable option. Moreover, secondary optics like lenses, reflectors, TIR (total internal reflection) optics, etc., can help in collimating the light rays to increase the light intensity. For example, the WAYLLSHINE® Zoomable Yard Flashlight [49] has a built-in lens that changes the beam angle of light, which ultimately controls the area of the spotlight. Moreover, among the visible light

sources, blue and green light attenuates least in the water environment [50][51]. So, in our experiment, we have used blue LED light sources.

3.1.2 Modeling the Water Surface

The water surface is not typically flat, where there is often a wave in air-water interface due to the wind. It is very difficult to find an

exact equation for the surface wave. In general, the surface wave mainly depends on water depth and wind speed. Figure 3 shows a simple water surface function and associated

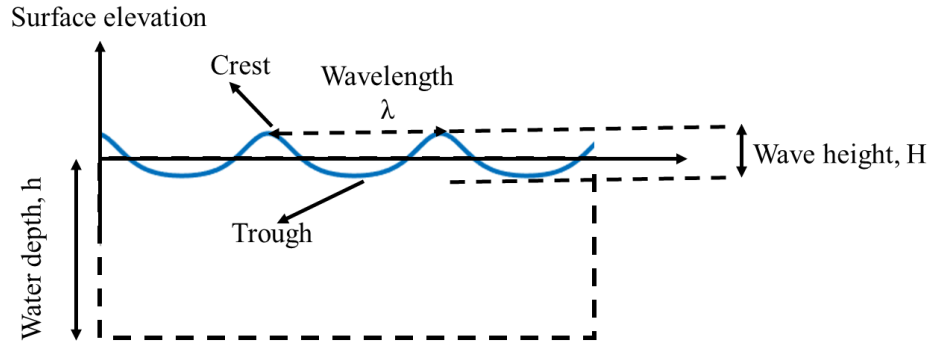


Figure 3: Illustrating the shape of a cnoidal water wave

parameter. Here the surface elevation is a cnoidal function. As seen in the figure, a cnoidal wave has a higher crest and a flatter trough than a sine wave. If h is the water depth and λ is the wavelength of the water surface wave, then the water source is defined as shallow water when $\lambda > h$. For shallow water, Boussinesq equations and Korteweg–de Vries equation (KdV) is the popular mathematical model for the water surface [52]. The solution of KdV is a cnoidal wave whose shape looks like the one that has been shown in Figure 3. The cnoidal-wave solution of the KdV equation can be presented as follows [53]:

$$\eta(x, t) = \eta_2 + H \cdot cn^2\left(\frac{x - ct}{\Delta} \middle| m\right) \quad (1)$$

Where η = surface elevation, x = horizontal coordinate, t = time, H = wave height, η_2 = trough elevation, c = phase speed and cn = one of the Jacobi elliptic functions. η_2 , Δ , λ , and c can be expressed as follows:

$$\eta_2 = \frac{H}{m} \left(1 - m - \frac{E(m)}{K(m)}\right) \quad , \quad \Delta = \frac{\lambda}{2K(m)} = h \sqrt{\frac{4m \cdot h}{3H}} \quad (2)$$

$$c = \sqrt{g \cdot h} \left[1 + \frac{H}{m \cdot h} \left(1 - \frac{1}{2}m - \frac{3E(m)}{2K(m)}\right)\right] \quad \text{and} \quad \tau = \frac{\lambda}{c} \quad (3)$$

On the other hand, general waves governed by Stokes' wave theory apply for intermediate and deep water [54]. Deep water is characterized with water depth that is much larger than wavelength ($h > \lambda$). According to Stokes' third-order theory, the water surface elevation can be expressed as follows [55]:

$$\eta(x, t) = \alpha \left\{ \left[1 - \frac{1}{16} (k \cdot \alpha)^2 \right] \cos \theta + \frac{1}{2} (k \cdot \alpha) \cos 2\theta + \frac{3}{8} (k \cdot \alpha)^2 \cos 3\theta \right\} + \mathcal{O}((k \cdot \alpha)^4) \quad (4)$$

$$c = \frac{w}{k} = \left(1 + \frac{1}{2} (k \cdot \alpha)^2 \right) \sqrt{\frac{g}{k} + \mathcal{O}((k \cdot \alpha)^4)} \quad (5)$$

$$\theta(x, t) = kx - wt \quad (6)$$

where $k \cdot \alpha$ is the wave steepness. If the value of $k \cdot \alpha$ is larger in Figure 3, the crest will be steeper, and the trough will be flatter. The solution of Eq. (4) is also a cnoidal type. In the analysis below, we will denote a water surface wave with $\eta(x, t)$, and depending on the water depth we use either Eq. (1) or Eq. (4), where for flat surface we will put simply $\eta = 0$. In the next section, we will show how these water surface models are used to enable communication across the air-water interface either using single or beamformed multiple light sources.

3.1.3 Modulation techniques for VLC communication across Water Surface

In PPM, information is encoded in the pulse position; the pulse position depends on the value represented by the corresponding M input data.

In L-PPM, a block of $M = \log_2 L$ input data is mapped into one of the L distinct waveforms containing only

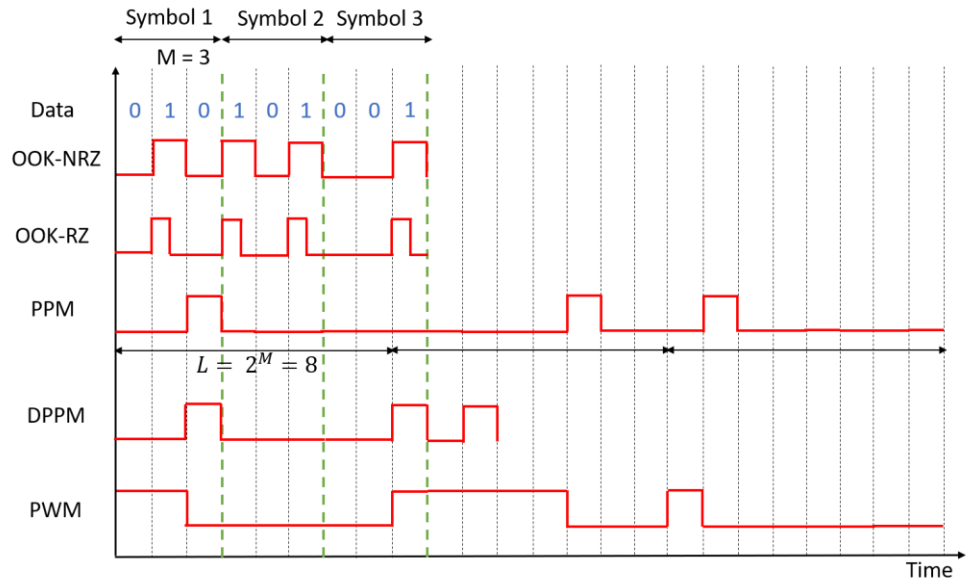


Figure 4: Different modulation techniques for VLC communication

one ‘on’ chip and the remaining $L-1$ chips are off, where $M > 0$. A pulse $p(t)$ is transmitted on that ‘on’ chip (time slot). Figure 4 explains the PPM with an example along with other modulation technique. In this example, actual data is 9 bits long. Here, we have chosen $M=3$ which means $L = 2^M = 8$; consequently, the main input data needs to be partitions into groups of 3 bits. In this example, the decimal value of first three input bits is 2, so the pulse position is also 2 in the first L time slots. In a similar way we can schedule those other pulses based on the decimal value of each group of 3 bits in the data payload.

PPM is a power efficient modulation technique because we are sending less ‘on’ pulses than other modulation techniques like OOK-NRZ, OOK-RZ, PWM. This is a key advantage for the energy constrained applications like those involving underwater wireless optical communication. However, the bandwidth efficiency of PPM is not as good as OOK because the symbol is longer, and more time is needed to transmit the same data than OOK. Another disadvantage of PPM is the need for very tight clock synchronization between the transmitter and receiver since accurate pulse positioning is crucial for successful reception in PPM.

These two issues are addressed in DPPM, which is a modified version of PPM. DPPM improves power efficiency as well as bandwidth efficiency by removing the extra zeros after the pulse position. Figure 4 also shows the DPPM waveform, where the extra zeros after the pulse have been omitted from the PPM waveform. Thus, the average number of slots per symbol in DPPM is:

$$\bar{L}_{DPPM} = \frac{L+1}{2} \quad (7)$$

which is half of that of PPM. Such optimization enables DPPM to outperform PPM in terms of bandwidth efficiency, and eliminate the need for tight clock synchronization. By knowing the time difference between two ‘on’ pulses, a receiver can extract the data.

Although DPPM’s omission of zeros after a pulse improves the bandwidth efficiency, it makes the modulated data size variable. In Figure 4, we can see all modulated waveforms have the same size for a fixed length of data except DPPM, which has variable number of time slots in the waveform depending on the input data. This variable time slot count in the output waveforms makes it quite difficult to decode if there are any errors in the received waveform. Any insertion/deletion of a “1” chip in the modulated waveform causes wrong decoding. Therefore, the number of ones in the modulated waveform is very important to decode the received signal correctly.

Another key parameter of DPPM is M . For a fixed data size, a larger M would increase energy efficiency by sending fewer ‘on’ pulses, yet at the same time it would decrease the bandwidth efficiency because we need more time slots to send the same data. Depending on the communication properties we can change the setting of M to get better results. For example, if in Figure 1 the underwater depth, d_w , is very small, i.e., the light intensity at the receiver is high enough to establish a communication link, we can keep M as low as possible so that bandwidth efficiency remains high. On the other hand, a large d_w would dramatically diminish the detectability of the light signal at the receiver; in this case we can use a bigger value of M so that fewer ‘on’ pulses are sent with high power.

Thus, changing M dynamically is very important for the VLC links across the air-water interface. However, if the transmitter module changes the value of M dynamically, it will not be possible for the receiver to demodulate the DPPM data. In this dissertation, we design a novel frame structure which contains the information of M so that the receiver module can decode the received signals. This frame structure also helps in detecting error within a frame. We call this adaptive DPPM (ADPPM) frame since it contains the information of M and changing the value of M will not hinder correct reception.

3.2 Photoacoustic Background

This section covers some background about the PA mechanism and highlights the challenges for designing suitable modulation and demodulation schemes.

3.2.1 Photoacoustic Mechanism

Alexander Graham Bell first discovered the photoacoustic effect in 1881. He noticed that when high-intensity light impinges on a liquid like water, an acoustic signal is generated, a phenomenon that is referred to as the photoacoustic effect. Figure 5 describes possible cross-medium communication by exploiting photoacoustic energy conversion. The photoacoustic energy conversion process could be divided into two mechanisms, linear and nonlinear. In a linear mechanism, high-intensity pulsed laser light is absorbed by the water and causes water to heat up. Since the laser light is pulsed, a water temperature fluctuation occurs where laser light gets absorbed by the water. This temperature fluctuation introduces a change in density which eventually creates a region of compression and rarefaction. Such compression and rarefaction of the water generate a propagating pressure wave. This process is also known as thermo-acoustic. In this process, the properties of the water medium do not change. The term “linear” is associated because the intensity of the generated sound wave is proportional to the applied intensity of the laser light. The conversion rate in this process is very low

which makes it inefficient for long distance communication [44][56]. In contrast to linear PA, in a nonlinear PA the generated acoustic signal strength is not proportional to the applied light energy, and the physical properties of the water medium change. When the intensity of the applied pulsed laser light energy exceeds a threshold level, the water becomes vapor and optical breakdown occurs. In this process water goes to a plasma state

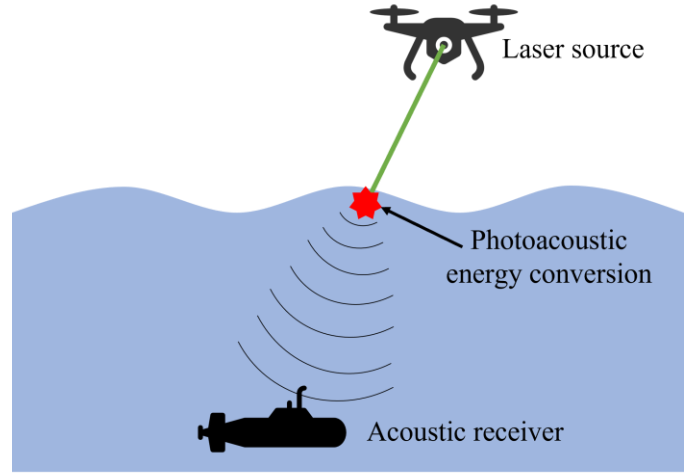


Figure 5: Air to underwater communication using photoacoustic mechanism

which creates optical breakdown induced acoustic shock waves. A nonlinear photoacoustic effect also creates additional cavitation bubble oscillation, which creates shockwaves as well. The energy conversion rate in a nonlinear optoacoustic process is much higher than the linear counterpart. It is reported on [56] that for a typical single pulse laser source the generated sound pressure level (SPL) is below 150 dB re μPa (decibel relative to a micro-Pascal) at a meter distance for linear photoacoustic whereas the SPL is higher than 178 dB re μPa for nonlinear photoacoustic. The breakdown threshold depends on the duration of the laser pulse. A. Vogel et al. [38] have studied the required breakdown irradiance threshold for nanosecond and femtosecond lasers. It has been concluded that irradiance energy levels in the order of 10^{11} W/cm^2 and 10^{13} W/cm^2 , are required for a nanosecond and a femtosecond laser, respectively. In order to create such high irradiance in the water we need to focus the laser light on the water. Hence, we have used focusing lenses on our lab experiments. The duration (τ), energy (E), diameter (D) of the laser beam and focal length (f) of the lens affect the value of laser irradiance in the water [57]. We can calculate the laser irradiance (I) as follows,

$$I = \frac{E}{\tau A_f} \quad (8)$$

where, A_f is the focal spot area which further can be calculated as follows,

$$A_f = \pi r^2 = \pi \left(\frac{\lambda f M^2}{\pi \frac{D}{2}} \right)^2 \quad (9)$$

where, λ is the wavelength of the laser light and M^2 is the beam quality factor of the laser beam. For a perfect Gaussian beam, the value of M^2 is 1. Hence, for a perfect Gaussian laser beam substituting the value of A_f from Eq. (9) into Eq. (8) we get,

$$I = \frac{\pi E}{4\tau} \left(\frac{D}{\lambda f} \right)^2 \quad (10)$$

We will use this equation to calculate the laser irradiance value in our lab experiments.

3.2.2 Design Challenges

There are four key issues that we must consider when designing a suitable modulation and demodulation scheme for PA-based communications. First, the

generated acoustic signal using the PA effect is very broadband in nature. Figure 6 shows both the time (Figure 6a) and frequency (Figure 6b) domain plots of the generated acoustic signal for a single laser pulse using a nonlinear PA

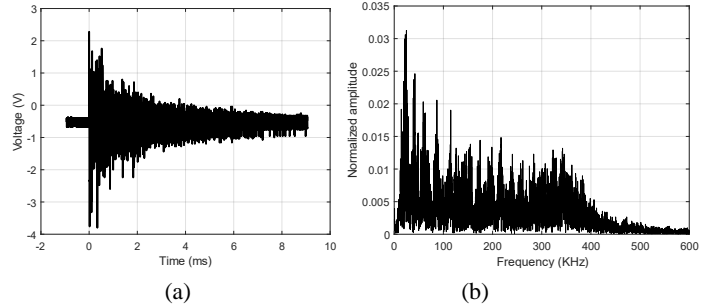


Figure 6: (a) Generated acoustic signal from a single laser pulse and (b) FFT of that acoustic signal

mechanism. From Figure 6b we can observe the

generated acoustic signal has spectral response up to 500 KHz. Although by applying a pass band filter we can detect a narrowband signal, the signal will become very weak. Hence, pursuing a FSK type modulation is quite challenging for this kind of PA signal.

Second, in nonlinear PA the optical breakdown of the water creates a vapor cloud around the plasma position [56]. This vapor cloud blocks the subsequent acoustic signal generation. To avoid such a scenario, we must wait a reasonable amount of time before sending the next laser pulse which constrains the repetition rate of laser pulses and eventually limits the channel capacity. In [56], it has been experimentally shown that even at

a laser pulse repetition rate of 200 Hz, there are several missing acoustic signals. Thirdly, even for fixed laser parameters the intensity of the generated acoustic signal could be inconsistent. This may be caused by imperfection in the laser source where the generated laser pulses do not have the same power. We have observed such power variability in our experiments, while using a custom-made laser by NASA Goddard Space Flight Center. Figure 7 shows an experimental result of the generated acoustic signal where the repetition rate of the laser pulse is 10 Hz. From this figure we can see, the peak value of each generated acoustic signal is not the same. This kind of amplitude fluctuation and others, for example environmental conditions such as water waves, making any kind of PAM, and QAM, modulation schemes quite challenging.

The fourth issue is related to the hybrid nature of the carriers, where the PA effect involves two different types of signals. In a PA-based communication, light energy is emitted from the transmitter and acoustic energy is sensed at the receiver. Such hybrid nature complicates the design of a suitable modulation and demodulation scheme. Considering all the above design challenges, we believe that OOK is the simplest, yet effective modulation and demodulation scheme for the PA mechanism.

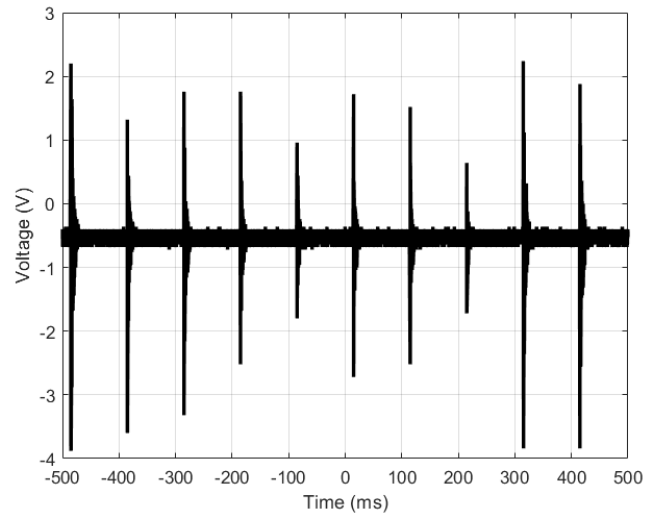


Figure 7: Generated acoustic signal from a Q-switch Nd:Yag laser with repetition rate = 10 Hz

Chapter 4: VLC Communication Using a Single Light Source

In this chapter, we analyze how we can use a single light source to communicate through the air-water interface. For this purpose, we will place a light source at a specific height from the water surface and focus the light into the water. Then we will analyze the intensity of light at a specific underwater depth. We use a light source with an adjustable beam angle so that we can control the intensity and coverage area inside the water. Table 1 provides a summary of the parameters used in the analysis. Here, we assume that the water medium is homogeneous. In our work, we refer to the spotlight inside the water as the coverage area.

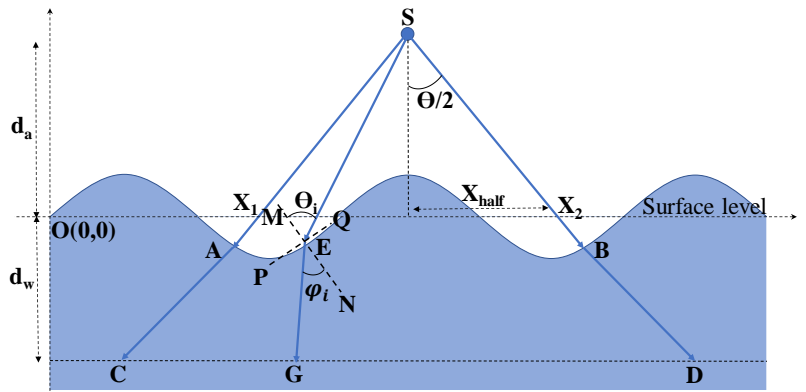


Figure 8: Illustration of light ray direction in a wavy surface

Figure 1 shows the 3D view of a single light transmitter S and the corresponding underwater coverage area. As seen in the figure, a light beam gets refracted as it penetrates the water surface. For a flat water surface the coverage area inside the water will be circular but if the water surface is wavy the coverage area will be irregularly shaped as shown in Figure 1. Basically, the conical propagation of the light will not be evenly refracted since the water surface is wavy. To determine the boundary of the coverage area, we first consider a cross section of the cone, e.g., the 2D plane of the two light beams SA and SB on the cone

Table 1. A summary of the important notations

<i>Notation</i>	Description
θ	Beam angle of light source
d_a	Proximity of the light source to the surface
d_w	Depth at which the underwater node exists
θ_i	Incident angle of light on the water surface
ϕ_i	Refraction angle of the light beam
ϕ	Angle of the refracted light beam edge
d	Diameter of the coverage area
η_l	Reflectance of light
τ_l	Transmittance of light
P	Power of single light source

surface, and then determine the corresponding underwater point C and D on the boundary of the underwater coverage area. When rotating such a 2D plane, two more points on the coverage area boundary can be determined. By incrementally rotating the 2D plane up to 360° we can fully define the underwater coverage area, as we explain below.

4.1 Single Source Analysis

Figure 8 shows a detailed view of the 2D plan used in the first step. The x -axis in Figure 8 is the water level in absence of any waves; the water surface disperses from this level to become wavy. The point $O(0,0)$ is considered the origin. A light source is placed at point $S(x_s, y_s)$ which is at a distance d_a meter above the water surface. θ is the beam angle of the light source. Ray SE is the incident ray from light source S , which strikes at point $E(x_e, y_e)$ on the water surface at incident angle θ_i with line MN . Here MN is the normal line of PQ , where PQ is the tangent at point E . The light ray gets refracted at point $G(x_g, y_g)$ from point E making the transmission angle φ_i . The coverage area will be determined by the refracted version of the boundary rays of the transmitted light beam. Moreover, to calculate the light intensity at an underwater point G , we need to determine the distance \overline{SE} and \overline{EG} , and angles θ_i and φ_i . The following shows how these measures are determined.

Assume that the water surface function is:

$$y = f(x) \quad (11)$$

For wavy water surface we can get the surface function using either Eq. (1) or Eq. (4) and for flat surface this is simply a straight line. The tangent at any point on the water surface is the first derivative of surface function on that point. Thus, the slope at point E is:

$$m_{PQ} = f'(x_e) \quad (12)$$

In order to calculate incident angle θ_i , we need to know the slope of SE and MN , which can be calculated as:

$$m_{SE} = \frac{y_s - y_e}{x_s - x_e} = \frac{y_s - f(x_e)}{x_s - x_e} \quad (13)$$

$$m_{MN} = \frac{-1}{m_{PQ}} = \frac{-1}{f'(x_e)} \quad (14)$$

Now, the angle between SE and MN is:

$$\tan \theta_i = \left| \frac{\frac{y_s - f(x_e)}{x_s - x_e} + \frac{1}{f'(x_e)}}{1 - \frac{y_s - f(x_e)}{(x_s - x_e)f'(x_e)}} \right|, \rightarrow \theta_i = \tan^{-1} \left| \frac{f'(x_e)(y_s - f(x_e)) + (x_s - x_e)}{(x_s - x_e)f'(x_e) - y_s + f(x_e)} \right| \quad (15)$$

If we know the incident angle, θ_i we can calculate transmission angle φ_i using Snell's law:

$$n_a \cdot \sin \theta_i = n_w \cdot \sin \varphi_i \quad (16)$$

Hence, the slope of line EG is:

$$m_{EG} = \frac{y_g - f(x_e)}{x_g - x_e} \quad \rightarrow \quad x_g = x_e + \frac{y_g - f(x_e)}{m_{EG}} \quad (17)$$

Now the relation between φ_i , m_{EG} and m_{MN} is:

$$\tan \varphi_i = \left| \frac{m_{MN} - m_{EG}}{1 + m_{MN} \cdot m_{EG}} \right| \quad (18)$$

If we expand Eq. (18) for m_{EG} then we get:

$$(m_{MN}^2 \cdot \tan^2 \varphi_i - 1) \cdot m_{EG}^2 + 2 \cdot m_{MN} (1 + \tan^2 \varphi_i) \cdot m_{EG} + \tan^2 \varphi_i - m_{MN}^2 = 0 \quad (19)$$

Eq. (19) is a quadratic equation of m_{EG} . By solving this equation, we will know the value of m_{EG} and substituting the value in Eq. (17) we get x_g . The value of y_g is simply d_w . Hence, we know the point $G(x_g, y_g)$.

We next show how to use the above analysis to estimate the coverage area and light intensity.

4.2 Coverage Area

Based on the above analysis, for known water surface function and position of the light source, we can find the refracted ray in underwater at a given surface point. Figure 8 represents a simple case where lines SA and SB are two end rays in the air and the lines AC and BD are the corresponding refracted rays. Thus, if we know points A and B , in this case, we can determine points C and D , respectively, and the line CD contains all the points where the light goes after refraction. Remember this is just one cross-section of the coverage area. As illustrated in Figure 8, let X_1 and X_2 be the points where the lines SA and SB intersect with the x -axis, respectively. For a known beam angle, θ , the distance between the middle point of the line X_1X_2 and either point X_1 or X_2 can be calculated as follows:

$$X_{half} = d_a \tan \frac{\theta}{2} \quad (20)$$

Now, we can easily calculate the position of point X_1 and X_2

$$X_1 \equiv (X_s - X_{half}, 0), \quad X_2 \equiv (X_s + X_{half}, 0) \quad (21)$$

The equation for line SX_1 (or SA) is:

$$\frac{x-x_s}{x_s-x_s+X_{half}} = \frac{y-y_s}{y_s-0} \rightarrow y_s \cdot x - X_{half} \cdot y - x_s \cdot y_s + X_{half} \cdot y_s = 0 \quad (22)$$

By solving Eq. (22) we determine the coordinates of point A . Eq. (22) can only be solved numerically, e.g., by applying the Newton Raphson method. Let's assume initial solution of point A is x_0 then we can iterate and converge to the solution using: $x_{n+1} = x_n - \frac{f(x_n)}{f'(x_n)}$

Similarly, we can determine the coordinates of point B . After calculating the coordinates of the two endpoints, namely, A , and B , we can determine points C , and D using Eq. (17) and Eq. (19). To extend the

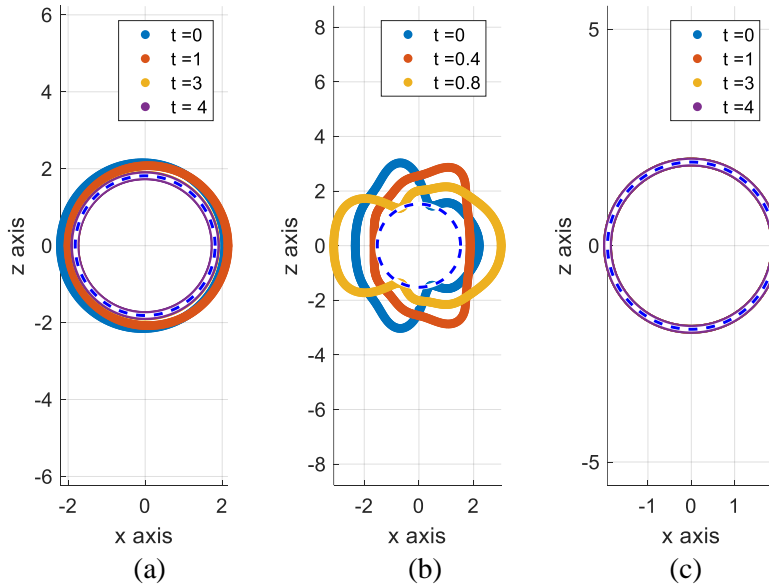


Figure 9: Illustrating the difference between the actual and effective coverage area for (a) shallow water ($H= 1$ m, $T= 5.6$ sec, $\lambda=30$ m and $h= 3$ m), (b) deep water ($H= 0.2$ m; $T = 1.2$ sec; $h= 10$ m), and (c) flat water surface

analysis to 3D, the same steps can be followed to determine the coordinates of all boundary points of the covered underwater area (i.e., a source with the same θ and relative position to the water surface, and the same surface function). This is like rotating the line X_1X_2 horizontally in the x - z plane from 1° to 360° . The accuracy

of the coverage boundary will depend on the radial angle increment. Figure 9 shows examples for such an area based on radial angle increment of 1° . We study the effect of the radial increment later in this section.

The analysis above implicitly assumes that the light source transmits when its position is vertically aligned with the peak of the sinusoidal surface function. However, in practice, such alignment is rare where the water wave always changes with time and consequently the coverage area will vary. Figure 9 shows such variation in the coverage area for both shallow and deep water at different times. The figure also shows the coverage area for the flat-water surface case. For both the shallow and deep-water cases coverage area is randomly changing over time. The variation is less significant for shallow water (Figure 9(a)) because of the high wavelength and relatively low amplitude of the water wave. Figure 9(b) shows the results for the deep-water scenario. In this figure, the coverage area varies significantly due to the low wavelength. Figure 9(c) shows the result of a flat-water scenario. From this figure, we can see there is no change in the coverage area over time which is very much expected for a flat non-varying surface.

It is worth reminding that our goal is to find the underwater area that consistently receives light. Finding such an area is very complex for wavy water surface; therefore, we approximate it using a circle that is centered at the projected position of the light source, and whose radius is the minimum distance from its center to the boundary of the coverage area for all possible phases. We call such a circle the effective coverage area. The dotted circle in Figure 9(a) and (b) reflects the effective coverage and corresponds to the area that always gets light. For a flat-water scenario, Figure 9(c) confirms that effective coverage area and coverage area are the same. Note that in Figure 9 we show the coverage area on the x - z plane, where the transmitter is placed in y -axis at a distance d_a meter above from the water surface level (see Figure 8). Thus, the position of the light source is $(0, d_a, 0)$.

Algorithm and Optimization: *Algorithm 1*

summarizes the steps for finding the effective coverage area. The algorithm iterates over full wave period, T , with an increment of Δt . For each of the considered wave, the coverage area is determined using a cross section (2D plane) and then rotating it from 0° to 360° with an increment of Δr . The value

```
 $r_{eff} = 0$  // The effective radius  $r_{eff}$   
for (time = 0 to  $T$ , step  $\Delta t$ ,)  
– Calculate all underwater point across line  $\overline{CD}$   
– Rotate the axis according to  $\Delta r$  from  $0^\circ$  to  $360^\circ$  in order to determine the coverage area  
–  $R =$  minimum distance of coverage area from the projected position of the light source  
–  $r_{eff} = \min(r_{eff}, R)$   
end for
```

Algorithm 1: Summary of the steps for defining the effective coverage area

of Δr simply determines how accurate (continuity) is the coverage area boundary. For each 2D plain, we calculate the proximity of the boundary points to the projected position of the light source and track the minimum value over all iterations. After considering all times from 0 to T , the minimum distance becomes the radius of the effective coverage area (r_{eff}). The runtime complexity of *Algorithm 1* is $O(\Delta r \cdot \Delta t)$. As mentioned above, the values of Δr vary from 0° to 360° and Δt vary from 0 to T , where T is the period of the water wave function. For example, if $\Delta r = 1^\circ$, $\Delta t = .1$ and $T = 5$ sec, Eq. (22) will be solved $360 \times 50 = 18,000$ times. Obviously, there is a tradeoff where a higher accuracy for determining the coverage area, requires increased computational overhead.

Nonetheless, major optimization can be made if the frequency of the water wave is reasonably high (small period and wavelength), such that the light transmission, i.e., width of the cone base, covers one full cycle of the water wave. Basically, in such a case if Δr is small enough the value of r_{eff} does not change for the various time phases because r_{eff} corresponds to a specific wave amplitude and incident angle. Thus, in this particular case, the light propagation experiences the same wave amplitude and incident angle for all times within T and consequently, we do not need to vary the time phases, i.e., we do not need to run the loop for Δt , which expedites the algorithm execution. It is worth noting that this particular case is expected in almost all practical scenarios; for example, if $d_a = 5\text{m}$, $d_w = 5\text{m}$, and $\theta = 50^\circ$ the coverage area is 40 m^2 which means the diameter of the coverage area is approximately 7m. The coverage area even grows with beam angle and underwater depth as shown in the next section. Figure 9(b) shows the simulation results to capture the effect of Δr when the light

beam covers at least one full period of the water wave. As seen in the figure, for each snapshot the circle touches the corresponding coverage area at least once. Accordingly, we only need to vary Δr to get the r_{eff} for a case where Δr is small enough and the transmitter beam angle θ is large enough so that the light covers at least one full cycle of the water surface wave. The effect of Δr on r_{eff} is highlighted in Figure 10, where increasing Δr causes a major decline in

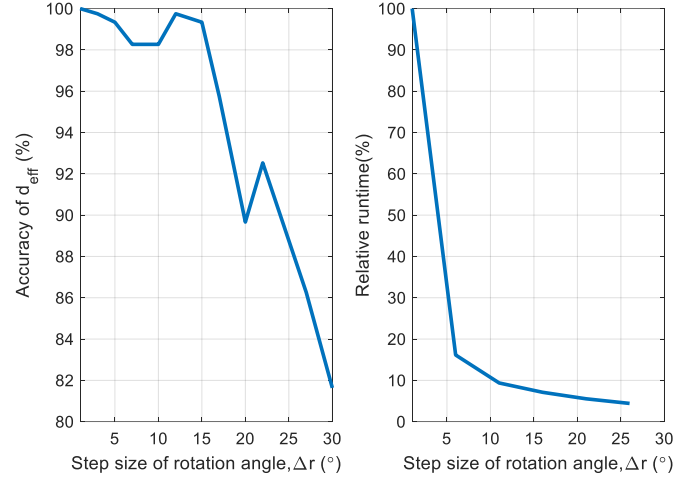


Figure 10: Effect of step size of rotation angle on accuracy of r_{eff} and runtime of the algorithm. Note that relative runtime means in comparison to the case where $\Delta r = 1$

the runtime complexity and a slight decrease in accuracy. A setting of Δr up to a value of 5 will have an unnoticeable impact on accuracy while dropping runtime by 27% relative to $\Delta r = 1$.

No optimization is required for a flat-water surface scenario because the algorithm needs to run only once to determine the coverage area.

4.3 Light Intensity

In the air, if we know the distance that light travels, then it is very easy to find the intensity. Using the location of points S , E and G , in Figure 8, we can easily calculate the distance between them.

$$\overline{SE} = \sqrt{(x_e - x_s)^2 + (y_e - y_s)^2} \quad (23)$$

$$\overline{EG} = \sqrt{(x_e - x_g)^2 + (y_e - y_g)^2} \quad (24)$$

However, the light intensity at point G depends not only on the distance but also how much light is penetrating the surface to the water, i.e., we need to know the transmittance, τ_l and reflectance, η_l of the water surface.

The relation between τ_l and η_l is:

$$\tau_l = 1 - \eta_l \quad (25)$$

Now, the reflectance η_l depends on the incident and transmittance angle and polarity of the light source. If the light source is not polarized, then we can express reflectance as follows:

$$\eta_l = \frac{\eta_s + \eta_p}{2} \quad (26)$$

where η_s and η_p are the reflectance coefficients of s -polarized light and p -polarized light, respectively. To determine η_s and

η_p , Fresnel equation can be used. If n_a and n_w are the refractive indexes of air and water respectively, then using Fresnel equation η_s and η_p are:

$$\eta_s = \left| \frac{n_a \cos \theta_i - n_w \cos \phi_i}{n_a \cos \theta_i + n_w \cos \phi_i} \right|^2 \quad \text{and} \quad \eta_p = \left| \frac{n_a \cos \phi_i - n_w \cos \theta_i}{n_a \cos \phi_i + n_w \cos \theta_i} \right|^2 \quad (27)$$

Using Eq. (25), (26), and (27) we can show in Figure 11 the relationship between reflectance and transmittance and the incident angle. Figure 11 indicates for incident angle below 60° , the transmittance τ_l is almost one.

After measuring the distances and calculating transmittance, we find the intensity at point G in Figure 8. Let's assume, I_e is the intensity at point E which is just above the water surface and I_{ew} is the intensity just below the water surface at the same point. I_e and I_{ew} can be calculated as follows,

$$I_E = \frac{2\pi}{\theta} \cdot \frac{P}{4\pi \cdot SE^2} \quad (28)$$

$$I_{ew} = \tau_l \cdot I_e \quad (29)$$

where P is the power of the light source at point S. The intensity I_{ew} will decrease as light travels in the water depending on the beam attenuation coefficient, k (m^{-1}), of light in the water medium.

Thus, the light intensity at point G after traveling \overline{EG} distance in water can be calculated using Beer's law as [58]:

$$I = I_{ew} \cdot e^{-k(EG)} \quad (30)$$

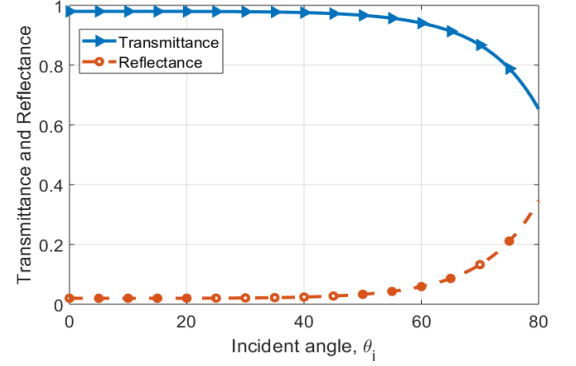


Figure 11: Relationship between transmittance and reflectance and the incident angle

Generally, the value of k depends on the biological factors of water and absorption, $a(m^{-1})$ and scattering, $b(m^{-1})$ coefficient. A detailed analysis of how we can calculate the value of k has been given in Appendix A. Eq. (30) is valid when no scattered light is recollected. However, some portion of the scattered light may reenter into the receiver FOV. In Appendix A, we have also shown how to calculate the recollection of the scattered light using Eq. (97). In that calculation, a scattering factor n ($0 \leq n \leq 1$) is used to recollect scattered light. This scattering factor is a

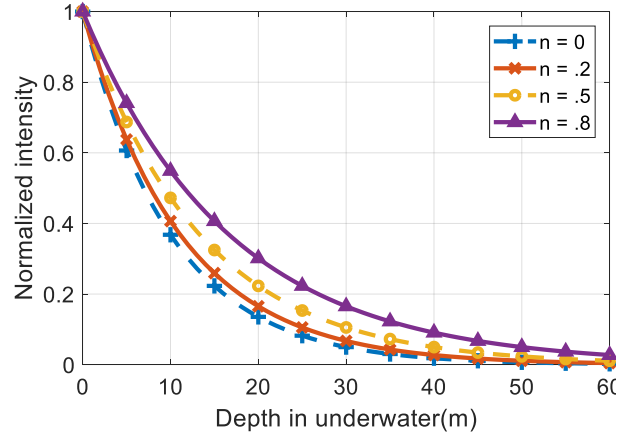


Figure 12: Effect of scattering factor, n on the light propagation

function of the water optical properties (i.e., absorption, scattering, and total attenuation) and system parameters (i.e., receiver polarization state, aperture, FOV, and initial laser beam radius and divergence). Figure 12 illustrates the effect of the scattering factor on light intensity. In this figure, the y-axis reflects the intensity at a specific depth of water relative to the intensity at the water surface. As shown in Figure 12, the intensity of the light grows with the increase of the scattering factor. In the figure, $n = 0$ corresponds to the case when no scattering light is collected. How to determine the absorption, scattering and scattering factors can be found in [59][60][61]. Assuming that the values of these factors are known, we will calculate the light intensity in underwater, e.g., at point G. Using Eq. (28), (29) and (30), the light intensity at point G will be:

$$I = \frac{2\pi P}{4\pi\theta} \cdot \tau_l \cdot \frac{1}{SE^2} \cdot e^{-k \cdot (EG)} \quad (31)$$

Eq. (31) provides the intensity at point G. If we know all points at the water surface, i.e., surface function, we can find the intensities at all points covered by the light sources at depth d_w .

Intensity for a flat surface: For a flat-water surface, Eq. (31) can be simplified. When incident angle, θ_i is minimum, i.e., zero, the distances \overline{SE} and \overline{EG} become minimum, specifically, $\overline{SE} = d_a$ and $\overline{EG} = d_w$. In this case, the intensity is maximum. Reflecting this condition in Eq. (31) we can get the maximum intensity I_{max} for a flat-water surface as follows:

$$I_{max} = \frac{2\pi P}{4\pi\theta} \cdot \tau_l \cdot \frac{1}{d_a^2} \cdot e^{-k \cdot (d_w)} \quad (32)$$

The minimum intensity, I_{min} , corresponds to $\theta_i = \theta/2$ and $\varphi_i = \varphi$. In this case \overline{SE} and \overline{EG} become maximum where $\overline{SE} = \frac{d_a}{\cos\frac{\theta}{2}}$ and $\overline{EG} = \frac{d_w}{\cos\varphi}$. Reflecting this condition in Eq. (31), I_{min} for flat water surface will be:

$$I_{min} = \frac{2\pi P}{4\pi\theta} \cdot \tau_l \cdot \frac{1}{\left(\frac{d_a}{\cos\frac{\theta}{2}}\right)^2} \cdot e^{-k \cdot \left(\frac{d_w}{\cos\varphi}\right)} \quad (33)$$

Using *Algorithm 1* we can find the coverage area and using Eq. (31), (32), and (33) we can calculate the intensity on that area. Figure 13 shows such theoretical relation between coverage area and intensity for a flat-water surface, where d is the diameter of the coverage area. From this figure we can see, the light is confined within a circle with diameter d for a specific beam angle, θ . The intensity is zero outside, maximum (I_{max}) in the middle (center) and minimum in the edges (I_{min}) of this circular area. By controlling θ , d_a , d_w , and P , the value of d , I_{max} , and I_{min} can be varied. In the next section, we leverage the above analysis of a single light source to study the cases of multiple beamformed light sources.

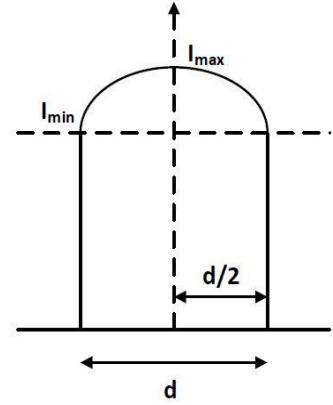


Figure 13: Relation between coverage area and intensity for single light source.

Chapter 5: Multiple Beamformed Light Sources

In the previous chapter, as we analyzed the underwater coverage and intensity for a single light source, the coverage area inside the water mainly depends on the light source beam angle, θ where the coverage usually grows with the increase of θ . On the other hand, the light intensity within the covered underwater area depends on both light source power, P and θ . If P is constant, the light intensity diminishes with the increase of θ . We are particularly interested in I_{min}

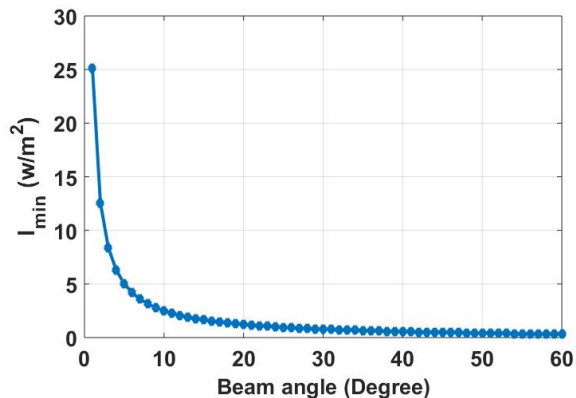


Figure 14: Changes of I_{min} for different beam angles of a single light source. The plot is based on setting $d_a = 10\text{m}$, $d_w = 10\text{m}$ and $p = 100\text{w/m}^2$.

because it reflects the ability of an optical receiver to successfully receive a transmission. Using Eq. (33) we can determine the relation between I_{min} and θ , which has been shown in Figure 14. From this figure, it is obvious that I_{min} decreases quickly when broadening the angle θ . On the other hand, having a large coverage area is also an important factor for successful transmission because of the uncertainty of the underwater node position due to the water current. Thus, there is a tradeoff between coverage area and intensity.

Through our analysis in this chapter, and the simulation results in the next chapter, we will show how to increase the gain in both the coverage area and intensity using the same total transmission power distributed into multiple light sources, as illustrated in Figure 15. We call it beamforming multiple light sources. In optical beamforming, the coverage area of multiple light sources overlaps inside the water and the light intensity on that region becomes the sum of the individual light sources capable of reaching to same area. Maintaining higher coverage area using optical beamforming has some other advantages as well. In [62], a secure downlink transmission communication link has been made using multiple light inputs by designing transmit beamformers that maximize the achievable secrecy rate. Moreover, a higher signal-to-interference-plus-noise ratio (SINR) is possible using beamforming. In [63] a multi-element VLC transmitter architecture for different

configurations is proposed. Multi-element transmitters with three, seven, and nineteen LEDs are compared with a single light transmitter in terms of SINR and illumination. The transmitter configuration with three LED has been found to yield the best performance for simultaneously achieving good illumination and SINR distribution.

5.1 Positioning of Multiple Light Sources

Based on the analysis in the previous section for a single light source, here we study the positioning of multiple beamformed light sources so that the size of coverage area is maximized while keeping the intensity level throughout the covered area sufficiently high for good SINR. We distribute the same power P which is used for the baseline setup of a single light source, among the beamformed transmitters. For example, if we have four beamformed sources, each is allocated power of $P/4$. It should be noted that if there is no power budget, i.e., one can use the same power P for all transmitters, the positioning problem becomes finding coverage patterns with least overlaps, which has been extensively used in the realm of sensor networks [64]; with the constrained total power budget, the problem becomes more complicated due to the coverage and intensity tradeoff as discussed at the beginning of this subsection. Thus, we opt to find the best number of beamformed transmitters and determine their positions relative to one another, i.e., deployment pattern.

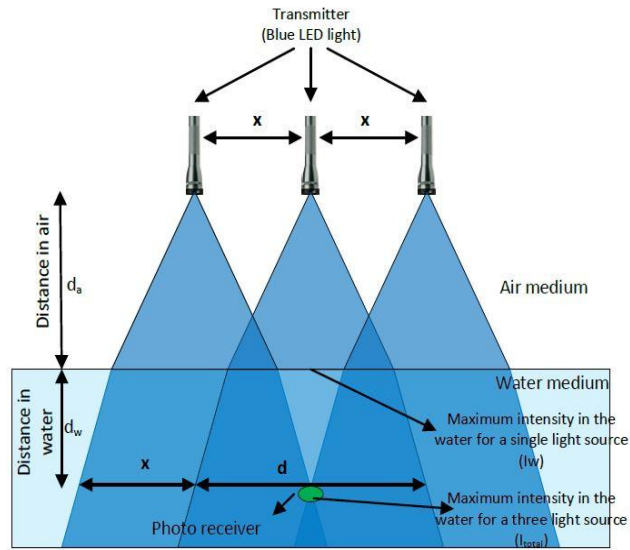


Figure 15: Communication through the air-water interface using multiple light sources

Conventional node placement for maximized coverage opts to employ the least number of nodes; thus, the objective is to minimize overlap among the regions covered by the individual nodes. Fundamentally a placement pattern is determined, and the entire deployment area is then tiled using such a pattern. In the realm

of sensor networks, an equilateral triangle has been shown to achieve optimal results, where sensors of disc-shaped ranges are placed on the vertices of the triangles [64]. In such a pattern, there is no point in the triangle that is covered by more than 2 sensors. However, for distributed beamforming, the placement pattern of the light sources should ensure the presence of a commonly covered region, i.e., a region that is covered by multiple beamformed sources, in order to enable the establishment of highly reliable communication links for the underwater receiver located in such a region. Figure 16 shows sample beamforming patterns for varying count and positions of light sources. As seen in the figure, the intensity in areas with non-overlapped coverage, i.e., I_{min} , diminishes with the increased number of sources, which ultimately leads to weaker SINR. Thus, it is important to have areas with maximal overlap among the sources.

Another important factor is the size of maximal coverage for the placement pattern; this is important to mitigate uncertainty about the location of the underwater nodes where water current causes the node to drift while communicating with the beamformed sources and between consecutive data sharing sessions with the

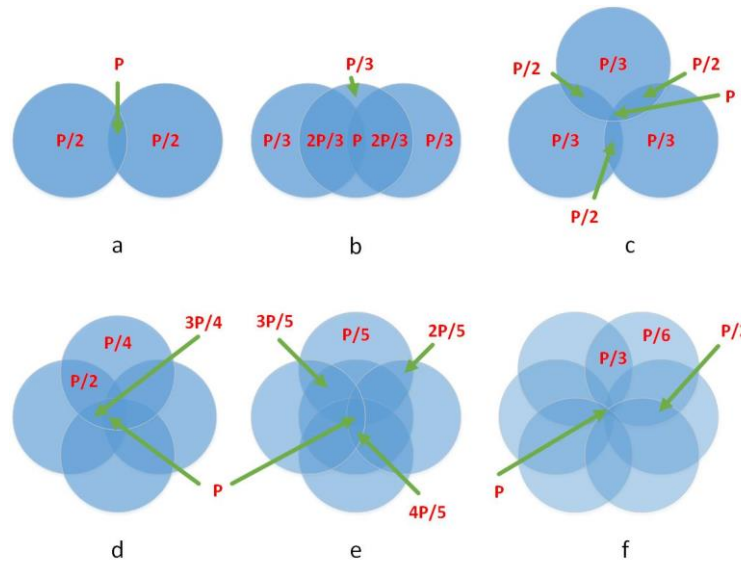


Figure 16: Sample arrangement for: (a) two, (b) three in straight line, (c) three in triangular, (d) four, (e) five, and (f) six light sources. Same power ‘P’ is equally split among all sources.

airborne unit(s). Based on such a criterion, the placement pattern in Figure 16(b) is better than that in Figure 16(c) for three beamformed sources, despite the fact that the pattern of Figure 16(c) yields better coverage. Fundamentally, the pattern in Figure 16(b) has two advantages in our particular application. Firstly, as water

current can cause an underwater receiver to drift away in one direction, the three light sources can be easily aligned in that direction. Secondly, due to the increased overlap in the central region, we can use that region for establishing a highly robust communication link between the airborne unit and the underwater node, i.e., we have a larger area that experiences I_{max} . With the increased number of light sources, it becomes quite difficult and inflexible to reposition the individual sources to cope with underwater drifts; especially the coverage area becomes more diverse in terms of the number of overlapped light sources. Furthermore, the splitting of the total power on many sources will diminish I_{min} and thus the increased coverage could more or less become illusive in this case since the receiver will experience low SINR in areas covered by few sources. For example, in Figure 16(f) areas covered only by one source will experience I_{min} that is 1/2 that of those covered by one source in Figures 16(b) and 16(c).

5.2 Analysis of Three Beamformed Light Sources

As concluded above, the collinear positioning of three light sources, shown in Figure 16(b), is deemed the most suitable arrangement for beamformed transmission across the air-water interface. This subsection analyzes the effect of the inter-source proximity on the coverage and light intensity for both flat and wavy water surfaces.

Flat Water Surface: From Figure 15, the distance between two light sources is denoted by x , and the diameter of the coverage area of a single light source is referred to by d . We can calculate the total coverage area, C at d_w meter depth for three collinear light sources as follows:

$$C = 3\pi \left(\frac{d}{2}\right)^2 - d^2 \cos^{-1} \left(\frac{d-x}{d}\right) + (d-x) \sqrt{d^2 - (d-x)^2} \quad (34)$$

Table 2. Relation between total coverage and inter light source distance.

Distance (x)	Total coverage (C)
$d/2$	$3\pi\left(\frac{d}{2}\right)^2 - d^2 \cos^{-1}\left(\frac{1}{2}\right) + \frac{\sqrt{3}}{4}d^2$
0	$\pi\left(\frac{d}{2}\right)^2$
$0 < x < d/2$	$\pi\left(\frac{d}{2}\right)^2 < C < 3\pi\left(\frac{d}{2}\right)^2 - d^2 \cos^{-1}\left(\frac{1}{2}\right) + \frac{\sqrt{3}}{4}d^2$

The light intensity at any point within the C is the sum of the light intensity of individual light sources. If the intensity at any point at d_w meter depth for three light sources are I_1 , I_2 , and I_3 , respectively, then Total intensity, I_{total} on that point is:

$$I_{total} = I_1 + I_2 + I_3 \quad (35)$$

Using Eq. (34) we can calculate the coverage area for different inter-light sources distances, as shown in Table 2. We will study the coverage area and light intensity on that area more through simulation in the next section.

Wavy Water Surface: Using Algorithm 1, we can find the effective diameter of the coverage area for a single light source. Let's assume for some given parameter the diameter of the effective coverage area is d_{eff} and again if the distances between light sources are Δ meters, then we can get the coverage area for three light sources using Eq. (34) as:

$$C_{eff} = 3\pi\left(\frac{d_{eff}}{2}\right)^2 - d_{eff}^2 \cos^{-1}\left(\frac{d_{eff}-x}{d_{eff}}\right) + (d_{eff} - \Delta) \sqrt{d_{eff}^2 - (d_{eff} - \Delta)^2} \quad (36)$$

The value of d_{eff} depends on the water wave amplitude and frequency hence C_{eff} also depends on the water surface function. In the next section, we will study Eq. (36) through simulation. For intensity calculation again if we know the intensity at a specific point for every single light source then the total intensity is simply the sum of all those intensities like Eq. (35).

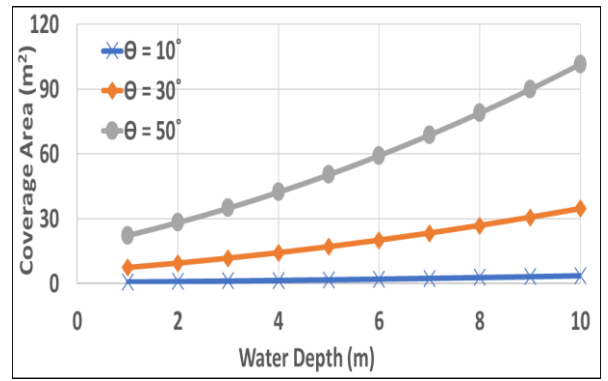
Chapter 6: Validation Results of VLC Communication

In this chapter, the coverage area and light intensity inside the water is extensively studied using MATLAB. The simulation is done for various surface wave parameters, beam angle (θ), and for various values of d_a and d_w . In addition, a lab experiment has been conducted to validate the simulation results. Simulation is done for both wavy and flat surface. We will start with the flat surface simulation and experiment, and then show the result for a wavy surface.

6.1 Simulation for a Flat Water Surface

The intensity and coverage area calculation are quite different depending on the surface function (flat or wavy). In this subsection, we present the results for a flat-water surface for both single and multiple beamformed light sources.

Single light source: The effect of θ and d_w on the light intensity and coverage have been captured first for a single light source. Again, keep in mind that the coverage area is measured by tracking the diameter d of the coverage area for a single light source, i.e., $d = \overline{CD}$ in Figure 1. In this simulation, the transmitted power, P is set to 30 mW and attenuation coefficient of water, $k = 0.1$ ($a = .05$, $b = 0.05$), $n = 0$ (no scattered light is collected). Moreover, we assume that transmittance, τ is constant and equals to 0.97 for all incident angles less than 60° , as explained in Figure 11. The value of d_w has been varied from 1 to 10 meters to track down intensity and coverage area while keeping



(a)

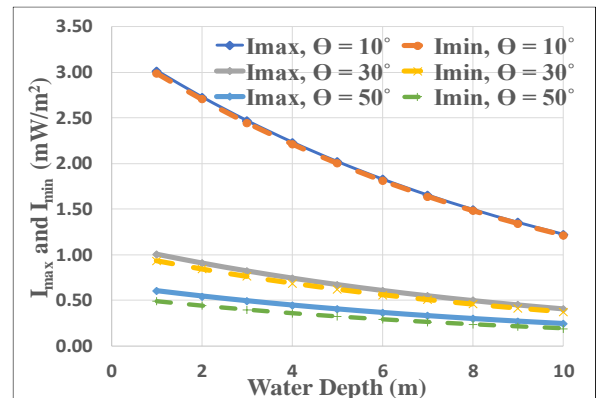


Figure 17: The coverage and light intensity at various underwater depth for a single light source placed in air at a height, $d_a = 5$ m, from the water surface with beam angle, $\theta=10^\circ, 20^\circ,$ and 50°

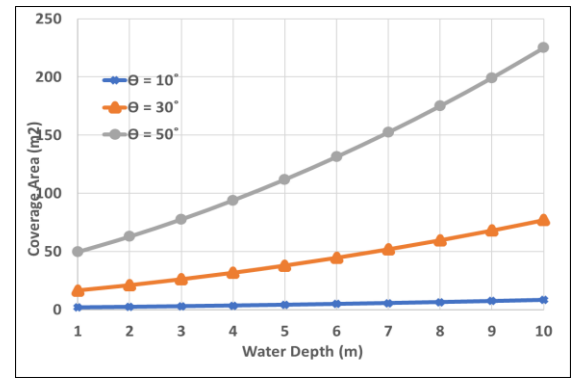
d_a fixed for different θ ($\theta = 10^\circ, 30^\circ,$ and 50°). The results are plotted in Figures 17(a) and 17(b).

Figure 17(a) shows the relation between the size of the coverage area and water depth for various θ . The results indicate that θ has a dramatic effect on coverage. For small values of θ , the coverage area is very small which is risky since the underwater node may drift away from that small coverage area due to the water current. A large value of θ clearly gives better coverage, particularly for increased water depth.

On the other hand, Figure 17(b) shows the relationship between I_{min} and I_{max} with θ and d_w . As expected, the light intensity is higher for smaller beam angles. The intensity diminishes rapidly for larger beam angle, especially the gap between I_{min} and I_{max} grows with the increased value of θ . Overall, the plot confirms the tradeoff between coverage and intensity which has been discussed in the previous section.

Beamformed sources: Figure 18 shows the same analysis for the multiple light sources. Here all parameter

has been set exactly the same as the single light source except the total power P , where the total 30 mW has been divided equally among the three light sources. The inter-distance x between light sources has been set to $\frac{d}{2}$. Figure 18(a) and 18(b) shows the results for coverage and light intensity. When comparing Figure 17(a) and 18(a), it is obvious that beamforming multiple light sources almost doubles the coverage area for the same θ and d_w . It is very important for tolerating node drifts and thus enabling the establishment of robust communication links. Figure 18(b) shows the result of light intensity. The figure shows that beamforming does not affect the I_{max} , yet I_{min} is significantly less than the Figure 17(b), which is very much expected since the transmission power of each of the three sources is 1/3 that of the single



(a)

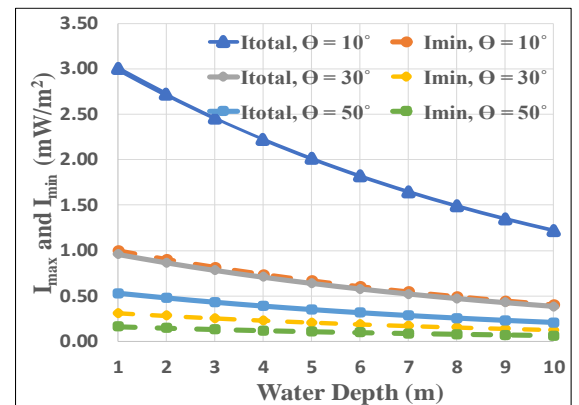


Figure 18: The effect of underwater distance on the coverage and light intensity for three collinear beamformed light sources places at height $d_a = 5\text{m}$ above the water surface.

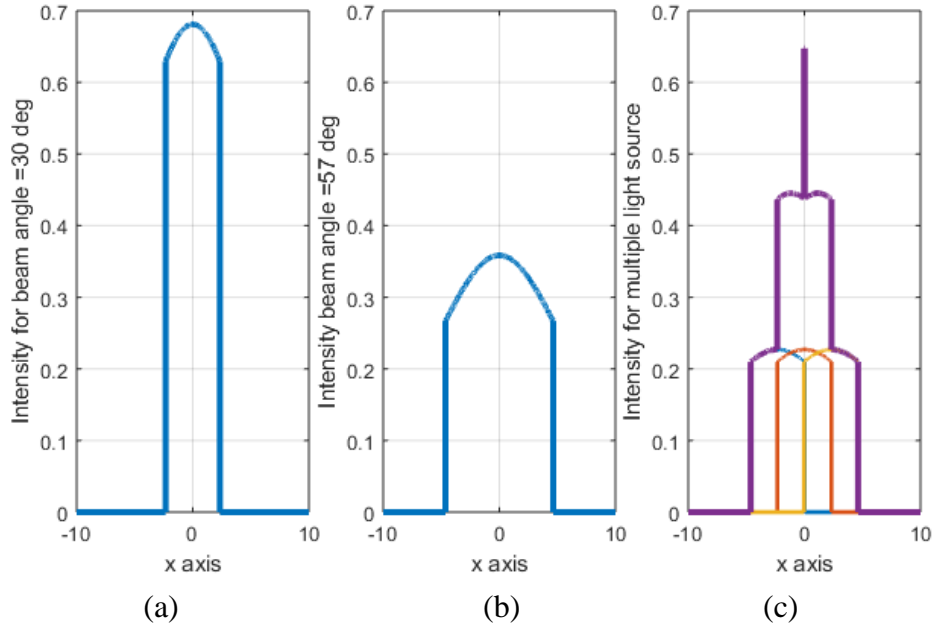


Figure 19: Comparison of intensity and coverage area for a single light source with different beam angles in (a), and (b), and for three beamformed sources in (c), where $d_a = 5\text{m}$ and $d_w = 5\text{m}$.

source used for Figure 18(b). In practice, I_{min} is very important and determines the number of sources and the total power since it affects the SINR.

Figure 19 opts to highlight the benefit of multiple light sources. The coverage is measured using the diameter of coverage area in the x -axis, while the intensity is reported in the y -axis. Figure 19(a) shows the light intensity and coverage for a single light source with $d_a = 5\text{m}$ and $d_w = 5\text{m}$, $\theta = 30^\circ$ and $p = 30\text{mW}$. For such configuration, the diameter of the coverage area is 4.66m. In Figure 19(c), the plot for beamformed sources is shown for the same d_a , d_w , and θ settings, where the 30mW power is divided equally among three light sources. In this case, the diameter of the coverage area is 9.26m, which is almost double the value for a single source with the same power in Figure 19(a). If we want to achieve the same coverage with only a single light source, a bigger beam angle of 57° is needed, as shown in Figure 19(b). In other words, Figures 19(b) and 19(c) are equivalent in terms of coverage. In addition, the minimum intensity in both Figures 19(b) and 19(c) is almost the same. Thus, with multiple light sources, we get a coverage area which holds high intensity. This is very important in case of turbid water because turbid water reduces the light intensity. Thus, the beamformed light sources configuration provides better SNR in this case.

6.2 Wavy Surfaces

Most of the time, the water surface is not flat where waves form due to the wind and earth gravity. We have used Eq. (1) and Eq. (4) to generate a wavy water surface. In this subsection, we discuss the simulation results for a wavy water surface for both single and multiple light sources.

A water surface wave has two important parameters, namely, wave amplitude and the time when the water surface function is captured. Such time can vary from 0 to the wave period, T . We have analyzed the effect of both parameters on the intensity when a single light source is used. In this simulation, the source is placed 5m above the water and the receiver is assumed to be at 5m depth, i.e., $d_a = 5\text{m}$ and $d_w = 5\text{m}$. Figure 20 shows the results when the water wave's amplitude is changed between, 0 (flat), 0.1, 0.3 and 0.4 meters. The plot reflects the intensity assuming a cnoidal shaped surface at zero time, i.e., the peak of the wave is vertically aligned with the light source. We can see intensity spreads almost equally within the coverage area for low amplitude, which means there is less deviation between the maximum and minimum intensity.

Water surface function always changes with time. Figure 21 shows the effect of time on light intensity when a single source is employed. The time can vary from 0 to wave period, T . Figure 21 shows the results for the time of 0, 0.5, and 0.8 sec, where the area covered by the light inside water always varies in accordance

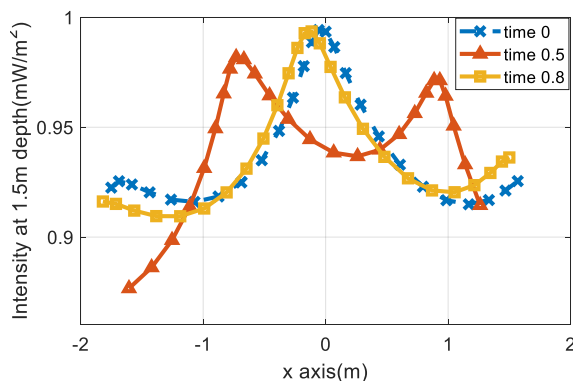


Figure 21: Effect of instantaneous time on intensity for single light source

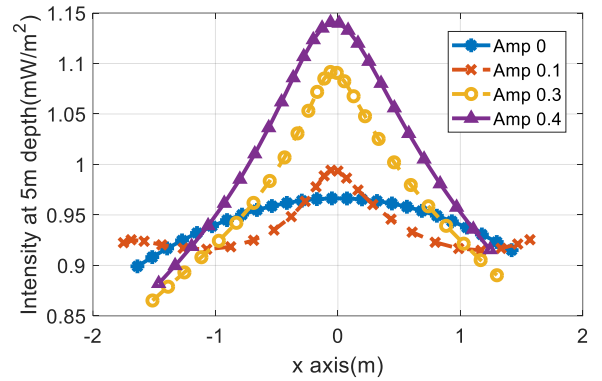


Figure 20: Effect of water surface wave's amplitude on intensity for single light source

with time, as illustrated also in Figure 9.

The interest is in the effective coverage area which is covered by light all the time. Figure 22 shows the effective coverage area when applying Algorithm 1. For different θ ($\theta = 20^\circ, 30^\circ, \text{ and } 50^\circ$), Figures 22(a) and 22(b) provide the results for single and multiple light sources, respectively. When comparing Figures 22, 17(a) and 18(a),

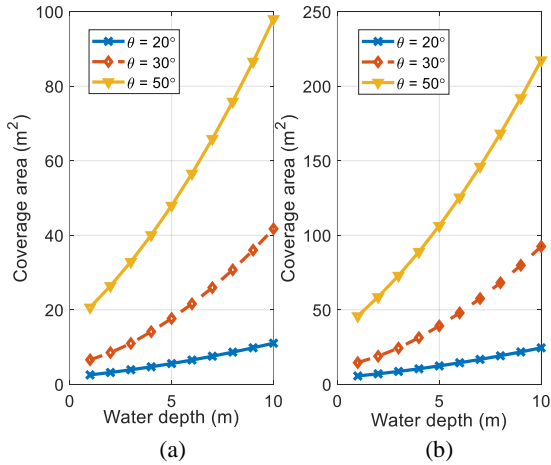


Figure 22: Coverage area in presence of water waves for both (a) single and (b) multiple light sources

is expected given the increased scattering of light rays. Again, the use of multiple beamformed sources will yield better coverage; yet the effect of wave amplitude is consistent.

For multiple light sources, we have repeated analysis of Figure 19 in presence of water waves. Again, we have considered same parameters as used for flat water surface ($d_a = 5\text{m}$, $d_w = 5\text{m}$, $p = 30\text{mW}$ for a single light source, and 10 mW for each of the three beamformed light sources). Figure 24 shows the simulation results for water wave’s amplitude 0.3m . This figure is identical with Figure 19 except there are variations in the intensity between the maximum and minimum intensity due to the presence of surface waves.

6.3 Lab Experiment

In order to validate the theoretical analysis and simulation results, a lab experiment has been conducted using a $122\text{cm} \times 46\text{cm}$ water tank. The tank is made of clear glass. Given the size constraint of the water tank, it is not possible to generate significantly sized water waves that cause measurable impacts on the light intensity inside the water. Therefore, we conducted our lab experiment only for a flat-water surface. We have used blue LED light, which has the

the effective coverage area is always smaller than the coverage area for a flat-water surface for both single and multiple light sources. Figure 23 shows the difference between coverage areas for single and multiple light sources for varying wave amplitude. Note that zero amplitude corresponds to a flat-water surface. As evident from the figure, the coverage area diminishes with the increase of wave amplitude, which is

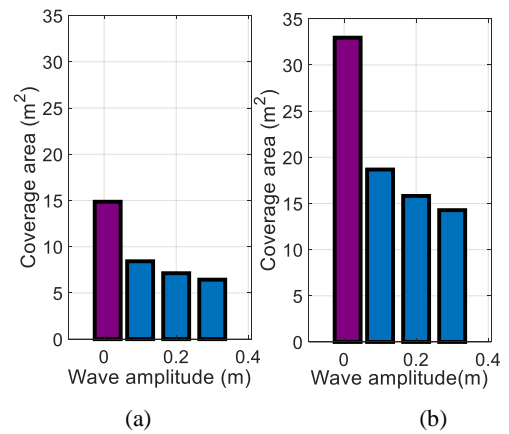


Figure 23: Changes in coverage area for different wave amplitude for (a) Single light source, (b) three beamformed sources.

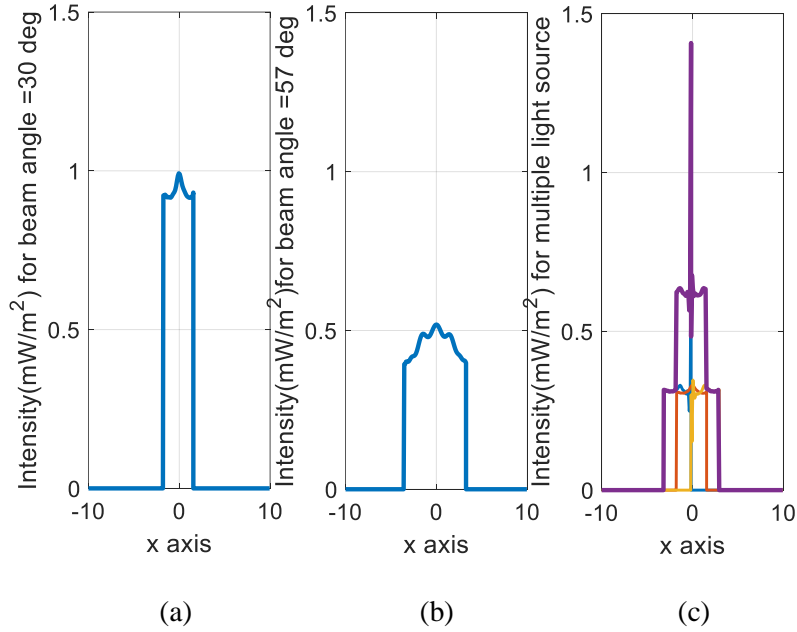


Figure 24: Comparing intensity and coverage area for both single (a), (b) and multiple light sources (c) at $d_a = 5\text{m}$ and $d_w = 5\text{m}$ for wavy water surface.

lowest attenuation coefficient in the water, as mentioned earlier. As a light source, we have used WAYLLSHINE® Zoomable Scalable CREE LED 3 Mode 200 Lumen 150 Yard Flashlight, which can be configured for different beam angles. As a photodetector 10mm^2 PIN detector (PC10-6b TO) has been used since it has a high response for blue LED light. In the experiment three light sources have been used with 10

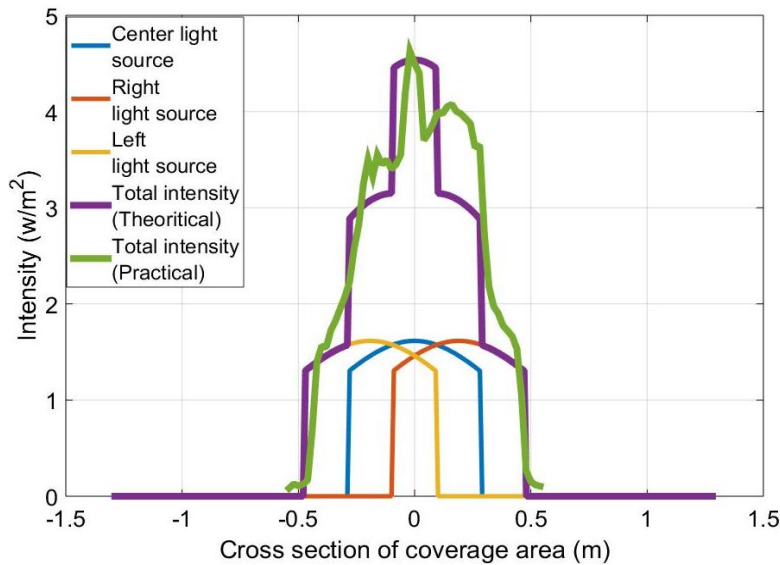


Figure 25: Experimental and theoretical results for light intensity at $d_a = 0.25\text{m}$ and $d_w = 0.46\text{m}$, with $\theta = 52^\circ$

mW power each. The water attenuation coefficient, k is measured and found to 0.1 m^{-1} . Due to the small room and tank size, the experiment is done with $d_a = 0.25\text{m}$ and $d_w = 0.46\text{m}$. The beam angle is set to 52° , which is found to provide maximum coverage area inside the water tank for the above value of d_a and d_w . The experiment is done under dark setting to avoid the ambient noise from external light sources. Both the experimental and simulation results are shown in Figure 25. From this figure, we can see the experimental results almost match those obtained via simulation.

Chapter 7: Modulation: Adaptive DPPM

After doing extensive analysis on coverage area and intensity of a VLC system, we gear our research toward focusing on a suitable modulation technique for such kind of application. In chapter 2 we have mentioned that DPPM is the most suitable modulation technique for VLC operation across the air-water interface. We have also discussed changing M dynamically in DPPM is very important for the VLC links. However, if the transmitter module changes the value of M dynamically, it will not be possible for the receiver to demodulate the DPPM data. In this chapter, we design a novel frame structure which contains the information of M so that the receiver module can decode the received signals. This frame structure also helps in detecting error within a frame. We call this Adaptive DPPM (ADPPM) frame since it contains the information of M and changing the value of M will not hinder correct reception. We will first design a frame structure for the proposed ADPPM protocol and then develop an algorithm for fitting the encoded data in such a frame structure. We also show how this frame structure can be decoded. Finally, we propose an additional algorithm for determining the appropriate value of M , and consequently the symbol size L .

7.1 Frame design



Figure 26: ADPPM frame structure

Figure 26 shows our proposed ADPPM frame structure. In this frame, the payload is the modulated version of the actual message data. If D_m is the data size of the actual message, then the maximum and minimum payload can be calculated as follows:

$$P_{max} = 2^M \times \frac{D_m}{M} \text{ and } P_{min} = \frac{D_m}{M} \quad (37)$$

Delimiters: A guard band, G , is added before and after the payload. At the end of the frame, another guard band is added to inform the receiver about the frame boundary; recall the frame size of DPPM is variable. Theoretically, the bit pattern for G could be anything as long as the transmitter and receiver know it. Obviously, a similar bit pattern may appear in the payload and additional information may be included to distinguish guards from data, as we explain below. Generally, the size of G , denoted $|G|$, is subject to tradeoff. Using a large bit pattern for G will diminish the probability of having a similar pattern within the payload, and vice versa. In our approach, if the same pattern appears in the payload, an additional zero is appended to such a pattern in the payload. For example, if G is picked to be ‘0110’, any time the pattern ‘0110’ appears in the payload, an additional zero is inserted in the middle making it ‘01010’ instead. A field, called $EZPs$, is included in the frame to identify the added zeros due to matching the guard G within the payload. Basically, $EZPs$ contains the position of all those extra 0’s. If ezp represents the position of only one extra 0, $EZPs$ can be expressed as follows:

$$EZPs = ezp \times N_0 \quad (38)$$

Where N_0 denotes the number of extra 0’s. The size of each ezp depends on the P_{max} since it represents the maximum size of the payload. For example, if maximum size of payload, $P_{max} = 128$ bits, we need at least 7 bits to represent each extra 0 position. We can express this as follows:

$$ezp = \log_2(P_{max}) = \log_2 \left(2^M \times \frac{D_m}{M} \right) \quad (39)$$

Thus, the size of $EZPs$ varies depending on the value of N_0 . The maximum value of N_0 , denoted $N_{0,max}$, corresponds to the case that all consecutive groups of $|G|$ bits in the payload matches the bit pattern of G .

$$EZPs_{min} = 0 \quad \text{and} \quad EZPs_{max} = ezp \times N_{0,max} \quad (40)$$

It is important to note that distinguishing the payload from G is essential only for the guard band after the payload in the frame since it can cause confusion about when the payload field actually ends. Therefore, overlapped matches of G within the payload is not warranted. Thus,

$$N_{0,max} = \left\lfloor \frac{D_m}{|G|} \right\rfloor \quad (41)$$

Determining M : In addition to $EZPs$, we also introduce an extra field, namely, NOP to enable correct demodulation. NOP , which stands for number of 1's in the data payload. Such a field is necessary to inform the receiver about the value of M used by the transmitter. Assume that N_1 is the number of 1's that the data payload. Given that DPPM sends only one "on" pulse for each M bits, N_1 can be calculated as follows:

$$N_1 = \frac{D_m}{M} \quad (42)$$

Thus, the size of the NOP is

$$NOP = \log_2 \left(\frac{D_m}{M} \right) + 1 \quad (43)$$

The size of the NOP is fixed and is determined based on the maximum value of N_1 , which corresponds to the minimum value of M that will be used in communication. If D_m is fixed, by knowing the decimal value in the NOP field in the frame, the receiver can estimate the value of M from Eq. (42).

7.2 Protocol Efficiency

In the frame, anything other than the payload is called overhead. Thus, the overhead for our proposed frame structure is:

$$Overhead = 3|G| + NOP + EZPs \quad (44)$$

Substituting the value of NOP and $EZPs$ from Eq. (38), and (43) we get:

$$Overhead = 3|G| + \log_2 \left(\frac{D_m}{M} \right) + 1 + ezp \times N_0 \quad (45)$$

Now, by knowing the payload and overhead we can calculate the protocol efficiency, η of the communication system as follows:

$$\eta = \frac{\text{Data size}}{\text{Payload} + \text{Overhead}} \quad (46)$$

This protocol efficiency, η is very important to understand the maximum value of message data, D_m that should send in one frame. It also tells us how effectively we can design a data frame. We want this as big as possible. The largest η is when the payload, and overhead is at minimum. From Eq. (37) we can get the minimum payload. Eq. (40) indicates that the overhead is minimum when $EZPs = 0$, i.e., when payload contain no guard pattern, G . Thus,

$$\eta_{max} = \frac{D_m}{\frac{D_m}{M} + 3|G| + \log_2\left(\frac{D_m}{M}\right) + 1} \quad (47)$$

Meanwhile, the minimum value of η corresponds to maximum overhead and payload, and will be:

$$\eta_{min} = \frac{\text{Data Size}}{\text{Payload}_{max} + \text{Overhead}_{max}} \quad (48)$$

Using Eq. (40), (41), and (45), the maximum overhead.

$$\text{overhead}_{max} = 3|G| + \log_2\left(\frac{D_m}{M}\right) + 1 + \text{ezp} \times \left\lfloor \frac{D_m}{|G|} \right\rfloor \quad (49)$$

From Eq. (37) the maximum size of payload is $2^M \times \frac{D_m}{M}$. However, we need to note that the payload may contains zeros due to matches of G with the data bits; in the worst cases the bit pattern of the data is simply a sequence of matches of G and $N_{0,max}$ bits are added. Therefore, the maximum payload is further updated to factor in the situation when N_0 is maximum, i.e., using Eq. (41). Thus,

$$\text{Payload}_{max} = 2^M \times \frac{D_m}{M} + \left\lfloor \frac{D_m}{|G|} \right\rfloor \quad (50)$$

Substituting overhead_{max} and Payload_{max} from Eq. (40), (49) and (50) into Eq. (48), we can derive formula for η_{min} .

$$\eta_{min} = \frac{D_m}{3|G| + \log_2\left(\frac{D_m}{M}\right) + 1 + \log_2\left(2^M \times \frac{D_m}{M}\right) \left\lfloor \frac{D_m}{|G|} \right\rfloor + 2^M \times \frac{D_m}{M} + \left\lfloor \frac{D_m}{|G|} \right\rfloor} \quad (51)$$

From Eq. (47) and (51) we can note that the maximum and minimum protocol efficiency mainly depends on the message data length, D_m and M . Such a relation is captured in Figure 27. From this figure we can see that for large values of D_m , η_{min} and η_{max} do not depend that much on M . On the other hand, for smaller D_m , growing M boosts η_{max} and diminishes η_{min} . At this point we need to keep in mind that though higher D_m give us slightly better protocol efficiency, it also makes the frame size bigger which means if there is any error, we need to send that bigger frame again which eventually decreases the bandwidth efficiency. Therefore, we need to choose D_m as low as possible which also provides reasonable protocol efficiency. For example, if $D_m = 32$ bits, we get reasonable protocol efficiency, when $D_m < 32$ the maximum protocol efficiency drops drastically.

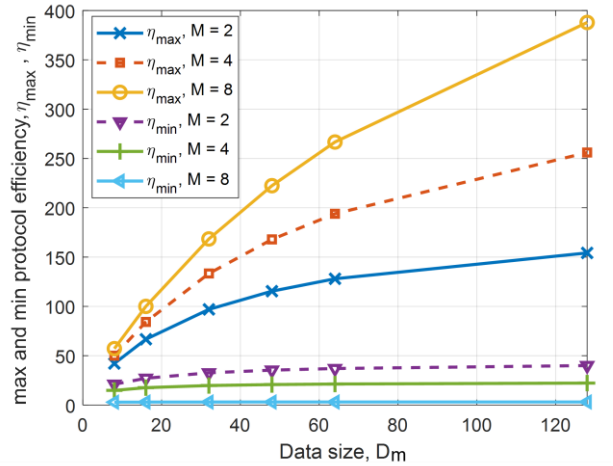


Figure 27: Effect of data size, D_m and M on protocol efficiency, η

Consequently, in the validation (Section 7.4) we choose $D_m = 32$ bits.

7.3 Algorithms and Illustrative Examples

Based on the frame design and analysis above, in this subsection we develop two algorithms to: (i) generate the ADPPM frame structure at the sender, and (ii) demodulate the frame at the receiver. We will also propose another algorithm to dynamically change the value of M to maintain certain packet error rate (PER).

Algorithm 2: A pseudo code summary of the steps for creating an ADPPM frame is shown in Algorithm 2. We will explain such an algorithm step by step using the example shown in Figure 28. The presentation follows higher level steps that those in Algorithm 2.

Step 1: The key parameters, namely, the size of input data, D_m , the guard pattern, G and the modulation

index, M , are to be determined. In the example, $D_m = 32$ bits and $M = 4$, i.e., $L = 2^M = 16$. We also assume that $G = '01110'$.

Step 2: The values of ezp and NOP are calculated according to Eq. (39) and (43), respectively. In the example $NOP = 4$ bits and $ezp = 7$ bits.

Step 3: Apply DPPM to modulate on input data.

 Input: Message data, D_m
 Output: ADPPM frame

1. *initialize: M, D_m, G*
2. *set $NOP = M/D_m$*
3. *set bit size for each extra zero position (ezp)*
4. *payload = mod_data = DPPM modulation of the input data*
5. *if (mod_data contains G)*
6. *add extra zero in the payload and update EZPs*
7. *end if*
8. *set ADPPM frame = $G + \text{payload} + G + NOP + EZPs + G$*

Algorithm 2. Steps for generating an ADPPM frame

Step 4: Check the data for matches to the guard pattern, G . Anytime the pattern of G is encountered in the payload an extra 0 will be added and EZPs field will be updated, as shown in the Figure 28.

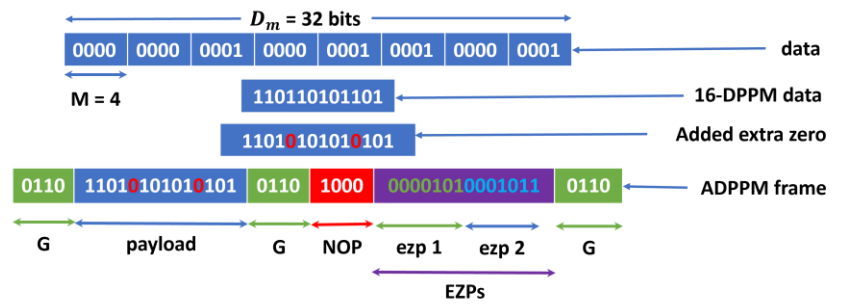


Figure 28: An example ADPPM frame

Step 5: Form a frame following the format shown in Figure 26.

Algorithm 3: The outlined steps explain how a receiver can decode an ADPPM frame and extract the message data, D_m . This algorithm is illustrated using the example shown in Figure 29. Again, the discussion follows higher level steps that those shown in Algorithm 3.

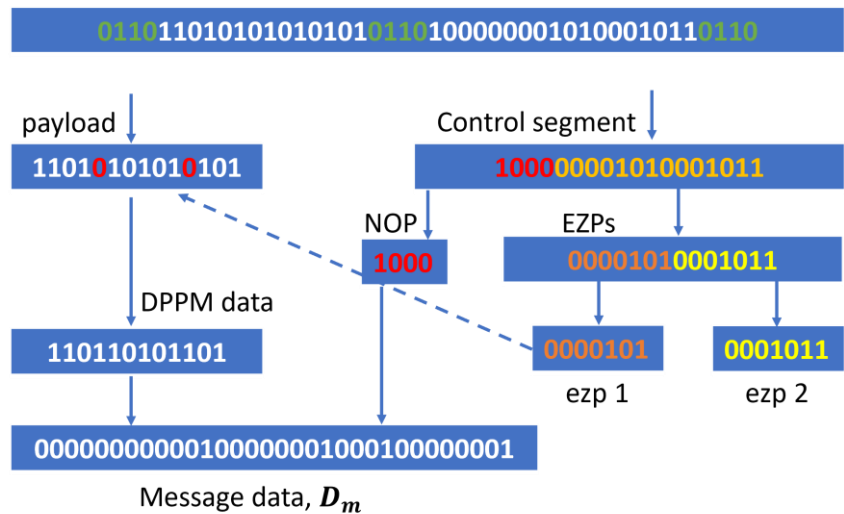


Figure 29: An example of decoding received ADPPM frame

Step 1: At first a receiver, Rx will look for the positions of the guard pattern, G throughout the whole frame.

Since according to the format in Figure 26, a transmitter, Tx, would have added G three times, Rx should receive at least three guard patterns. If there is any error Rx can receive less or more than three guard patterns. In case of the former, the frame should be resent by Tx. On the other hand, since Tx added extra 0's in the payload, Rx should not receive more than three guard patterns if there are no errors. However, theoretically it may happen, because the $EZPs$ field itself can contain a pattern that matches G . Thus, if Rx observes more than three instances of G , it does not conclude that an error has occurred.

Step 2: Rx will extract the payload and the control segment within the frame. The latter will further be divided into two parts, corresponding to NOP and $EZPs$.

Step 3: Depending on the decimal value of bits in the $EZPs$, extra 0's will be discarded from the payload. After discarding them, the payload will reflect DPPM modulated data.

Step 4: The number of 1's in the DPPM data should match the value of NOP . In the example $NOP = 8$. We can also see DPPM data contains 8 1's. If these two fields do not match there are errors in the packet. Given that the Rx knows that $D_m = 32$, the value of M can be concluded by dividing D_m by NOP .

```

-----
Input: Received ADPPM frame
Output: Message data, D
-----
1. Check the guard positions, G in the received data
2. if (no. of G < 3 or no G found in the beginning and end)
3.   ack = 0
4. else
5.   extract payload and control segment
6.   if (no. of bits in the control seg. < NOP)
7.     ack = 0
8.   else
9.     extracts NOP and EZPs
10.    if (mod(EZPs, ezp) ≠ 0)
11.      ack = 0
12.    else
13.      ack = 1
14.    if (EZPs ≠ 0 )
15.      get the decimal value of each ezp
16.      if (max(decimal value of each ezp) < no. of payloads)
17.        delete extra zeros from the payload
18.      end if
19.    end if
20.    if (no. of 1's in the payload = NOP)
21.      demodulate payload
22.    else
23.      ack = 0
24.    end if
25.  end if
26. end if
27. end if

```

Algorithm 3. A demodulation of an ADPPM frame

Step 5: Rx will then demodulate the DPPM data to get the actual message data, D_m . While decoding Rx will use the value of M inferred from the previous step.

Algorithm 4: Leveraging Algorithms 2 and 3, this algorithm calculates PER and dynamically changes value of M depending to such PER. In Algorithm 4, a value M is initially chosen and then depending on PER either we decrease or increase M . In the validation section, both Algorithms 2, 3 and 4 will be explained with simulated data.

Input: Data, M
Output: Packet error rate, PER

1. Initialize: M , D_m and $threshold_PER$
2. Call Algorithms 1 and 2
3. Calculate PER
4. **if** $PER > threshold_PER$
5. Increase M
6. **else**
7. Keep same M
8. Go to next frame
9. **end if**
10. calculate PER

Algorithm 4. Changing value of M to optimize the PER

7.4 Validation Results

We have implemented Algorithms 2, 3 and 4 in MATLAB. Through simulation, we have analyzed PER, bit rate for different value of SNR and underwater depth, d_w . In this simulation we change the value of M and visualize the effect of M on bit rate and PER.

Figures 30 and 31 capture the effect of M in bit rate and PER calculation for different SNR. These results have been generated using Algorithms 2 and 3. Figure 30 shows that if the value of M is increased the bit rate decreases. This is expected due to the fact that the modulated data size grows with the increase of M , which ultimately decreases the bit rate; recall that the symbol L exponentially grows with the increase in M . On the other hand, Figure 31 shows that PER decreases with the increase of M . Because higher values of M imply that we are sending less ‘on’ chips and we can

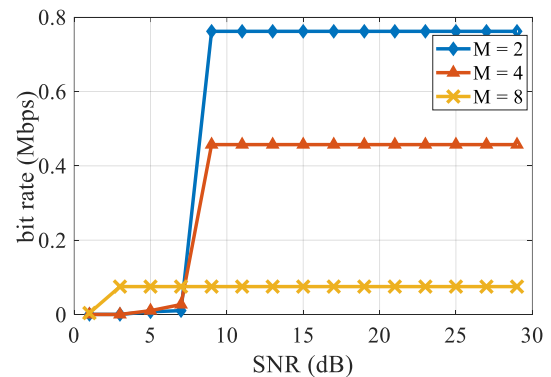


Figure 30: Bit rate vs SNR for different value of M

provide more power on those ‘on’ chips; consequently, the probability of bit errors diminishes. In Figure 31, PER becomes almost close to zero for SNR value above 15 dB. Hence, if the signal strength at the receiver is very good all values of M work perfectly. In this kind of situation settings, a lower value of M is desired, because it will give better bit rate. However, if the signal strength is low such that SNR is less than 15 dB, a higher value of M gives better PER at the expense of lower bit rate and consequently lower bandwidth efficiency as shown earlier in Figure 27. To conclude, depending on the signal strength at the receiver, we can dynamically change the value of M to achieve power and the bandwidth efficiency using Algorithm 4.

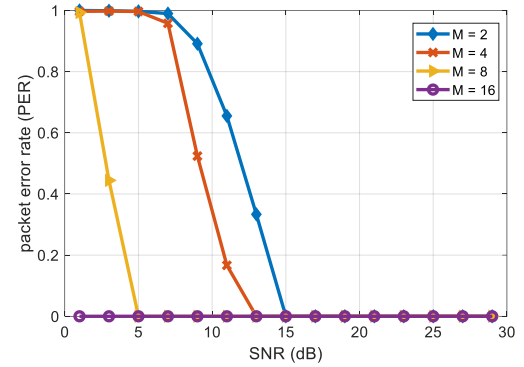


Figure 31: Packet error rate vs SNR for different M in DPPM

Figure 32 shows PER versus underwater depth for different values of M , using Algorithm 4. In this simulation we have also studied the performance of OOK modulation, because it is the most popular

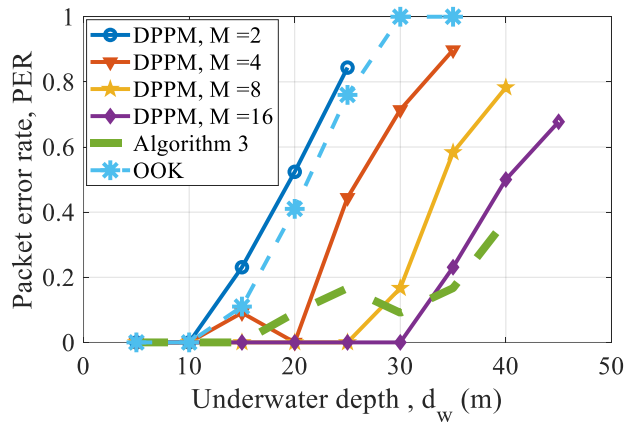


Figure 32: PER vs underwater depth for various modulation techniques

modulation techniques for underwater optical communication; thus, we use OOK as a baseline to compare the result of our proposed ADPPM modulation scheme. The results in Figure 32 indicate that PER grows with the increase of underwater depth d_w ; this is because the SNR diminishes with the increase of underwater depth due to signal absorption and scattering. PER

increases rapidly for small values of M . For OOK, PER also increases with the increase of d_w . For example, at depth 20 meter, the value of PER is almost zero for $M = 4, 8, 16$ and approximately 0.5 for $M = 2$. Hence, at

this point, setting $M = 4, 8,$ or 16 will yield the same error performance. However, keeping the value of M as low as possible will increase the bit rate as we discussed earlier. By using Algorithm 4 we can dynamically adjust M to optimize the bit rate and PER. For example, for a PER threshold of 0.3 , Algorithm 4 will adjust M if PER exceeds a threshold. The green line in Figure 32 shows the simulation result for Algorithm 4. The results plotted in the figure indicate that PER remains below 0.3 for $d_w = [5, 15]$, and consequently a setting of $M=2$ is the best option. With the increase of d_w , Algorithm 4 dynamically would boost M to meet the PER requirement. Figure 32 also shows that our proposed approach outperforms the traditional OOK modulation for increased underwater depth.

Chapter 8: Modulation: Improving Bandwidth Efficiency of DPPM

In the previous chapter, we have discussed how we can dynamically change the value of M of DPPM modulation to minimize the packet error rate (PER). In this chapter, we will discuss how we can improve the bandwidth efficiency of DPPM. As we mentioned earlier that the DPPM is one of the popular power-efficient schemes for supporting visible light communication in underwater environments and across the air-water interface. Despite such an advantage, DPPM does not efficiently utilize the available channel capacity. This paper aspires to tackle such shortcoming by striking a better balance between power and bandwidth efficiency. Particularly, L-DPPM is considered where a block of M input data bits is mapped into one of the L distinct waveforms containing only one ‘on’ chip. A novel encoding algorithm and frame structure are proposed in order to shorten the time between consecutive symbols and consequently improve the bit rate of L-DPPM. The idea is based on avoiding bit patterns that contribute the most to bandwidth inefficiency. The proposed algorithm explores several bit patterns remapping through simple complement and shifting operations. A detailed frame structure with all necessary control bits is provided. Overall, boosting the bandwidth efficacy comes at the expense of a slight increase in control bit count and transmission power. The simulation results demonstrate the effectiveness of the proposed encoding algorithm and provide guidelines for determining M for best performance.

8.1 Theoretical Analysis

The DPPM frame size depends on the input data size, D_m and modulation index, M , and the binary value of input data. When all the input data is logic ‘0’, the DPPM frame size becomes maximum and when all input data is logic ‘1’, the DPPM frame size becomes minimum. The maximum and minimum DPPM frame size are:

$$F_{max} = 2^M \cdot \left\lceil \frac{D_m}{M} \right\rceil \quad \text{and} \quad F_{min} = \left\lceil \frac{D_m}{M} \right\rceil \quad (52)$$

For any other combination of the input data, the DPPM frame size is between F_{max} and F_{min} . Hence the average the frame size is:

$$F_{avg} = \frac{D_m(2^M+1)}{2^M} \quad (53)$$

From Eq. (53) we can clearly see, the average frame size is bigger than actual data size, D_m and it grows rapidly with the increase of M . It is worth mentioning that among all the modulation technique OOK requires a smaller number of bits to modulate the actual data, and the modulated data size is exactly matches the data length, D_m . To capture the relation between actual and modulated data sizes, we define protocol efficiency, η as follows:

$$\eta = \frac{D_m}{F_{avg}} \times 100\% = \frac{2^M}{2^M+1} \times 100\% \quad (54)$$

The above equation indicates that the protocol efficiency for OOK is 100% and less than 100% for DPPM modulation for any value of M . Though the protocol efficiency of DPPM is less than OOK, it is very power efficient because it requires fewer number of ‘on’ chips than OOK. If D_m and M are fixed, then the DPPM frame always contains $\left\lceil \frac{D_m}{M} \right\rceil$ ‘on’ chips for any data bit pattern. For example, from Figure 4 we can see that the DPPM frame contains 3 ‘on’ chips. If the value of data is changed, then DPPM frame will again contain 3 ‘on’ chips but in different positions. On the other hand, in OOK, the number of ‘on’ chips depends on the decimal value of data. If the probabilities of having ‘on’ and ‘off’ chips (meaning having 1 or 0 for a bit) in the data are the same, then a message of size D_m contains an average of $\frac{D_m}{2}$ ‘on’ chips. Thus, we can define power efficiency of DPPM with respect to OOK as follows:

$$P_{dppm/ook} = \left(1 + \frac{\left\lceil \frac{D_m}{2} \right\rceil - \left\lceil \frac{D_m}{M} \right\rceil}{\left\lceil \frac{D_m}{2} \right\rceil} \right) \times 100\% = \left(1 + \frac{M-2}{M} \right) \times 100\% \quad (55)$$

For example, if $M = 4$, then, $P_{dppm/ook} = 150\%$, which means we can improve power efficiency by 50% compared to OOK. If M increases, the power efficiency grows; however, from Eq. (54) we know protocol efficiency diminishes for large M , meaning that the bandwidth efficiency decreases as well. In the next section we will discuss some methods by which we can improve the protocol efficiency.

8.2 Improving Bandwidth Efficiency

The DPPM frame size depends on the data length D . Technically from Figure 4, we can observe that the DPPM frame size depends on the decimal value of each group of M bits in the data pattern. Recall that in DPPM, a message is divided into $\frac{D_m}{M}$ groups. If we can map the message bit pattern to another where the sum of the decimal values of each group is less than that of the original message, then we can reduce the size of the DPPM frame, which eventually improves the bit rate and consequently the protocol efficiency. In order to do such mapping, it will be necessary to add some overhead, i.e., control bits, to the DPPM frame to enable successful message decoding at the receiver. The following discusses our proposed transformation for improving DPPM bit rate.

1's complement method: For certain messages, we can improve the bandwidth efficiency by simply sending the 1's complement version of input data instead of sending the original one. For example, if input data, $D_m = '11110111'$ and $M = 4$, after DPPM modulation it becomes '000000000000000100000001'. The 1's complement of D_m is '00001000' and after modulation it becomes '1000000001'. Thus, in this case, clearly sending the original data pattern requires more bits than sending its 1's complement. Since there could be another scenario where sending the original data pattern requires fewer bits, an additional control bit has to be included in the DPPM frame to indicate whether the original or 1's complement version has been used to encode the data.

Shifting method: By circular shifting of message bit patterns, we can also minimize the sum of decimal values of each group. For example, if $M = 4$ and $D_m = '0001100000000001'$ the decimal values of each 4 bits are (1, 8, 0, 1). Now if we right shift D_m three times circularly, D_m becomes $'0010001100000000'$ which provides a much smaller sum of decimal values (2, 3, 0, 0). To support shifting, we need control flags to specify the shift amount. Since a message of length D_m can be shifted (D_m-1) times, the overhead to represent the number of shift amount is,

$$O_s = \lceil \log_2 D_m \rceil \quad (56)$$

The above equation indicates that a larger value of D_m , i.e., longer message, would increase the overhead.

Reducing extra 0's from DPPM frame: We have already mentioned that a higher value of M increases the DPPM frame size, and that frame mostly contains long string of 0's. Our next method is to find a way to reduce extra 0's from that DPPM modulated data. The idea is to

indicate that only 50% of the zeros are indeed included in the symbol modulated bit pattern and the rest are omitted. For example, for "0000001" we include "0001" and provide a control bit to reflect that only 50% of the zeros are included. Generally, if the DPPM frame contains a count of n zeros before an 'on' chip, we can reduce that number by either $\frac{n}{2}$ or $(\frac{n-1}{2} + 1)$ based on whether n is even or odd. For instance, assume that '00000000010000010000101' is a DPPM modulated message, which contains (9, 5, 4, 1) 0's before every 1's. Now we can reduce those 0's to (5, 3, 2, 1) based on the above methods. A control bit will be set if zeros are omitted. In order to indicate whether the reduction comes from an odd or even number of 0's, we need to add

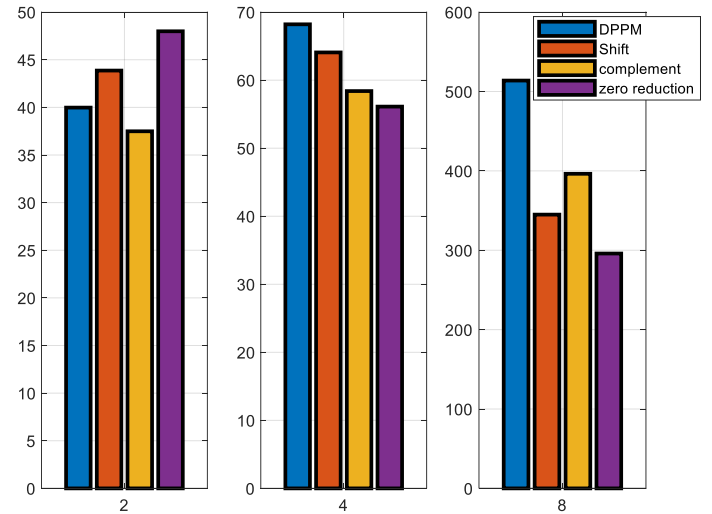


Figure 33: DPPM frame sizes for different methods ($D_m = 32$ bits)

an additional controls bit. For this example, for the four symbols we could add ‘1101’ where a one indicates that the actual number of 0’s was odd and a zero implies an even number of 0’s. The number of control bits in this case depends on how many groups in the message and can be determined by:

$$O_z = \left\lceil \frac{D_m}{M} \right\rceil \quad (57)$$

Figure 33 shows how much we can reduce the DPPM frame size by these three methods individually for a message size, $D_m = 32$ bits for different values of M . From this figure we can see, a small value of M like 2, actually increases rather than decreases the frame size. However, for higher values of M , any method can reduce the frame size than original DPPM frame. In the next section, we develop an algorithm that leverages these three methods to minimize the DPPM frame size.

1’s complement of individual groups: Applying the 1’s complement to the whole message doesn’t always reduce the DPPM frame size. For example, if message = ‘00001111’ and $M = 4$, the 1’s complement becomes ‘1111000’ which means DPPM data size will stay the same. Alternatively, we explore applying 1’s complement to the individual groups and adopt the version which has the lowest equivalent decimal values. In the above example the first 4 bits of data is ‘0000’, and thus will include it as is. The next 4 bits are ‘1111’, and applying 1’s complement is beneficial. Thus, our modified message will be ‘00000000’ and corresponding the DPPM frame will be ‘1101’, where two extra control bits are appended to indicate whether we have used the original or complement bit pattern of each group. Therefore, in this method, the added control bits, O_{cg} , equal to the number of groups.

$$O_{cg} = \left\lceil \frac{D_m}{M} \right\rceil \quad (58)$$

The frame design under this method is referred to as Complement DPPM frame (CDPPM).

8.3 *Frame Design*

EDPPM frame: As discussed in the previous section, our proposed three methods work well in different message data patterns. In this section, we will combine those methods to



Figure 34: EDPPM (a) and CDPPM (b) frame structures

create a frame structure which provides the minimum number of bits to represent a DPPM modulated data. We name our approach as Enhanced DPPM (EDPPM). If o_c, o_s, o_z represent the number of control bits required to represent complement, shifting, and reduction of 0's, then the total overhead in bits is:

$$O = O_c + O_s + O_z \quad (59)$$

Figure 34(a) shows the frame structure of EDPPM, where payload is the modulated data. Using Eq. (56) and (57), we can update Eq. (59) as follows:

$$O = 1 + \lceil \log_2 D_m \rceil + \left\lceil \frac{D_m}{M} \right\rceil \quad (60)$$

From Eq. (52) we know that the minimum original DPPM data size is $\frac{D_m}{M}$. For EDPPM we need to add the overhead, hence the minimum EDPPM frame size is:

$$F'_{min} = \left\lceil \frac{D_m}{M} \right\rceil + O = 1 + 2 \left\lceil \frac{D_m}{M} \right\rceil + \lceil \log_2 D_m \rceil \quad (61)$$

Finding the maximum frame size is tricky, since we are applying all three methods together. We need to find a pattern of the input data which modulated version doesn't get reduced by any of the above methods. For example, if $M = 4$ and $D_m = '00001111'$, we cannot reduce the DPPM data. If we apply one's complement, the sum of the decimal value of each group doesn't change. Moreover, if we apply any number of right shifts, the sum of the decimal value of each group remains the same. This example tells us that if half of the groups have '0000' pattern and another half have '1111' pattern for $M = 4$, complement and shifting do not help to reduce the DPPM data size. Thus, we can represent maximum frame is as follows:

$$F'_{max} = \frac{1}{2} \left\lceil \frac{D_m}{M} \right\rceil + 2^{M-1} \left\lceil \frac{D_m}{M} \right\rceil + O = 1 + \left\lceil \frac{D_m}{M} \right\rceil \left(\frac{3}{2} + 2^{M-2} \right) + \lceil \log_2 D_m \rceil \quad (62)$$

By knowing F'_{min} and F'_{max} , we can calculate the average frame size.

$$F'_{avg} = 1 + \left\lceil \frac{D_m}{M} \right\rceil (4 + 2^{M-3}) + \lceil \text{Log}_2 D_m \rceil \quad (63)$$

Using Eq. (54), we can again calculate the protocol efficiency of EDPPM as follows:

$$\eta' = \frac{D_m}{1 + \frac{M}{D_m}(4 + 2^{M-3}) + \lceil \text{Log}_2 D_m \rceil} \times 100\% \quad (64)$$

Now, we redefine power efficiency of our proposed frame structure in a similar way like Eq. (55). In the case of EDPPM, we need to keep in mind that the extra overhead also carries ‘on’ chips. If the probabilities of having an ‘on’ and ‘off’ chip are similar, the overhead will contain on average $\frac{O}{2}$ ‘on’ chips. Thus, the power efficiency of our proposed method relative to OOK will be

$$P_{idppm/ook} = \frac{\frac{D_m}{2} - \left(\left\lceil \frac{D_m}{M} \right\rceil + \frac{O}{2} \right)}{\frac{D_m}{2}} \times 100\% \quad (65)$$

Substituting the value of O from Eq. (59) into Eq. (65) we get,

$$P_{idppm/ook} = 1 - \frac{3}{M} - \frac{1}{D_m} (1 + \lceil \text{Log}_2 D_m \rceil) \quad (66)$$

This new protocol efficiency and power efficiency will be explained elaborately through simulation in the validation result section.

A pseudo code summary of the steps for creating an EDPPM frame is shown in Algorithm 5. We will explain such an algorithm using the example shown in Figure 35.

Step 1: The key parameters are to be determined, specifically, the input data, P , the data size, D_m , and the modulation index, M . In the example, $P = '1110011111111110'$, $D_m = 16$ bits and $M = 4$. Depending on the value of M and P , the size of O_s and O_z are determined using Eq. (56) and (57), which are 4 for both cases in this example.

Step 2: Apply 1's complement to P .

Steps 3-8: Perform circular right shift to both original and complement versions of P for D_m times. Each time we calculate the sum of decimal values of each

group. We then identify the lowest sum achieved for both original and complemented versions. In this example, we get the lowest sum after shifting 1 time for original input data and 3 times for the complement version and the lowest sums are 40 and 5 for original and 1's complement version respectively. We adopt the smallest value and adjust the bit pattern accordingly.

In the example, '0010001100000000' is picked. Thus, instead of sending the original bit pattern for P , this value will be considered for DPPM modulation. Since the 3rd right shift of the 1's complement version has been taken, control bit $O_c = 1$ and $O_s = 0011$.

Step 9: Since, $M = 4$, after DPPM modulation to '0010001100000000' yields '001000111'.

Input: Message data payload (P), D_m , M
Output: IDPPM frame

1. initialize: M , D_m , and size of O_c , O_s and O_z
2. get 1's complement of P , P'
3. for $i=1$ to $D_m = \text{size of } (P)$
4. circular right shift P & P'
5. calculate sum of decimal value of each group
6. end for
7. get minimum sum of decimal values of each group
8. update P , O_c and O_s
9. modulate P using DPPM
10. shortening the string of leading 0's from each group of DPPM frame to either $\frac{n}{2}$ or $(\frac{n-1}{2} + 1)$
11. update O_z
12. EDPPM frame = DPPM + O_c + O_s + O_z

Algorithm 5. Steps for generating an EDPPM frame

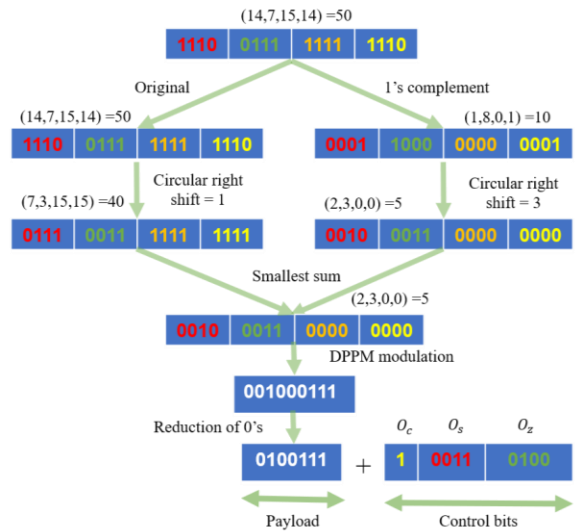


Figure 35: Illustration of creating EDPPM frame

Steps 10-11: Removing some of the leading 0's from the modulated data, as discussed earlier. In the example, '001000111' becomes '0100111' which is the data payload of the EDPPM frame. Accordingly, O_z is updated to be '0100'.

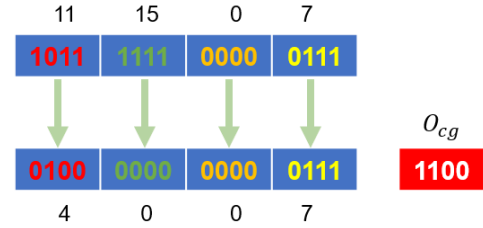


Figure 36: Illustration of creating CDPPM frame

Step 12: Creating the EDPPM frame by adding payload and overhead, which is '0100111100110100' in the example.

CDPPM frame: Creating a CDPPM frame is quite simple; Algorithm 6 describes the steps. In such a frame structure, we have only payload and one overhead field which has shown in Figure 36. The size of overhead O_{cg} can be calculated using Eq. (58). Figure 36 explains algorithm 6 with an example.

Steps 1-2: Again, the key parameters are P , D_m , and M . In the example, $P = '1011111100000111'$, $D_m = 16$ bits and $M = 4$. Depending on the value of M and P , size of O_{cg} is determined using Eq. (58), which are 4 in this example.

Steps 3-12: Find the 1's complement of each group of M data bits and compare the decimal value to that of the original bit pattern. If the complement version has a

Input: Message data payload (P), D_m , M
Output: CDPPM frame

1. initialize: M , D_m and size of O_{cg}
2. group, $G = \lfloor \frac{D}{M} \rfloor$
3. **for** $i = 1$ to G
4. calculate 1's complement of each group
5. **if** (1's complement of $G(i) < \text{original } G(i)$)
6. new $G(i) = 1$'s complement of $G(i)$
7. $O_{cg}(i) = 1$
8. **else**
9. new $G(i) = \text{original } G(i)$
10. $O_{cg}(i) = 0$
11. **end if**
12. **end for**
13. CDPPM frame = $G + O_{cg}$

Algorithm 6. Steps for generating the CDPPM frame

smaller decimal value, it will be adopted. For instance, in the example in Figure 36, the decimal value of the first 4 bits of data is 11 and its complemented value is 4; hence, the latter is to be used and the corresponding O_{cg} field will be 1.

Step 13: Combine the new bit pattern for the data with O_{cg} to create the CDPPM frame. In this case it is ‘01000000000001111100’.

8.4 Validation Results

Algorithms 5 and 6 have been implemented using MATLAB to analyze the protocol and power efficiency of our proposed EDPPM and CDPPM frame structures. Figure 37 captures the effect of M on protocol efficiency for different data sizes of EDPPM frame. We also show protocol efficiency for original DPPM data. From Eq. (54), it is clear that protocol efficiency doesn't change with the data size, D_m , which is obvious in this figure.

For $M = 2$, the protocol efficiency actually is worse than the original DPPM, which makes sense because in this case the overhead is relatively very high relative to the reduction of bit count achieved by our method.

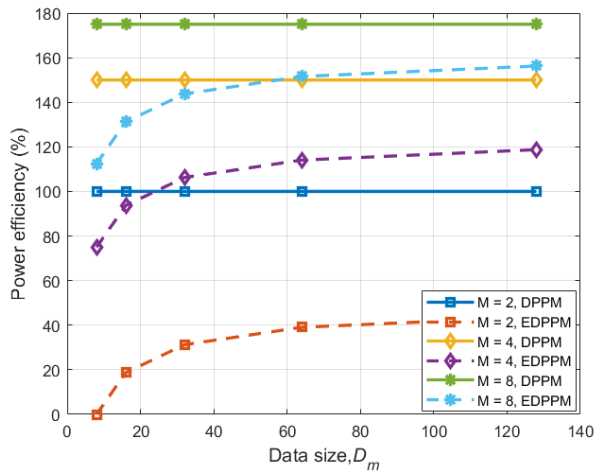


Figure 37: Power efficiency of EDPPM frame relative to OOK frame for different data size

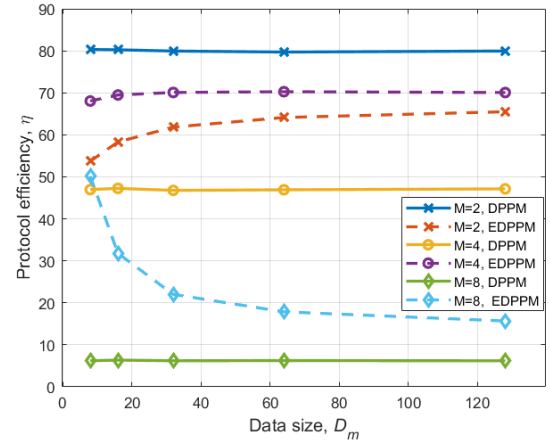


Figure 38: Protocol efficiency of EDPPM frame for different data size

However, for higher values of M , we can see protocol efficiency increasing significantly and surpassing DPPM. For instance, we can increase protocol efficiency by 45% for $M = 4$. One of the key problems of DPPM is that its protocol efficiency decreases a lot with the increase of M . Here, we can see, when $M = 8$, the protocol efficiency drops to around 5%. Yet, using our method we can improve it a lot, especially for smaller data sizes.

The improved protocol efficiency comes in exchange for a slight reduction in the power efficiency, as shown in Figure 38, which has been plotted using Eq. (55) and Eq. (66). From this figure we can observe that for a low value of M , the reduction of power efficiency becomes major. For example, if $D_m = 64$, $M = 2$, the power efficiency using our method is 40%, down from 100% for the original DPPM. Yet if $D_m = 64$, $M = 8$, the power efficiency drops from 175% to 150% using our method, which is relatively small in this case. From the above discussion, we can conclude that for lower M values, EDPPM doesn't improve the protocol efficiency, yet for higher values of M it increases protocol efficiency significantly.

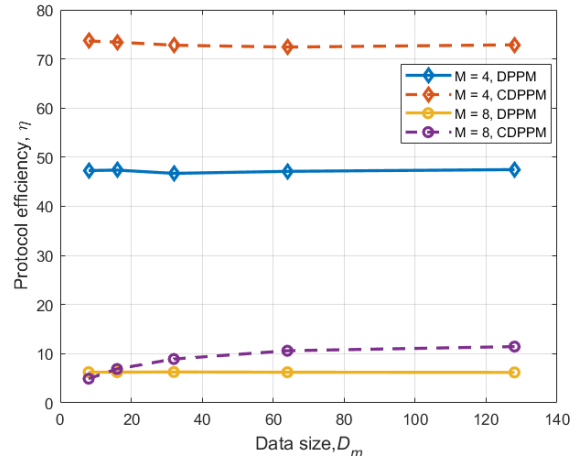


Figure 39: Protocol efficiency of CDPPM frame for different data size

We can improve protocol efficiency more while having the least effect on the power efficiency using a CDPPM frame. The results are shown in Figure 39 and 40. From Figure 39, we can see protocol efficiency increasing from 48% to 74% for $M = 4$. Nonetheless, for higher M values of like $M = 8$, the increment is little. Thus, the CDPPM frame structure is good for relatively lower values of M . From Figure 40, we can also see the reduction in power efficiency is less than the EDPPM frame (Figure 35) for $M = 4$.

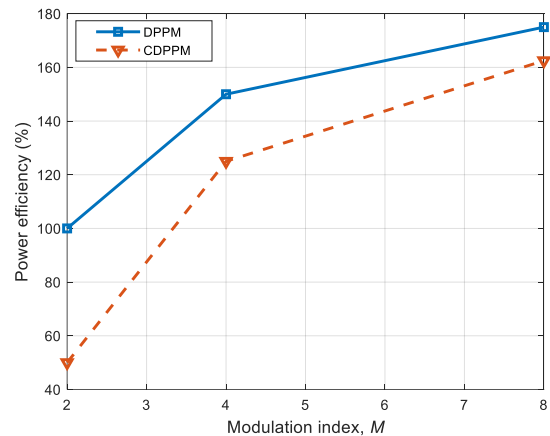


Figure 40: Power efficiency of CDPPM frame relative to OOK frame for different data size

Chapter 9: Photoacoustic: Optimizing Acoustic Signal Quality

So far, we have exploited how VLC can be used to communicate through the air-water interface. We have developed different methods and algorithms to improve all the key parameters of VLC like SNR, bit rate, bandwidth efficiency and best suited modulation techniques for VLC. Though VLC is very good for short distance communication, exponential decay of light in underwater setup makes it hard to work for long distance communication. To our best knowledge, there is no single physical signal that supports long distance communication while crossing the air-water boundary. In underwater wireless networks, photoacoustic energy conversion using high energy laser pulse is the only known viable option for communication from an airborne unit to a node at large depth, e.g., a submarine or an unmanned underwater vehicle. However, controlling the generated acoustic signal through this process is very complex. Specifically, if the repetition rate of laser pulses is low, the corresponding acoustic signal is very broadband. The higher frequency components of this broadband signal attenuate more if the underwater node is very far from the surface. Hence, a relatively narrowband signal with lower frequency components is desirable for long distance communication. The frequency component of the broadband acoustic signal depends on the incident angle of the laser light and observation angle of the receiver, i.e., the position of the underwater hydrophone. Both angles also change continuously for a wavy water surface, which makes it more complex to determine the frequency components of this kind of signal. In this chapter, we show that by carefully choosing the relative position of the airborne unit and underwater node, we can generate a narrowband acoustic signal with lower frequency components for both flat and wavy water surfaces. We provide theoretical analysis and simulation results to capture the effect of these angles on the generated acoustic signals. We further provide guidelines for optimum angle setting for improving the quality of the optoacoustic communication link.

We have already mentioned that the generated acoustic signal from an optoacoustic energy transfer mechanism is generally a broadband signal. Therefore, it is important to have the pressure spectral response analysis. In this section, we will discuss the spectral response of the acoustic pressure; based on such analysis, we will determine the best relative position of an airborne unit and underwater node for better quality acoustic signal generation. In the next section, we will show how this analysis helps in determining the relative positioning of the airborne unit and underwater node for the wavy water surface using a surface wave modeling function.

Table 3. A summary of the important notations

<i>Notation</i>	Description
r	Range to the observation point
θ_i	Incident angle
θ_r	Refracted angle
θ	Observation angle from vertical axis
φ	Observation angle from horizontal axis
t_r	Optical transmissivity of the water
β	Thermal expansion coefficient
C_p	Specific heat of the water medium
μ	Optical absorption coefficient
a	Laser beam radius
I_0	Laser intensity amplitude
τ	Laser pulse duration
T	Laser pulse repetition period
$I(t)$	Temporal laser waveform
$I(\omega)$	Impulse response of laser waveform
k	Acoustic wave number
ω	Angular frequency of acoustic wave
c	Speed of acoustic wave

9.1 Acoustic Spectral Response

The pressure spectral response of the generated acoustic signal by optoacoustic energy conversion methods depends on the laser parameters, medium parameters and the range of the underwater node, i.e., position of the hydrophone in the underwater. This pressure spectral response has been calculated by solving Green's function integral for normal [45] and oblique incident [43]. Eq. (67) and Eq. (68) show the result for a normal [45] and an oblique laser beam incident [43].

$$P_{normal}(r, \omega) = \frac{-TI_0\beta a^2}{2C_p} \cdot \frac{e^{ikr}}{r} \cdot I(\omega) \cdot \frac{\omega^2\tau\mu}{1+\omega^2\tau\mu^2} \cdot e^{\frac{-\omega^2\tau_a^2}{4}} \quad (67)$$

$$P_{oblique}(r, \omega) = \frac{-t_r K}{\mu} \cdot e^{ikr} \cdot I(\omega) \cdot \frac{\Lambda}{\mu} \cdot \frac{e^{\mathcal{F}}}{\Delta} \quad (68)$$

where,

$$K = \frac{i\mu\beta\rho_0\omega}{4\pi C_p r}, \quad (69)$$

$$\frac{\Delta}{\mu} = 2i\sigma \sin \theta_r \sin \theta \cos \varphi \sinh(\xi) - 2 \sinh(\xi) - 2i\sigma \cos \theta \cos \theta_r \cosh(\xi), \quad (70)$$

$$\xi = \frac{k^2 a^2 \sin 2\theta \cos \varphi \sin 2\theta_r}{8}, \quad (71)$$

$$\Delta = 1 - 2i\sigma \sin \theta_r \sin \theta \cos \varphi + \sigma^2 (\cos^2 \theta \cos^2 \theta_r - \sin^2 \theta_r \sin^2 \theta \cos^2 \varphi), \quad (72)$$

$$\sigma = \frac{k}{\mu} = \frac{\omega}{\mu c}, \quad (73)$$

$$\mathcal{F} = \frac{-k^2 a^2 (\sin^2 \theta \sin^2 \varphi + \cos^2 \theta_r \sin^2 \theta \cos^2 \varphi + \sin^2 \theta_r \cos^2 \theta)}{4} \quad (74)$$

$$\tau_\mu = \frac{\cos \theta}{\mu c} \quad (75)$$

$$\tau_a = \frac{a \sin \theta}{c} \quad (76)$$

All the parameters in Eq. (67) to (76) are described in Table 3, and the angles are marked in Figure 41. Now in Eq. (67), the term $(\omega^2 \tau_\mu)/(1 + \omega^2 \tau_\mu^2)$ acts like a high pass filter in frequency domain which has a 3-dB cut-off frequency:

$$f_H = \frac{1}{2\pi \tau_\mu} = \frac{\mu c}{2\pi \cos \theta} \quad (77)$$

From Eq. (77), we can observe that the cut-off frequency depends on the optical absorption co-efficient and observation angle, θ . The term $\exp(-\omega^2 \tau_a^2/4)$ in Eq. (67) represents the low pass filter with a 3-dB cut-off frequency:

$$f_L = \frac{c\sqrt{-\ln 0.7071}}{\pi a \sin \theta} \quad (78)$$

These two filtering function acts as a band pass filter. The interesting factor here is that the value of these two cut-off frequencies depends on the observation angle, θ . So, by controlling the value of θ , i.e., controlling the position of the laser transmitter and acoustic receiver we can create an acoustic signal with desirable frequency response.

In Eq. (67) and Eq. (68), $I(\omega)$ is the spectral response of the laser pulse waveform. Let $I(t)$ be the normalized laser beam profile; it can be represented as follows:

$$I(t) = \sum_{n=0}^{N-1} e^{-\left(\frac{t-nT}{\tau}\right)^2} \quad (79)$$

By applying a Fourier transform on Eq. (79), we get $I(\omega)$, which will be:

$$I(\omega) = \tau\sqrt{\pi}e^{-\frac{\omega^2\tau^2}{4}}e^{i(N-1)\omega T}\frac{\sin\frac{N\omega T}{2}}{\sin\frac{\omega T}{2}} \quad (80)$$

where, N is the number of Gaussian laser pulses, T is the laser pulse repetition period and τ is the laser pulse duration. If we know the value of all the parameters listed in Table 1, we can calculate Eq. (69) - (80) and then substitute all values in Eq. (68). Hence, we can calculate the spectral response of the generated acoustic wave for an oblique incident.

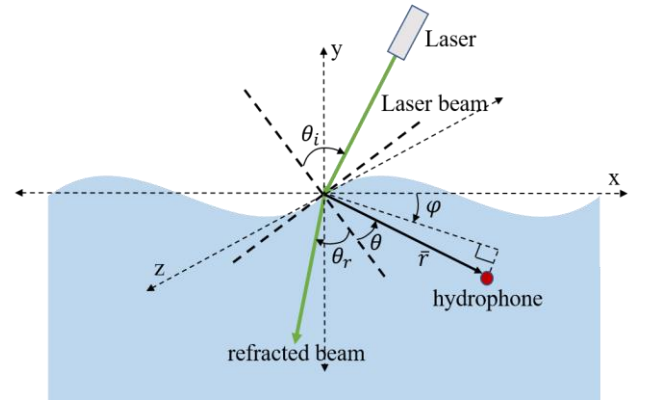


Figure 41: General geometry for linear optoacoustic communication from air to underwater

Through careful consideration of Eq. (68), we can note that there are three types of parameters: laser beam parameters, environmental parameters and some observation angles based on the relative position of the laser source, hydrophone, and water surface. For a specific laser beam source, the laser beam parameters and environmental parameters are fixed. Therefore, we can divide Eq. (68) into two parts as follows:

$$A_0(\mu, p_0, \omega, r, \tau, T) = \frac{-L_r K}{\mu} \cdot e^{ikr} \cdot I(\omega) \quad (81)$$

$$D(\theta_r, \theta, \varphi, \omega, \mu, a) = \frac{\Lambda}{\mu} \cdot \frac{e^{\mathcal{F}}}{\Delta} \quad (82)$$

where, A_0 is the amplitude term whose value depends on the optical absorption coefficient, laser beam peak power, communication distance, laser pulse duration and laser pulse repetition rate. Here, D is the directionality factor, which mainly depends on the refracted angle, θ_r , the vertical observation angle, θ , and the angular

frequency, ω , of the acoustic wave. The refracted angle, θ_r can be calculated from the laser beam incident angle, θ_i by using Snell's law.

$$\theta_r = \sin^{-1}\left(\frac{n_a}{n_w} \sin \theta_i\right) \quad (83)$$

where, n_a and n_w are the refractive index of air and water respectively. Substituting the value of A_0 and D in Eq. (68) we get,

$$P(r, \omega) = A_0 \times D \quad (84)$$

In the next subsection we will briefly describe amplitude, A_0 and directionality factor, D .

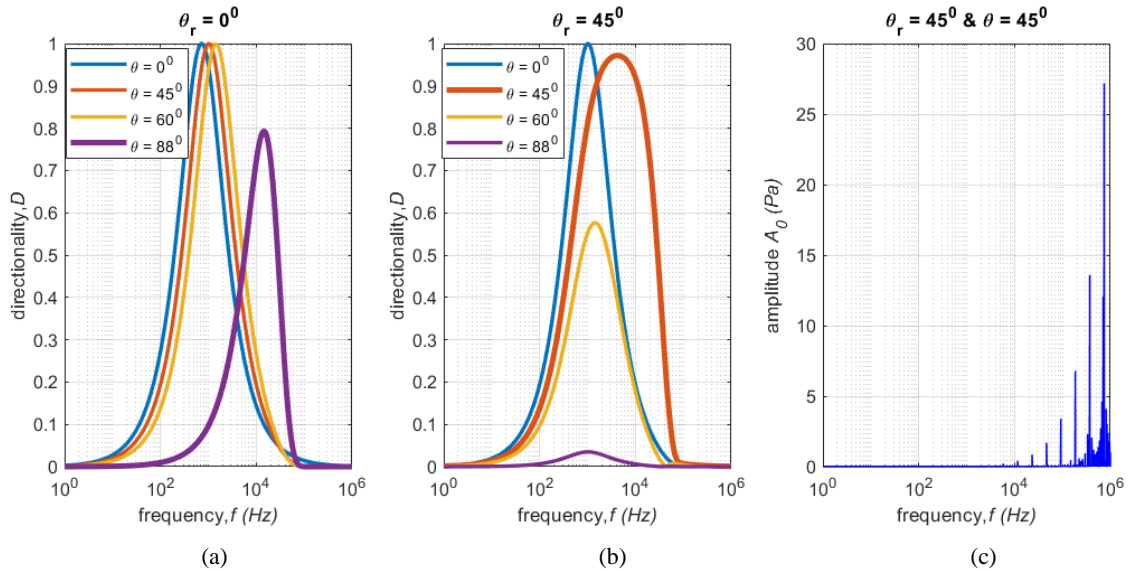


Figure 42: Determination of directionality factor, D for a) $\theta_r = 0^\circ$, b) $\theta_r = 45^\circ$ and amplitude, A_0 c) $\theta_r = 45^\circ$ and $\theta = 45^\circ$ for various frequency component of pressure wave

9.2 Parameter Effect Analysis

Amplitude factor, A_0 : From Eq. (69) and Eq. (81) we can see that the amplitude factor grows with the increase of the power and optical absorption coefficient of the laser beam; yet it decreases with the increase in observation distance. The value of this amplitude factor is plotted in Figure 42(b) with respect to frequency for laser parameters, $p_0 = 2 \text{ MW}$, $\mu = 13.7 \text{ m}^{-1}$, $\tau = 10 \text{ ns}$ and $T = 10 \text{ ms}$. From this figure we can conclude that the value of A_0 grows with the increase of frequency.

Directionality, D : As we already discussed, the directionality, D mainly depends on the relative position of laser light source and underwater observation point, i.e., refracted angle, θ_r , and vertical observation angle, θ . Eq. (84) shows that the acoustic pressure value is the multiplication of D and A_0 . Hence, in order to maximize the pressure value, we need to maximize both D and A_0 . Figure 42 shows the simulation results of D for various frequency components of the pressure wave using the same laser parameters that are used to calculate A_0 . This simulation is generated using Eq. (70) - (74) and Eq. (82). Figure 42(a) plots D with respect to f for various settings of θ while $\theta_r = 0^\circ$. The figure indicates that increasing f boosts the value of D until a certain level after which D starts to decline. Basically, the directionality factor, D acts like a band pass filter, whose lower and upper cut-off frequencies depend on θ . In addition, Figure 42(a) shows that the gap between the lower and upper cut-off frequency widens with the increase of θ . For example, when $\theta = 0^\circ$, the frequency response spans from few Hz to approximately 10 kHz. On the other hand, when $\theta = 88^\circ$, the frequency response covers from few Hz to approximately 100 kHz. From Figure 42(c), we observe that the value of A_0 is almost zero up to 10 kHz. So, in this setup if we choose $\theta = 88^\circ$, we can maximize the product of D and A_0 , and hence we can maximize the value of p . Keep in mind that Figure 42(a) has been drawn for $\theta_r = 0^\circ$. We have increased θ_r , specifically, $\theta_r = 45^\circ$, and recalculated D ; the results are plotted in Figure 42(b). The figure shows the maximum frequency span when $\theta = 45^\circ$. Based on Figures 42(a) and 3(b), we realize that, in order to maximize the value of p , we need to choose θ and θ_r in such a way that the sum of these two angles is close to 90° . If γ is the sum of these two angles then,

$$\gamma_{D_{max}} \approx \theta + \theta_r \quad (85)$$

We can further validate Eq. (85) from Figure 43, which shows the value of D for various θ while keeping θ_r fixed. In Figure 43(a), $\theta_r = 0^\circ$, and hence we get maximum D when θ is close to 90° . On the other hand, in Figure 43(b), D is maximum when $\theta = 30^\circ$ and $\theta_r = 60^\circ$. Based on this finding, in the next section we will discuss how to exploit the relationship between the position of the laser source and the underwater observation point for improving the quality of acoustic signal for both flat and wavy water surfaces.

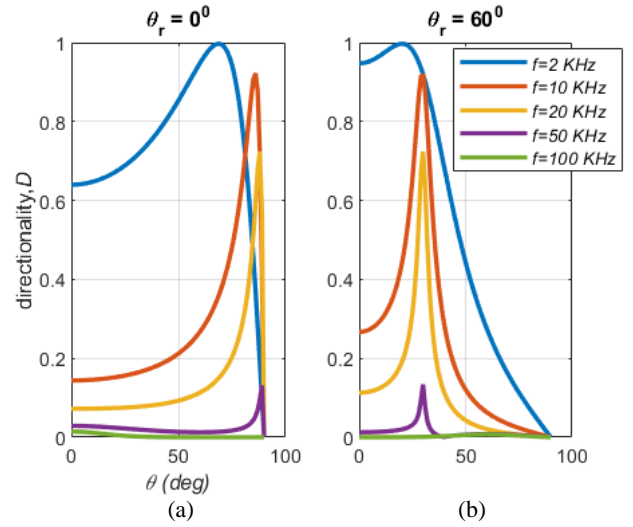


Figure 43: Directionality, D versus vertical observation angle, θ for (a) $\theta_r = 0^\circ$ and (b) $\theta_r = 60^\circ$

9.3 Positioning of Airborne and Underwater Nodes

The theoretical analysis in the previous section has highlighted the importance of selecting θ and θ_r and how keeping the sum of their values around 90° improves the quality of the generated acoustic signal. Based on such analysis, if we know the underwater node position, i.e., hydrophone position, we can shoot the laser beam in such a way that it creates the desired value of θ_r . Now based on the value of such θ_r , we can calculate the incident angle, θ_i using Eq. (83). In this section, we discuss optimum positioning of the laser source and underwater node for both flat and wavy water surfaces.

9.3.1 Flat Water Surface

For a flat-water surface, it is easy to calculate all the angle values; these angles do not change over time since the water surface is flat. Figure 44 shows some good relative positions of the laser source and the underwater

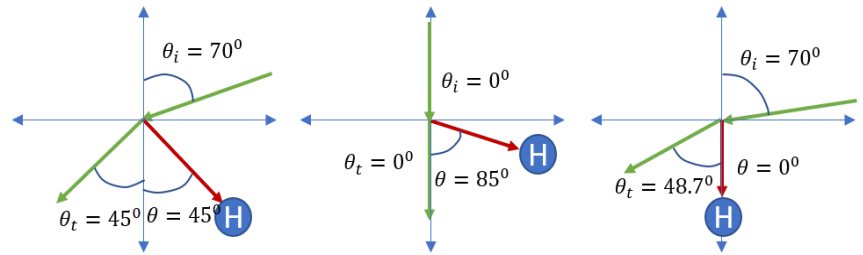


Figure 44: Relative position of laser beam incident point and hydrophone position for better quality pressure wave

node. For example, if the underwater node position is such that it creates 45° angle with the laser beam incident point at the water surface, we need to shoot the laser beam at such an incident angle so that the refracted angle becomes close to 45° as well. This scenario is explained in Figure 44(a). Figure 44(b) shows the best shooting angle of the laser beam for an underwater node close to the water surface. Similarly Figure 44(c) shows the best angle values for underwater nodes, which is vertically below the laser beam incident point at the water surface.

9.3.2 Wavy Water Surface

For a wavy water surface all angles continuously change over time due to waves on the water surface. In order to calculate these angles, we need to know the water surface function. It is very difficult to accurately model the water surface function. The simplest way to model the water surface is to assume that it is trigonometric function, e.g., sine or cosine, with variable amplitude and frequencies. However, more complex and accurate surface models exist in the literature. Section 3.1.2 has described some of the models. We utilize those models to simulate the water surface model in the simulation section.

Now, using any of the water surface models described in section 3.1.2, we can calculate the value of θ , θ_i , and θ_r at a particular phase or time of the water surface function. Again, we want to shoot the laser beam at such an angle so that the generated acoustic signal's strength is maximal for a known position of an underwater node.

To find such an angle, we will start with an optimal position of the laser source and underwater node for a flat-water surface and will observe the effect of water waves on the relative positions of the communicating pair. Figure 45(a) shows the optimal value of these angles for the particular hydrophone positions. If the water surface is wavy, these angles will be changing continuously over time. Figure 45(b) shows the angle values at a particular phase (moment of time) of the water surface. At this particular moment, we can observe that the value of θ_i , and θ_r becomes larger in

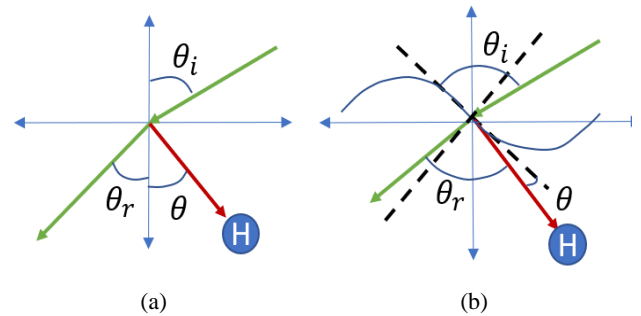


Figure 46: Relative position of laser beam incident point and hydrophone for (a) flat and (b) wavy water surface

comparison to the flat surface scenario. However, the value of θ becomes smaller than the flat surface. In essence, the sum of θ and θ_r remains almost the same, which is close to around 90° . This is a very important finding and is consistent with Eq. (85). The interesting question is whether this holds for a full wave period, i.e., at any particular moment of the water surface. In order to answer such a question, we need to calculate the values of θ and θ_r for all phases of a water surface period. The results are shown in Figure 46. This figure plots the sum of θ and θ_r for all phases of a water surface for different wave amplitudes. Based on these results, we can note that when the wave amplitude is zero, i.e., the water surface is flat, the sum of these angles is 90°

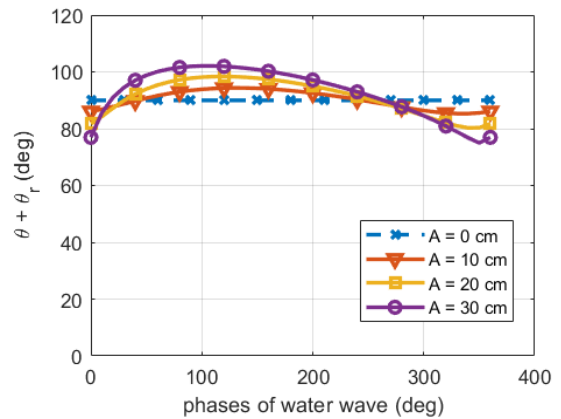


Figure 45: Sum of θ and θ_r for all phases of a water surface wave. Here water surface is assumed to be a sine wave

which is as expected from the above analysis. With the variation of water surface amplitude, the fluctuation of $\theta + \theta_r$ stays around 90° . If the water wave amplitude increases the deviation from 90° also grows, which has been shown in Figure 46 for four different wave amplitudes. Typically, water waves are not high in most setups under normal environmental conditions. Some rough wave crests could exist at shores and during environmental hazards like Tsunami, cyclone, etc. Therefore, we can conclude that the optimum relative positions of the laser source and underwater node for flat surface are still applicable for a wavy water surface in most practical scenarios. We confirm such a conclusion in the next section.

9.4 Validation Results

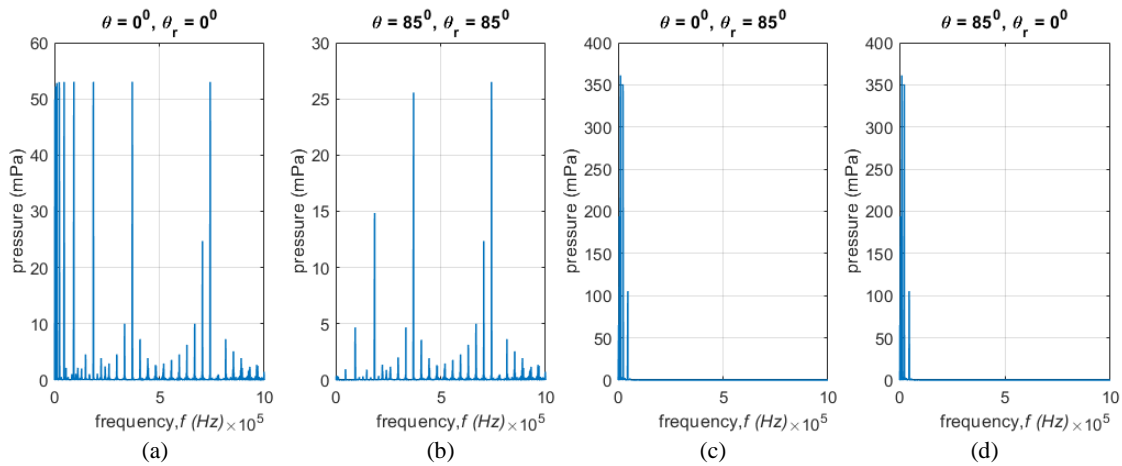


Figure 47: Spectral response of acoustic wave, for (a) $\theta_r = 0^\circ, \theta = 0^\circ$, (b) $\theta_r = 85^\circ, \theta = 85^\circ$, (c) $\theta_r = 85^\circ, \theta = 0^\circ$, and (d) $\theta_r = 0^\circ, \theta = 85^\circ$

From the previous section, we know that in order to create a relatively strong narrowband signal, we need to choose θ and θ_r such that their sum remains close to 90° . In this section, we simulate the spectral response of the generated acoustic signal using Eq. (68) – (80) for both flat and wavy water surfaces. The simulation results for flat water surface are shown in Figure 47 for various values of θ and θ_r while keeping other laser and environmental parameters fixed. The laser parameters have been chosen based on a currently available laser source [65]. Basically, we have set, $\mu = 13.7 \text{ m}^{-1}$, $\beta = 210 \times 10^{-6} \text{ (}^\circ\text{C)}$, $p_0 = 2 \times 10^6 \text{ MW/m}^2$, $a =$

3 mm, $C_p = 4200 \text{ J/Kg.k}$, $r = 1 \text{ m}$, $\tau = 10 \text{ ns}$, $T = 10 \text{ ms}$ and $c = 332 \text{ m/s}$. Figures 47(a) and 47(b) show that when the sum of θ and θ_r is not 90° , the spectral response is very broadband, spanning from few Hz to 1 MHz, and the pressure spectral amplitude is very low with a maximum around 50 mPa. On the other hand, Figures 47(c) and 47(d) indicate that the pressure spectrum spans from few Hz to approximately 100 KHz and the maximum spectral amplitude is around 350 mPa. Hence, in these cases, the frequency spectrum is almost 10 times lower than the Figures 47(a) and 47(b). Moreover, the maximum spectral amplitude is also higher than that in Figure 47(a) and 47(b). In essence, we are getting a relatively narrow-band signal with high spectral amplitude response when θ and θ_r are chosen such that their sum is 90° .

In the previous section, we have concluded that the criterion of choosing θ and θ_r for a wavy water surface is similar to that of the flat-water surface for typical water wave fluctuations. To confirm such a conclusion, we show in Figure 48 the simulation results for the spectral response of the generated acoustic signal corresponding to a wavy water surface. This simulation has been conducted for various phases of the wavy water surface function while fixing the amplitude of the

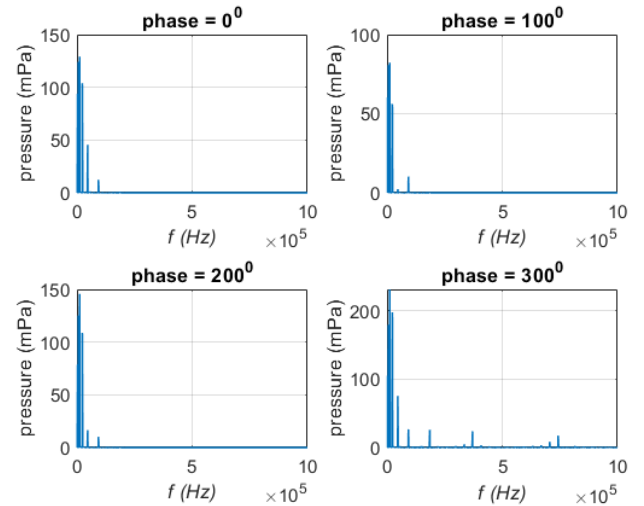


Figure 48: Spectral response of acoustic signal for various phase of the wavy water surface while wave amplitude = 30 cm

water wave at 30 cm. The results in this figure are almost like those in Figures 47(c) and 47(d) for various phases of the wavy water surface. Yet, the amplitude of spectral response becomes a bit weaker than the flat-water surface which is expected because the sum of θ and θ_r is not anymore 90° due to the fluctuation in the wavy water surface, as shown in Figure 46. If the water surface amplitude increases, the deviation of the sum of θ and θ_r from 90° will also increase; hence the amplitude of spectral response will decrease where Figure 47 shows that if the sum of θ and θ_r is not 90° , the spectral amplitude decreases.

Chapter 10: Photoacoustic: Modulation Scheme

As we discuss earlier, photoacoustic energy transfer is a promising mechanism for enabling cross-medium communication. Most research studies related to photoacoustic communication have only focused on characterizing the channel and relating the laser and acoustic signals. Little attention has been given to developing suitable modulation and demodulation schemes. In this chapter, we will discuss our research that fills such a technical gap and proposes a novel OOK modulation scheme using peak detection technique. In chapter 3, we have discussed the photoacoustic mechanism and the design challenges associated with the choosing appropriate modulation scheme for photoacoustic based air-water communication. Based on that discussion, in this chapter, we present our novel modulation and demodulation scheme. We will start our discussion describing the transmitter and receiver design based on that OOK modulation.

10.1 *Transmitter and Receiver Design*

To design a suitable modulation scheme, we have studied the generated acoustic signal carefully. Figure 6a shows the pattern of the generated acoustic signal for a single pulse of the laser light. From this figure we can observe that for a single laser pulse generated acoustic signal has multiple peaks. The highest peak appears almost at the very beginning. Then the strength of the acoustic signal diminishes within a couple of milliseconds. Hence, we adopted a peak detection based OOK modulation (PDOOK) scheme, meaning that sending a bit value of '1' corresponds to emitting a laser pulse and for a value of '0' no pulse is triggered. Figure 49 shows the PDOOK modulated acoustic signal for a random data pattern '1011'. In order to demodulate this acoustic signal, a peak detector is to be employed to identify the first peak of the received acoustic signal and use such peak value as baseline for the rest of the bit transmission time, T . If the first peak continues to be the largest, a bit value of "1" is concluded. However, the peak will be reset before the next bit

transmission time. In order to do that we use an electric reset pulse to reset that peak level. Here we must keep in mind that bit transmission time, T , and laser pulse duration, τ are different, whereas τ is the duration of laser pulse whereas T is the laser pulse repetition time. In the balance of this section, we describe the design of the transmitter and receiver for our PDOOK modulation/demodulation.

10.1.1 Transmitter Design

Figure 49 shows the timing diagram for the signals required to implement our proposed PDOOK. Based on such a timing diagram, Figure 50 shows a complete block diagram of the PDOOK transmitter and receiver. The main objective of the PDOOK transmitter is to produce a laser pulse of specific energy and repetition rate based on the data to be sent and the achievable bit rate. The controller generates a random return to zero (RZ) type data sequence that drives the

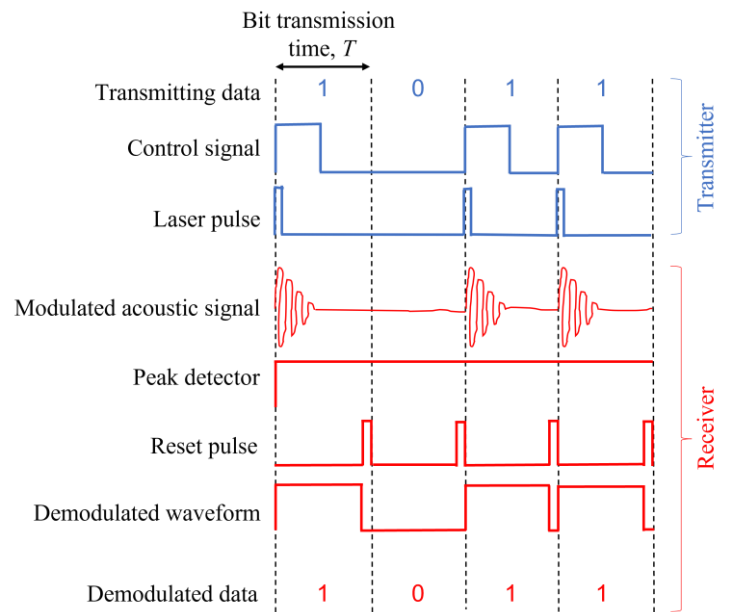


Figure 49: Timing diagram of PDOOK signals

components which triggers the pulse generation in the laser. First, based on the input data, the controller creates a signal to produce the desired laser pulse. We choose a RZ type control signal since it helps to distinguish between consecutive '1's. The laser driver has three main components: oscillator, preamplifier, and amplifier. Based on the electronic signals, these three components enable producing laser pulses with a desired pulse duration, pulse repetition rate and laser pulse energy. In order to implement a nonlinear PA mechanism, a very powerful pulsed laser source is required. Usually a Q switch Nd:Yag laser can produce such a high energy nano or pico-second laser pulses.

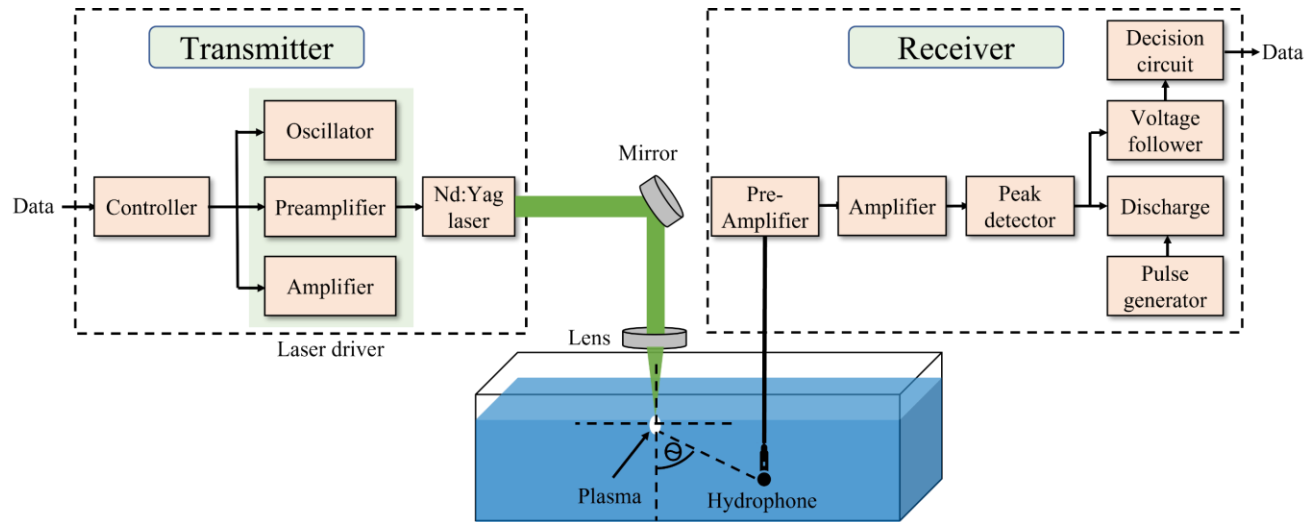


Figure 50: Block diagram of the photoacoustic air-to-underwater communication

10.1.2 Receiver Design

Figure 49 shows timing diagram for all the associated signals with a PDOOK receiver and Figure 50 provides a block diagram description of the receiver circuit. Functionally, we can divide the PDOOK receiver into the following:

Detection and amplification: At first, a hydrophone detects the PDOOK modulated acoustic signal. Since the modulated acoustic signal is very broadband, a hydrophone with a broad range of frequency response is required for this kind of receiver. Usually, an acoustic signal generated using a nonlinear PA mechanism can contain frequency components even in the MHz range. Though a higher frequency component mostly attenuates with the increase of the distance that the signal travels in the water, a hydrophone should sense at least a couple of hundreds KHz frequency components of the acoustic signal in order to successfully detect the signal at the receiver end. A pre-amplifier followed by an amplifier is used to produce a larger electrical signal.

Peak detector: After amplifying the signal, a peak detector is used to detect the maximum voltage of the acoustic signal. At the circuit level, a peak detector is realized using a capacitor. As shown in Figure 49, the detected signal peak should be latched for at least T sec, which can be achieved by choosing appropriate RC time constant. In order to successfully detect the next acoustic pulse (next transmitted bit), we need to reset

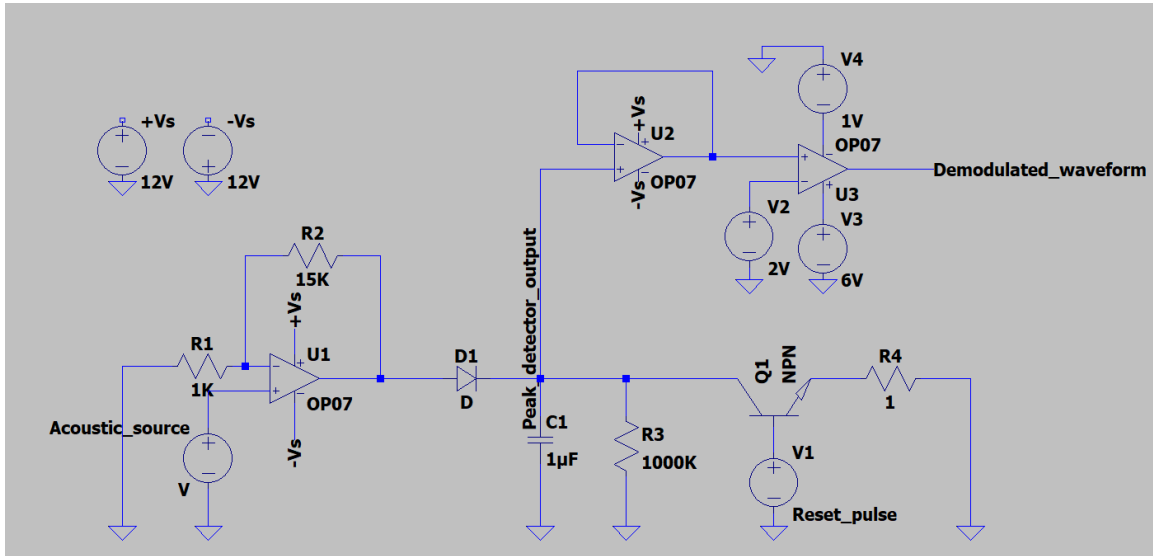


Figure 51: Schematic diagram of the acoustic receiver circuit

(set to 0 V) the peak value at the beginning of every time period T . This could be done by using a small rectangular reset pulse at the end of every time period, T . The pulse generator block in Figure 50 is responsible for doing so. Such pulse generation requires time synchronization between the sender and receiver. Therefore, PDOOK requires that the first transmitted bit to logic '1', which constitutes a necessary overhead. In our receiver design, the detection of the first acoustic signal peak triggers the generation of a reset pulse.

Shaping: From Figure 7 we can see the peak intensity of every acoustic signal is not the same. Hence, we need a decision circuit to make all the peaks in the same level. Usually, a comparator is used as a decision circuit. We need to keep in mind that this decision circuit might change the overall circuit gain. A voltage follower circuit is required to maintain the desired voltage and current level of the receiver circuit. Figure 49 shows what a demodulated PDOOK signal looks like. Figure 51 shows an example of a receiver circuit that has been used for our experiment. The amplifier, voltage follower and comparator (decision circuit) all have been designed using op-amps. The amplifier is a non-inverting type whose gain can be controlled by the $R1$ and $R2$ resistors. The peak detector is composed of a diode, capacitor and two resistors $R3$ and $R4$. The resistor $R3$ has very high value and $R4$ has very low value. A BJT switch has been used to switch between $R3$ and $R4$. This switch is controlled by a reset pulse, which we discussed earlier. When the value of that reset pulse is 0 V, the

peak detector is connected to the large resistor $R3$ so that the RC time constant of the peak detector becomes higher. The higher RC time constant helps the receiver retain the peak value for a long period of time. When we need to reset the peak value at the end of every time period, T , a small reset pulse in the BJT base connects the peak detector with the lower resistor $R4$, so that the capacitor of the peak detector can discharge quickly. Finally, a comparator circuit in conjunction with a voltage follower produces the two fixed voltage levels to successfully distinguish between logic '1' and '0'.

10.2 Validation Results

Both lab experiments and simulations have been conducted to validate our proposed PDOOK transmitter and receiver design. In this section, we will start discussing the lab experiments and then present simulation results which further capture the performance of PDOOK in a noisy environment.

10.2.1 Lab Experiments

Experiment Setup: In our experiments, the Geoscience Laser Altimeter System (GLAS) Q-switch Nd:Yag laser has been used as a light source [66]. The pulse duration of this laser source is 6 ns with energy of 1 ~ 50 mj per pulse. The diameter of the laser beam is 2 cm. It can produce a maximum of 40 Hz repetition rate. In order to control the laser driver and create control signals, a delay generator (DG535) has been used [67]. A Xilinx FPGA (Artix-7) has been used to generate random patterns of pulse periods and control the output of a delay generator [68]. Mirror and focusing lenses have been used to focus the laser light on the water and produce different laser irradiance in the water. In our experiments, we have used lenses of 20 cm and 7.5 cm focal lengths. We have used laser pulse energies ranging from 20 mj to 50 mj. For example, if we choose 20 mj laser pulse energy and 20 cm focusing lens, by using Eq. (10) we can produce $5.8 \times 10^{11} \text{ Wcm}^{-2}$ irradiance in the water which is above the breakdown threshold irradiance mentioned in chapter 3.

A 1.27m (L) x 0.6m (W) x 0.8m (H) water tank was used in the experiments. The tank is made of clear glass. Sound absorbing material is placed on the inner sides and bottom of the tank to mitigate reflection of acoustic signals. Given the constrained tank size, we placed our hydrophone at a maximum distance of 30 cm from the laser pulse focusing point. The hydrophone was placed at two different positions, namely, $\theta = 90^\circ$ and $\theta = 0^\circ$,

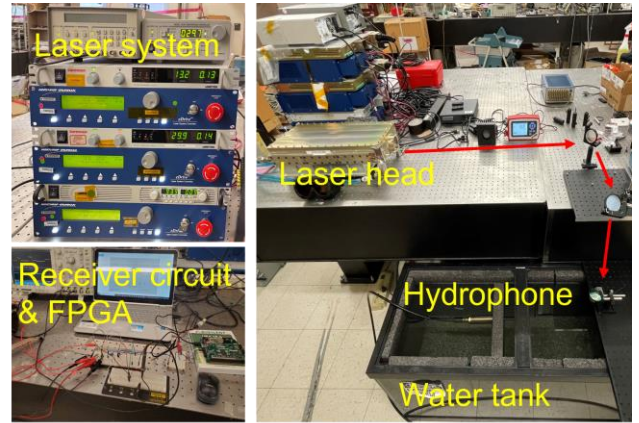


Figure 52: Depicting the experimental setup for air-to-underwater PA communication

from the vertical axis (norm on the water surface) of the laser light focusing point. Since the generated acoustic signal is very broadband, we have used the TC4014 hydrophone [69], which can detect acoustic signals up to 480 KHz. Such a hydrophone has a receiving sensitivity of $-186\text{dB} \pm 3\text{dB}$ re $1\text{V}/\mu\text{Pa}$. The hydrophone is connected with an active input module (EC6076) which provides power to the hydrophone [70]. Figure 52 shows our experimental setup.

Experimental Results: To validate our modulator/demodulator design, at first, we transmitted a random bit pattern ‘110110011’ at a repetition rate 10 Hz. Figure 53 shows the corresponding signals at the different stages of modulation/demodulation, as captured by a Tektronix DPO4054 digital oscilloscope. The topmost signal in the figure is the control

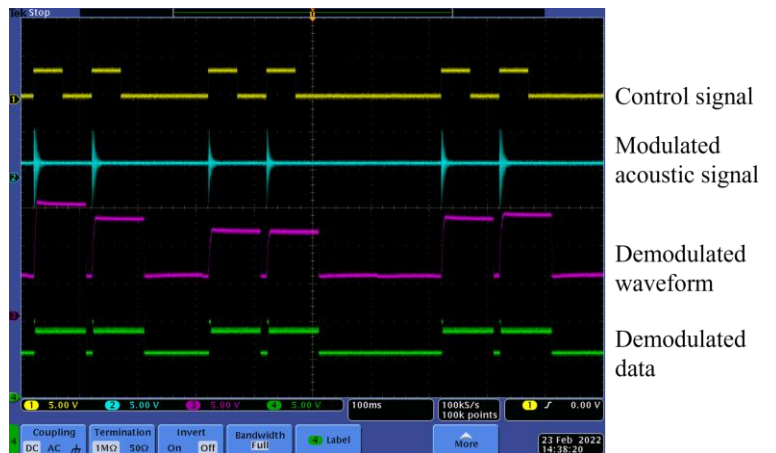
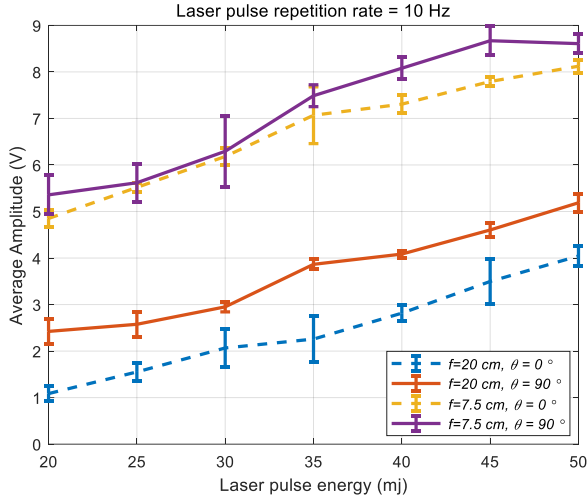
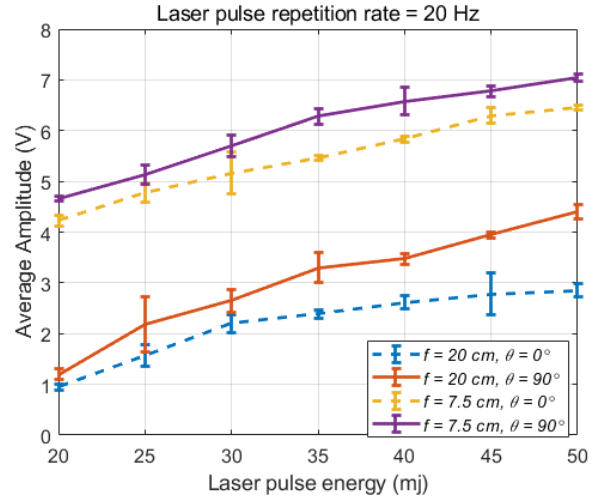


Figure 53: Tx and Rx data for laser pulse energy 30 *mj* and repetition rate 10 *Hz*

signal based on the above bit pattern which is used to generate a sequence of laser pulses. The next signal is



(a)



(b)

Figure 54: Effect of laser pulse energy on the received acoustic signal strength for laser repetition rate (a) 10 Hz and (b) 20 Hz

the modulated acoustic signal that reaches the receiver. Then, we show the PDOOK demodulated waveform before and after passing the decision circuit.

To further assess the design robustness, we have varied the laser pulse energy and observed the signal strength of the demodulated acoustic signal for various laser pulse repetition rates. The results are shown in Figure 54. We have used 20 cm and 7.5 cm lenses to focus the laser light inside the water. Figure 54a shows the signal strength for a laser repetition rate 10 Hz. As expected, the increase of laser pulse energy boosts the strength of the received acoustic signals. There are two additional important notes to make about the results. First, the 7.5 cm focusing lens yields a stronger signal than the 20 cm lens, which is attributed to the creation of more irradiance, as indicated by Eq. (10). Second, the received acoustic signal is directional, where a stronger signal is received when the hydrophone is placed at $\theta = 90^\circ$ than at $\theta = 0^\circ$. This observation is consistent with some experimental results found in the literature, e.g., in [46]. This kind of directivity depends on the generated plasma shape. Plasma could have different shapes, for example spherical or cylindrical. In our case the plasma is cylindrically shaped, and hence the signal strength is higher in one direction than the other.

The effect of focusing lenses is more significant than the hydrophone position. Figure 54b shows the results for a higher laser pulse repetition rate, specifically 20 Hz. The obtained results resemble those in Figure 54a, yet in all cases the received signal strength is a bit smaller than for a 10 Hz repetition rate. This is mainly because a higher repetition rate grows the probability of creating a vapor cloud which blocks subsequent pulses, as mentioned earlier in chapter 3 [56]. The effect of vapor cloud could be mitigated by using beam steering techniques. Employing a modulation technique which requires sending a smaller number of acoustic pulses could also reduce the effect of vapor cloud. In our future work, we will focus on how to diminish the impact of the vapor cloud on PA communication.

We further show the effect of laser pulse repetition rate on received signal strength in Figure 55. As expected, with the increase of laser repetition rate, the received signal becomes weaker. Figure 55a and 55b show the result for laser pulse energy of 20 mj and 50 mj, respectively. Again, the a 7.5 cm focusing lens creates stronger acoustic signals than the 20 cm counterpart. We also observe that positioning the hydrophone at $\theta = 90^\circ$ provides a better signal than $\theta = 0^\circ$. Moreover, the variation in acoustic signal strength becomes

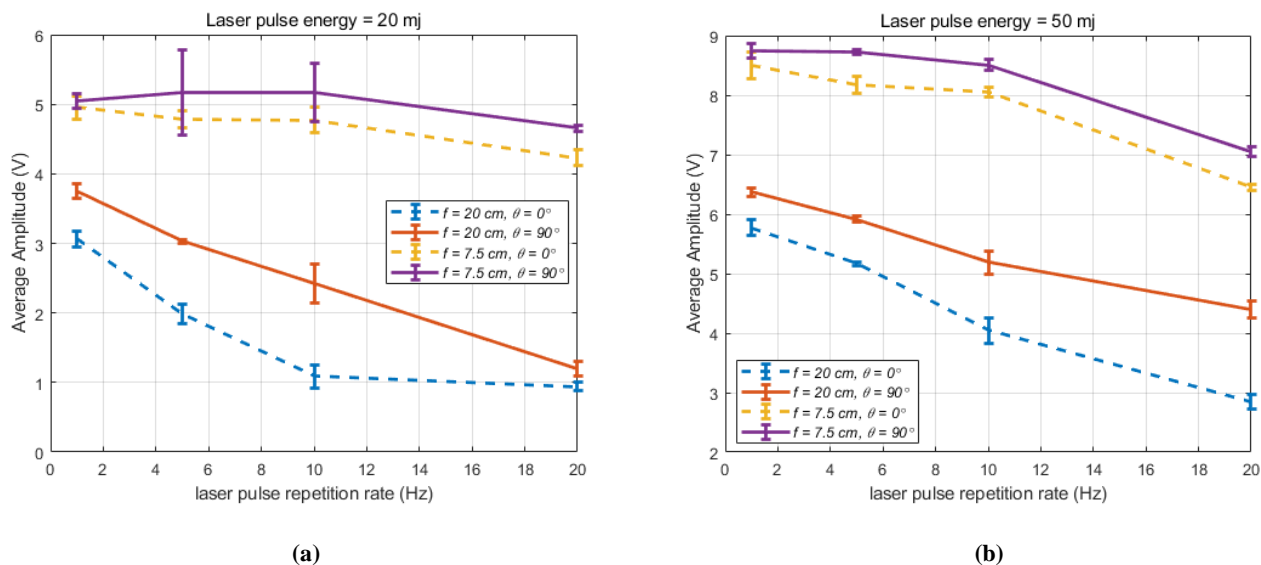


Figure 55: Effect of laser repetition rate on received acoustic signal strength for laser pulse energy (a) 20 mj and (b) 50 mj

smaller with the decrease of the laser repetition rate. This is mainly because the effect of vapor is more significant at high repetition rates.

10.2.2 Simulation Results

The aforementioned lab experiments have been conducted to show the performance of PDOOK at very short distance in a lab environment and in the presence of electrical noises only. Yet, in a real ocean environment, there could be other ambient noises that cannot be replicated in a lab prototype. Hence, we have pursued simulation to study the effect of ambient noises on the bit error rate (BER) and signal-to-noise ratio (SNR) performance of our proposed PDOOK modulation scheme.

BER calculation: At first, we injected random ambient noise and determined its effect on BER. We have assumed the ambient acoustic noise to be the additive white Gaussian noise (AWGN), and consequently calculated the error probability using the Q-function [71]. The Q-function of the noisy signal can be defined as follows:

$$Q\left(\frac{t-\mu}{\sigma}\right) = \frac{1}{\sqrt{2\pi\sigma^2}} \int_t^{\infty} \frac{e^{-(x-\mu)^2}}{2\sigma^2} dx \quad (86)$$

where, μ and σ^2 are the mean and the variance of the noise distribution, respectively. The above Q-function indicates the probability that a Gaussian random variable x will obtain a value larger than t . Our proposed modulation technique is OOK type modulation, which means it has two states: (i) logic '0' indicated by no (zero voltage) reception, and (ii) logic '1' implied by V_p voltage reception. Here, V_p is the voltage amplitude at a receiver which has been shown in Figure 54 and 55. For varying laser pulse energy and repetition rate, respectively. If the threshold voltage for distinguishing between these two stages is $\frac{V_p}{2}$, based on Eq. (86), the probability of erroneously detecting a logic stage can be defined as,

$$P(err) = BER = \frac{1}{\sqrt{2\pi\sigma^2}} \int_{\frac{V_p}{2}}^{\infty} \frac{e^{-(x)^2}}{2\sigma^2} dx \quad (87)$$

Here we assume the mean of the noise is 0. Now combining Eq. (86) and Eq. (87), we can conclude,

$$BER = Q\left(\frac{V_p}{2\sigma}\right) \quad (88)$$

Figure 56 shows the value of BER for different noise levels, σ and is plotted based on Eq. (86)-(88). The simulation is done using MATLAB and based on a laser repetition rate of 20 Hz. We can observe from the figure that with the increase of σ (the noise), the value of BER increases which is expected. The results have been shown for a receiver positioned at 0° and 90° , where the value of BER is higher for 0° position [72]. Intuitively,

when the received signal is stronger the value of BER is low; by considering Figure 54b and Figure 55 collectively give us an idea how much laser pulse energy is required in order to fulfill a certain BER requirement in a communication channel based on the noise level.

Similarly, Figure 57 shows the effect of the laser pulse repetition rate on the BER calculation for various noise levels. The simulation is performed for a fixed laser pulse energy of 50 mj. Here, we observe that with the increase of the laser pulse repetition rate, the BER grows which is also expected, because from Figure 55b we observe that with the increase of laser pulse repetition rate, the received signal strength diminishes. Figures 55b and 57 point out the value of maximum laser pulse

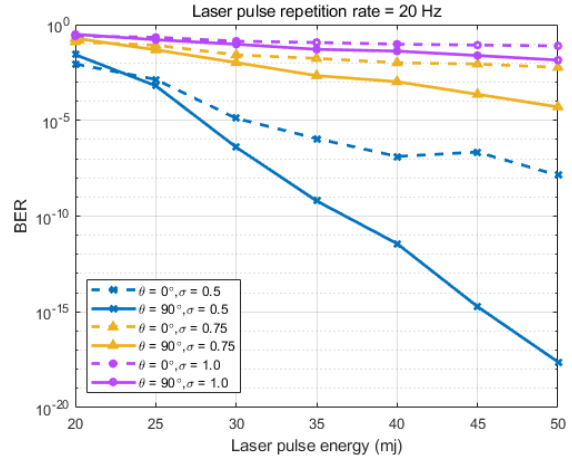


Figure 56: BER vs laser pulse energy for laser repetition rate 20 Hz for different noise levels

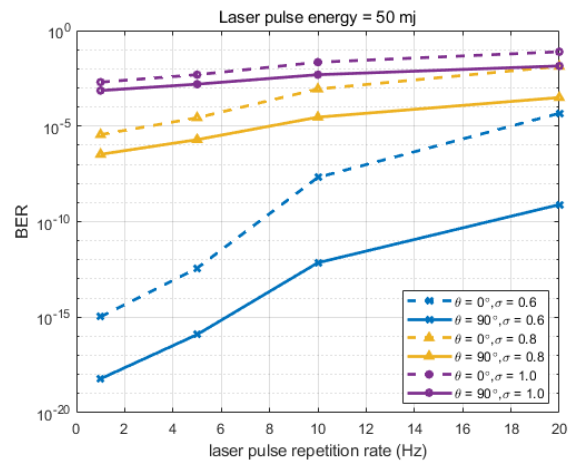


Figure 57: BER vs laser pulse repetition rate laser pulse energy for pulse energy 50 mj for different noise levels

repetition rate, i.e., what maximum bit rate is required for maintaining a certain *BER* value based on the noise level.

SNR calculation: Next, we determine the effect of noise on SNR for various underwater depths. In the lab experiments, we have measured Sound Pressure Level (SPL) at relatively close proximity from the generated plasma (acoustic source). In order to determine SPL at a further depth (longer distance), we need to factor the acoustic path loss model and ambient acoustic noise at that depth. Acoustic path loss (PL) can be estimated in dB as follows [73]:

$$PL(f) = k \cdot 10 \log D + D \cdot 10 \log a(f) \quad (89)$$

where, D is the underwater distance in km, k is the spreading factor, f is the acoustic source frequency in KHz, and a is the absorption coefficient. The spreading factor, k , determines the geometric shape of the acoustic propagation path; the value of k is 1.5 for so-called practical spreading [73]. The absorption coefficient, a , can be determined using Thorp's formula as follows [74]:

$$10 \log a(f) = 0.11 \frac{f^2}{1+f^2} + 44 \frac{f^2}{4100+f^2} + 2.75 \times 10^{-4} f^2 + 0.003 \quad (90)$$

The acoustic noise in an underwater environment has been modeled in [73], where turbulence, shipping, waves, and thermal noises are the main contributors. The power spectral density of these noise sources can be described by following empirical equations:

$$10 \log N_t(f) = 17 - 30 \log f \quad (91)$$

$$10 \log N_s(f) = 40 + 20(s - 0.5) + 26 \log f - 60 \log(f + 0.03) \quad (92)$$

$$10 \log N_w(f) = 50 + 7.5w^{\frac{1}{2}} + 20 \log f - 40 \log(f + 0.4) \quad (93)$$

$$10 \log N_{th}(f) = -15 + 20 \log f \quad (94)$$

Thus, the total noise $N(f)$ can be expressed as:

$$N(f) = N_t(f) + N_s(f) + N_w(f) + N_{th}(f) \quad (95)$$

In the above equations, s is the shipping activity factor whose value ranges from 0 to 1 and w is the wind speed in m/s. Using Eq. (89) - (95), we can calculate the SNR in dB as follows:

$$SNR = SPL - PL - N \tag{96}$$

All the parameters in Eq. (96) must be measured in dB.

Figure 58 shows the simulation results for SNR for various underwater depths. In this simulation, $w = 10$ m/s and $s = 1$. As expected, with the increase in the underwater depth, the SNR diminishes. The values of SNR have been shown for different settings of laser pulse energy at the transmitter side. With the increase of laser pulse energy, unsurprisingly the SNR also grows.

Figure 59 shows the effect of laser pulse repetition rate on SNR for various underwater depths. We can observe from the figure that the SNR becomes slightly smaller at higher laser repetition rates. This is mainly because at higher laser repetition rates, the acoustic signal is relatively weaker, as shown in Figure 55. Figure 58 and 59 point out the laser pulse energy and repetition rate required to obtain a certain amount of SNR for a known noisy channel.

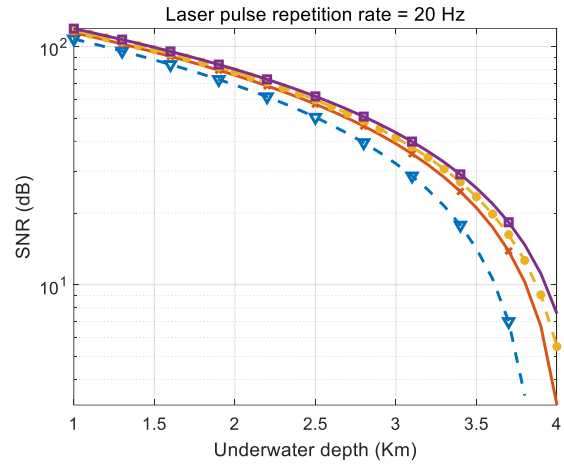


Figure 58: SNR vs underwater depth for different laser pulse energy

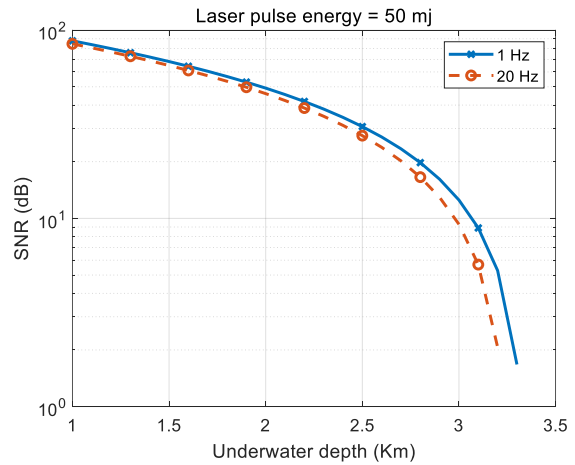


Figure 59: SNR vs underwater depth for different laser pulse repetition rate

Chapter 11: Conclusion and Future Work

11.1 *Conclusion*

This thesis has investigated the viability of establishing VLC links through the air-water interface in order to enable communication between an airborne base-station and underwater networks for short distance communication and photoacoustic energy conversion for long distance communication. For VLC, both the coverage area and light intensity have been studied under flat and wavy water surface conditions. We first have considered a single light source and then extended the analysis for multiple beamformed light sources. In clean and steady water, a single light source provides better intensity. In the case of turbid water and/or wavy surface, we promote beamforming of multiple light sources which boosts coverage while keeping enough intensity for VLC communication. Coverage is very important in the presence of water current because an underwater node can drift away.

Moreover, we studied the best modulation technique for VLC. We have presented a novel frame structure for DPPM modulation that enables dynamic adjustment of the symbol size to cope with varying channel conditions and transmission power constraints. The proposed frame provisions for specifying key DPPM attributes in order to inform the receiver about how to demodulate the transmitted signals. We have also developed an algorithm to dynamically change those DPPM attributes to optimize the bit rate and PER. Through simulation we have shown that our proposed Adaptive DPPM scheme with adjustable symbol length, provides better power and bandwidth efficiency than the DPPM with fixed symbol sizes. Our modulation scheme also provides better PER than traditional VLC modulation techniques such as OOK. We have also investigated how to improve the bandwidth efficiency for DPPM modulation schemes. Two novel frame structures, namely,

IDPPM and CDPPM, have been designed. IDPPM provides better results for relatively higher value of M , while CDPPM provides better results for lower value of M .

For long distance air-water communication, we promote photoacoustic energy transfer mechanism. First, we have studied the effect of the laser beam incident angle and observation angle on the spectral response of the generated acoustic signal using linear optoacoustic methods. The study has provided guidelines on optimum positioning of airborne and underwater nodes for which we can generate the best quality acoustic signals. The best quality implies an acoustic signal that has the highest spectral response at the lower frequency components. Low frequency acoustic signals are preferred since they can travel long distances in underwater medium. Through theoretical analysis and simulation, we have shown that if the sum of the refracted angle of the laser beam in the water medium and the observation angle of the underwater node from vertical axis is around 90° , we can create a relatively narrow-band signal with high signal strength. The results of our study are paramount for establishing robust communication links that leverage the optoacoustic effect and serve applications where deep underwater nodes need to be reached without employing gateway nodes on the water surface.

Furthermore, we have developed a novel peak detection based OOK (PDOOK) modulation scheme for photoacoustic communication. The thesis has presented the design of the PDOOK transmitter and receiver and provided details for the various modules. We have validated our design through extensive experiments using a lab-based prototype. Overall, the thesis provides analysis and protocols to establish downlink for communication across the air-water interface.

11.2 *Future Work*

The use of photoacoustic as a cross-medium communication is still in the early stage. There are many open research issues that need to be addressed. The biggest challenge will be how to improve the bit rate for this kind of photoacoustic communication. The achievable bit rate using photoacoustic is a couple of Hz to kHz range, which is very low for real-time audio and video communication. Moreover, focusing laser light inside

the water medium is difficult in practice. In lab setups, one can do so by using focusing lenses. However, such an approach is not practical in an open ocean environment. Auto-focusing laser light could be a viable option that is worth investigation.

Appendices

Appendix A: Calculation of water attenuation coefficient:

Using Beer's law, we can find the attenuation of optical signal at distance d as follows [59]:

$$I = I_0 \cdot e^{-k(\lambda)d} \quad (97)$$

Where $k(\lambda)$ is the attenuation coefficient (m^{-1}) of water, which is sum of absorption, $a(m^{-1})$ and scattering, $b(m^{-1})$ coefficient

$$k(\lambda) = a(\lambda) + b(\lambda) \quad (98)$$

The value of a and b depends on the biological factors of water and optical signal wavelength, λ . The absorption occurs mainly due to the pure water, chlorophyll-a, and humic and fulvic acids. The expression to get the value of a can be described as [60][61]:

$$a(\lambda) = a_w(\lambda) + a_f^0 C_f e^{-(k_f \lambda)} + a_h^0 C_h e^{-(k_h \lambda)} + a_c^0(\lambda) \left(\frac{C_c}{C_c^0} \right)^{0.602} \quad (99)$$

Where,

a_w = pure water absorption coefficient(m^{-1});

a_f^0 = specific absorption coefficient of fulvic acid;

a_h^0 = specific absorption coefficient of humic acid;

a_c^0 = specific absorption coefficient of chlorophyll in m^{-1} ;

C_f = concentration of fulvic acid in mg/m^3 ;

C_h = concentration of humic acid in mg/m^3 ;

C_c = concentration of chlorophyll-a in mg/m^3 ;

k_f = fulvic acid exponential coefficient, and

k_h = humic acid exponential coefficient.

The scattering is mainly caused by the water and particles, and can be express as [60][61]:

$$b(\lambda) = b_w(\lambda) + b_s^0(\lambda)C_s + b_l^0(\lambda)C_l \quad (100)$$

Where,

b_w = water scattering coefficient in m^{-1} ;

b_s^0 = scattering coefficient for small particulate matter in m^2/g ;

b_l^0 = scattering coefficient for large particulate matter in cm^2/g ;

C_s = concentration of small particles in g/m^3 , and

C_l = concentration of large particles in g/m^3 .

The scattering albedo is defined as the ratio of the amount of scattering to the overall attenuation, i.e., $w_0 = \frac{b}{k}$. Eq. (97) is valid when there is no contribution of the scattering light in the received light. However, in turbid water scattered light may reentered in the receiver field of view (FOV). In that case we need to rewrite Eq. (97) as follows [59]:

$$I = I_0 \cdot e^{-\gamma d} \quad (101)$$

Where $\gamma = a + (1 - n)b$ (102)

The scattering factor n ($0 \leq n \leq 1$) is used to recollect scattered light.

Appendix B: List of Acronyms:

Acronym	Description
VLC	Visual light communications
UWNs	Underwater Wireless Networks
PA	Photoacoustic
OOK	On-Off Keying
PPM	Pulse Position Modulation
DPPM	Differential Pulse Position Modulation
PER	Packet Error Rate
ADPPM	Adaptive Differential Pulse Position Modulation
FSK	Frequency-shift keying
PSK	Phase-shift keying
QAM	Quadrature amplitude modulation
PDOOK	Peak Detection based OOK
TARF	Translational Acoustic-RF communication
OPPM	Overlapping PPM
MPPM	Multiple PPM
DPIM	Pulse-interval modulation
DH-PIM α	Dual-header pulse-interval modulation
MFSK	Multi-frequency Shift Keying
KdV	Korteweg-de Vries equation
CDPPM	Complement DPPM
EDPPM	Enhanced DPPM
GLAS	Geoscience Laser Altimeter System
SPL	Sound Pressure Level

Chapter 12: References

- [1] D. Pompili and I. F. Akyildiz, "Overview of Networking Protocols for Underwater Wireless Communications," *IEEE Communications Magazine*, Vol. 47, No. 1, pp. 97 – 102, Feb. 2009.
- [2] M.V. Jamali, A. Chizari, and J. A. Salehi, "Performance Analysis of Multi-Hop Underwater Wireless Optical Communication Systems," *IEEE Photonics Technology Letters*, Vol. 29, pp. 462-465, Jan. 2017.
- [3] M. S. Islam, M. Younis and A. Ahmed, "Communication through Air Water Interface Using Multiple Light Sources," 2018 IEEE International Conference on Communications (ICC), Kansas City, MO, 2018, pp. 1-6.
- [4] M. S. Islam and M. F. Younis, "Analyzing Visible Light Communication Through Air–Water Interface," in *IEEE Access*, vol. 7, pp. 123830-123845, 2019.
- [5] J. Liu, B. Zheng, L. Zhao and Z. Gong, "A design of underwater wireless laser communication system based on PPM modulating method," in the *Proceedings of OCEANS 2015 - MTS/IEEE Washington*, Washington, DC, pp. 1-6, 2015.
- [6] S. Meihong, Y. Xinsheng and Z. Zhangguo, "The modified PPM modulation for underwater wireless optical communication," in the *Proceedings of the International Conference on Communication Software and Networks*, Macau, China, pp. 173-177, February 2009.
- [7] M. S. Islam and M. Younis, "An Adaptive DPPM for Efficient and Robust Visible Light Communication Across the Air-Water Interface," 2020 29th Wireless and Optical Communications Conference (WOCC), Newark, NJ, USA, 2020, pp. 1-6.
- [8] M. S. Islam and M. Younis, "A Novel Encoding Scheme for Improving the Bandwidth Efficiency of DPPM," to be published
- [9] A. G. Bell, "Upon the production of sound by radiant energy," *Philos. Mag. Ser. 5* 11, 510 (1881).
- [10] G. F. Edelmann, T. Akal, W. S. Hodgkiss, Seongil Kim, W. A. Kuperman and Hee Chun Song, "An initial demonstration of underwater acoustic communication using time reversal," in *IEEE Journal of Oceanic Engineering*, vol. 27, no. 3, pp. 602-609, July 2002.
- [11] S. Sendra, J. Lloret, J. M. Jimenez and L. Parra, "Underwater Acoustic Modems," in *IEEE Sensors Journal*, vol. 16, no. 11, pp. 4063-4071, June1, 2016.
- [12] X. Che, I. Wells, G. Dickers, P. Kear, and X. Gong, "Re-evaluation of RF electromagnetic communication in underwater sensor networks," *IEEE Communication Magazine*, Vol. 48, No. 12, pp. 143–151, Dec. 2010.
- [13] L. Liu, S. Zhou, and J.-H. Cui, "Prospects and problems of wireless communications for underwater sensor networks," *Wiley Wireless Comm. and Mobile Computing*, Vol. 8, No. 8, pp. 977–994, Oct. 2008.
- [14] I. F. Akyildiz, P. Wang, and Z. Sun, "Realizing underwater communication through magnetic induction," *IEEE Comm. Mag.*, Vol. 53, pp. 42-48, Nov. 2015.
- [15] M. C. Domingo, "Magnetic Induction for Underwater Wireless Communication Networks," *IEEE Transactions on Antennas and Propagation*, Vol. 60, pp. 2929 - 2939, June 2012.
- [16] J. W. Giles and I. N. Bankman, "Underwater optical communications systems. Part 2: basic design considerations," *Proc. of the IEEE Military Comm. Conf. (MILCOM 2005)*, Atlantic City, NJ., October 2005.
- [17] B. Cochenour, L. Mullen, A. Laux, and T. Curran, "Effects of multiple scattering on the implementation of an underwater wireless optical communications link," *Proc. of Oceans 2006*, Boston, MA, Sept. 2006.
- [18] N. Farr, A. Chave, L. Freitag, J. Preisig, S. White, D. Yoerger, and P. Titterton, "Optical modem technology for seafloor observatories," *Proc. of IEEE Oceans 2005*, pp. 928–934, Washington, DC, Dec. 2005.
- [19] T. Komine and M. Nakagawa, "Fundamental analysis for visible-light communication system using LED lights," in *IEEE Transactions on Consumer Electronics*, vol. 50, no. 1, pp. 100-107, Feb. 2004.
- [20] A. H. Azhar, T. Tran and D. O'Brien, "A Gigabit/s Indoor Wireless Transmission Using MIMO-OFDM Visible-Light Communications," in *IEEE Photonics Technology Letters*, vol. 25, no. 2, pp. 171-174, Jan.15, 2013.
- [21] F. Tonolini and F. Adib. "Networking across boundaries: enabling wireless communication through the water-air interface." *SIGCOMM* (2018).

- [22] X. Peng, W. Xu, X. Jin and J. Shang, "Adaptive filter design for suppressing the moving surface interferences in optic-acoustic remote sensing," Proc. of MTS/IEEE OCEANS 2013, San Diego, CA, 2013.
- [23] H. C. Dy and R. C. Gustilo, "Characterization of signal response for surface water movements in underwater optical wireless communications," TENCON 2012 IEEE Region 10 Conference, Cebu, 2012, pp. 1-6.
- [24] M. V. Jamali, J. A. Salehi and F. Akhoundi, "Performance Studies of Underwater Wireless Optical Communication Systems with Spatial Diversity: MIMO Scheme," IEEE Transactions on Communications, Vol. 65, No. 3, pp. 1176-1192, March 2017.
- [25] J. Wang, C. Lu, S. Li, and Z. Xu, "100 m/500 Mbps underwater optical wireless communication using an NRZ-OOK modulated 520 nm laser diode," Optics Express, Vol. 27, pp. 12171-12181, 2019.
- [26] X. Liu, S. Yi, R. Liu, L. Zheng and P. Tian, "34.5 m underwater optical wireless communication with 2.70 Gbps data rate based on a green laser with NRZ-OOK modulation," Proc. of the 14th China Int'l Forum on Solid State Lighting, China, Beijing, pp. 60-61, 2017.
- [27] D. Zhang, Y. Zhu, and Y. Zhang, "Multi-LED phase- shifted OOK modulation based visible light communication systems," IEEE Photonics Technology Letters, Vol. 25, December 2013.
- [28] B. Bai, Z. Xu and Y. Fan, "Joint LED dimming and high capacity visible light communication by overlapping PPM," Proc. 19th Annual Wireless and Optical Comm. Conf. (WOCC 2010), Shanghai, China, May 2010.
- [29] J. E. Gancarz, H. Elgala, and T. D.C. Little, "Overlapping PPM for band-limited visible light communication and dimming," Journal of Solid State Lighting, vol. 2, no.1, May 2015.
- [30] E. Elsayed, B. Yousif and M. Alzalabani, "Performance enhancement of the power penalty in DWDM FSO communication using DPPM and OOK modulation," Optical and Quantum Electronics, vol. 50, June 2018.
- [31] D. Shiu and J. M. Kahn, "Differential pulse-position modulation for power-efficient optical communication," IEEE Transactions on Communications, vol. 47, no. 8, pp. 1201-1210, Aug. 1999.
- [32] G. A. Mahdiraji and E. Zahedi, "Comparison of selected digital modulation schemes (OOK, PPM and DPIM) for wireless optical communications," Proc. of 4th Student Conference on Research and Development, Selangor, Malaysia, pp. 5-10, June 2006.
- [33] J. Ma, Y. Jiang, S. Yu, L. Tan and W. Du, "Packet error rate analysis of OOK, DPIM and PPM modulation schemes for ground-to-satellite optical communications," Optics Comm., vol. 283, pp. 237-242, January 2010.
- [34] N. M. Aldibbiat, Z. Ghassemlooy and R. McLaughlin, "Dual header pulse interval modulation for dispersive indoor optical wireless communication systems," IEE Proceedings - Circuits, Devices and Systems, vol. 149, no. 3, pp. 187-192, June 2002.
- [35] M. Pulkkinen, T. Haapala, J. Salomaa and K. Halonen, "45.2% Energy efficiency improvement of UWB IR Tx by use of differential PPM in 180nm CMOS," 2016 IEEE International Symposium on Circuits and Systems (ISCAS), Montreal, QC, pp. 193-196, 2016.
- [36] J. Wang, Z. Xu, and W. Hu, "Improved DPPM modulation for optical wireless communications," Proc. SPIE 5281, Optical Transmission, Switching, and Subsystems, vol. 5281, May 2004.
- [37] H. Ai-ping, F. Yang-Yu, L. Yuan-Kui, J. Meng, B. Bo and T. Qing-Gui, "A differential pulse position width modulation for optical wireless communication," Proc. of the 4th IEEE Conference on Industrial Electronics and Applications, Xi'an, China, pp. 1773-1776, 2009.
- [38] A. Vogel, J. Noack, G. Hüttman, et al. Mechanisms of femtosecond laser nanosurgery of cells and tissues. Appl. Phys. B 81, 1015–1047, 2005.
- [39] A. Vogel, S. Busch, and U. Parlitz, "Shock wave emission and cavitation bubble generation by picosecond and nanosecond optical breakdown in water," J. Acoust. Soc. Am., 100, pp. 148-165, 1996.
- [40] A. De La Zerda et al., "Carbon Nanotubes as Photoacoustic Molecular Imaging Agents in Living Mice," Nature Nanotech., vol. 3, no. 9, pp. 557–62, 2008.
- [41] H. Chen, Y. Shi, and D. Xing, "Photoacoustic Thermorelaxation Microscopy for Thermal Diffusivity Measurement," Opt. Lett., vol. 44, no. 13, pp. 3366–69, 2019.
- [42] Z. Ji, Y. Fu, J. Li, Z. Zhao and W. Mai, "Photoacoustic Communication from the Air to Underwater Based on Low-Cost Passive Relays," IEEE Communications Magazine, vol. 59, no. 1, pp. 140-143, January 2021.
- [43] Fletcher Blackmon, Lee Estes, and Gilbert Fain, "Linear photoacoustic underwater communication," Appl. Opt. 44, 3833-3845 (2005).

- [44] F. Blackmon, L. Antonelli, "Remote, aerial, opto-acoustic communications and sonar," Proc. SPIE 5778, Sensors, and Command, Control, Communications, and Intelligence (C3I) Technologies for Homeland Security and Homeland Defense IV, (20 May 2005).
- [45] Y. H. Berthelot, "Thermoacoustic generation of narrow-band signals with high repetition rate pulsed lasers," J. Acoust. Soc. Am. 85, 1173–1181 (1989).
- [46] T.G. Jones, M. Helle, A. Ting, and M. Nicholas, "Tailoring Underwater Laser Acoustic Pulses" (2012).
- [47] T. Sawa, N. Nishimura and S. Ito, "Wireless optical ethernet modem for underwater vehicles," *Proc. of the 15th IEEE Annual Consumer Communications & Networking Conf. (CCNC 2018)*, Las Vegas, NV, 2018.
- [48] H. M. Oubei et al, "2.3 Gbit/s underwater wireless optical communications using directly modulated 520 nm laser diode," *Opt. Express* Vol. 23, No.16, pp. 20743-20748, 2015.
- [49] <https://www.amazon.com/WAYLLSHINE-Zoomable-Scalable-Flashlight-Tactical/dp/B00W5PCTPW>
- [50] J. Sticklus, P. A. Hoehner and R. Röttgers, "Optical Underwater Communication: The Potential of Using Converted Green LEDs in Coastal Waters," *IEEE Journal of Oceanic Engineering*, (to appear).
- [51] H. Brundage. (2010, May 5). "Designing a Wireless Underwater Optical Communication System," M.S. thesis, Dept. of Mechanical Engineering, Massachusetts Institute of Technology, Cambridge, MA, 2010.
- [52] E. Infeld, A. Karczewska, P. Rozmej, "Solutions to the extended KdV equation for water surface waves," *Nonlinear Dynamics*, Vol. 91, No 2, pp 1085–1093, January 2018.
- [53] M. W. Dingemans, *Water Wave Propagation Over Uneven Bottoms*. Singapore: World Scientific, Jan. 1997, pp. 708-715.
- [54] R. Wiegel, "A presentation of cnoidal wave theory for practical application," *Journal of Fluid Mechanics*, Vol. 7, No. 2, 273-286, 1960.
- [55] Davies, Megan & Chattopadhyay, Amit. (2016). Stokes Waves Revisited: Exact Solutions in the Asymptotic Limit. *The European Physical Journal Plus*. 131. 10.1140/epjp/i2016-16069-7.
- [56] F. Blackmon and L. Antonelli, "Experimental demonstration of multiple pulse nonlinear optoacoustic signal generation and control," *Appl. Opt.* 44, 103-112, 2005.
- [57] M. Mahmud, M. S. Islam, M. Younis and G. Carter, "Optical Focusing-based Adaptive Modulation for Optoacoustic Communication," *Proc. 30th Wireless and Optical Comm. Conf. (WOCC)*, 2021, pp. 272-276.
- [58] M. V. Jamali, J. A. Salehi and F. Akhoundi, "Performance Studies of Underwater Wireless Optical Communication Systems with Spatial Diversity: MIMO Scheme," *IEEE Transactions on Communications*, Vol. 65, No. 3, pp. 1176-1192, March 2017.
- [59] B. Cochenour, L. Mullen, and J. Muth, "Effect of scattering albedo on attenuation and polarization of light underwater," *Opt. Lett.* 35, 2088-2090 (2010).
- [60] L. Johnson, R. Green, and M. Leeson, "Underwater optical wireless communications: depth dependent variations in attenuation," *Appl. Opt.* 52, 7867-7873 (2013).
- [61] V. Haltrin, "Chlorophyll-based model of seawater optical properties," *Appl. Opt.* 38, 6826-6832 (1999).
- [62] A. Mostafa, L. Lampe, "Optimal and Robust Beamforming for Secure Transmission in MISO Visible-Light Communication Links," *IEEE Trans. on Signal Processing*, Vol. 64, No. 24, pp. 6501 – 6516, Dec. 2016.
- [63] Y. S. Eroglu, et al., "Multi-Element Transmitter Design and Performance Evaluation for Visible Light Communication," *Proc. of IEEE Globecom Workshops*, San Diego, CA, Dec. 2015.
- [64] B. Wang. "Coverage problems in sensor networks: A survey," *ACM Computing Surveys*, Vol. 43, No. 4, Article 32,53 pages, Oct. 2011.
- [65] www.quantel-laser.com/en/products/item/ultra-50-100-mj--134.html
- [66] <https://ntrs.nasa.gov/api/citations/20070017920/downloads/20070017920.pdf>
- [67] https://www.valuetronics.com/product/dg535-stanford-research-pulse-generatorused?gclid=Cj0KCQiA2sqOBhCGARIsAPuPK0gOII_yWR8d5_0Ws3_iLy02vjT0xvEwisbktV11b0Rh9c3qosQG50aAgsVEALw_wcB
- [68] <https://digilent.com/reference/programmable-logic/nexys-4-ddr/start>
- [69] <http://www.teledynmarine.com/reson-tc-4014>
- [70] <http://www.teledynmarine.com/RESON-EC6076>
- [71] http://web.mit.edu/6.02/www/currentsemester/handouts/L08_slides.pdf

- [72] Y. Tagawa, S. Yamamoto, K. Hayasaka, & M. Kameda, "On pressure impulse of a laser-induced underwater shock wave," *Journal of Fluid Mechanics*, vol. 808, pp. 5-18, 2016.
- [73] M. Stojanovic, "On the relationship between capacity and distance in an underwater acoustic communication channel," *SIGMOBILE Mob. Comput. Commun. Rev.*, vol.11, issue 4, pp.34-43, October 2007.
- [74] L. Berkhovskikh, and Y. Lysanov, "Fundamentals of Ocean Acoustics," New York: Springer, 1982.

